NASA/TM–2019-220410/Volume I
NESC-RP-15-01037

Application of System Identification to Parachute Modeling

Daniel G. Murri/NESC, Eugene A. Morelli, Jing Pei, and Carlos M. Roithmayr
Langley Research Center, Hampton, Virginia

Daniel A. Matz
Johnson Space Center, Houston, Texas

Richard L. Barton, and Michael R. Mendenhall
Analytical Mechanics Associates, Hampton, Virginia

October 2019

NASA STI Program . . . in Profile

Since its founding, NASA has been dedicated to the advancement of aeronautics and space science. The NASA scientific and technical information (STI) program plays a key part in helping NASA maintain this important role.

The NASA STI program operates under the auspices of the Agency Chief Information Officer. It collects, organizes, provides for archiving, and disseminates NASA's STI. The NASA STI program provides access to the NTRS Registered and its public interface, the NASA Technical Reports Server, thus providing one of the largest collections of aeronautical and space science STI in the world. Results are published in both non-NASA channels and by NASA in the NASA STI Report Series, which includes the following report types:

- TECHNICAL PUBLICATION. Reports of completed research or a major significant phase of research that present the results of NASA Programs and include extensive data or theoretical analysis. Includes compilations of significant scientific and technical data and information deemed to be of continuing reference value. NASA counter-part of peer-reviewed formal professional papers but has less stringent limitations on manuscript length and extent of graphic presentations.

- TECHNICAL MEMORANDUM. Scientific and technical findings that are preliminary or of specialized interest, e.g., quick release reports, working papers, and bibliographies that contain minimal annotation. Does not contain extensive analysis.

- CONTRACTOR REPORT. Scientific and technical findings by NASA-sponsored contractors and grantees.

- CONFERENCE PUBLICATION. Collected papers from scientific and technical conferences, symposia, seminars, or other meetings sponsored or co-sponsored by NASA.

- SPECIAL PUBLICATION. Scientific, technical, or historical information from NASA programs, projects, and missions, often concerned with subjects having substantial public interest.

- TECHNICAL TRANSLATION. English-language translations of foreign scientific and technical material pertinent to NASA's mission.

Specialized services also include organizing and publishing research results, distributing specialized research announcements and feeds, providing information desk and personal search support, and enabling data exchange services.

For more information about the NASA STI program, see the following:

- Access the NASA STI program home page at *http://www.sti.nasa.gov*

- E-mail your question to help@sti.nasa.gov

- Phone the NASA STI Information Desk at 757-864-9658

- Write to:
  NASA STI Information Desk
  Mail Stop 148
  NASA Langley Research Center
  Hampton, VA 23681-2199

NASA/TM–2019-220410/Volume I
NESC-RP-15-01037

Application of System Identification to Parachute Modeling

Daniel G. Murri/NESC, Eugene A. Morelli, Jing Pei, and Carlos M. Roithmayr
Langley Research Center, Hampton, Virginia

Daniel A. Matz
Johnson Space Center, Houston, Texas

Richard L. Barton, and Michael R. Mendenhall
Analytical Mechanics Associates, Hampton, Virginia

National Aeronautics and
Space Administration

Langley Research Center
Hampton, Virginia 23681-2199

October 2019

Acknowledgments

The authors gratefully acknowledge the contributions of Dr. Jim Beaty, who retired from NASA and was the original developer of the Capsule Dynamics (CAPDYN) simulation tool used in this assessment.

Available from:

NASA STI Program / Mail Stop 148
NASA Langley Research Center
Hampton, VA 23681-2199
Fax: 757-864-6500

NASA Engineering and Safety Center
Technical Assessment Report

Volume I

Application of System Identification to Parachute Modeling

August 29, 2019

Report Approval and Revision History

NOTE: This document was approved at the August 29, 2019, NRB. This document was submitted to the NESC Director on September 20, 2019, for configuration control.

Approved:	*Original Signature on File*	9/23/19
	NESC Director	Date

Version	Description of Revision	Office of Primary Responsibility	Effective Date
1.0	Initial Release	Daniel G. Murri, NASA Technical Fellow for Flight Mechanics, LaRC	8/29/19

Table of Contents

Technical Assessment Report

List of Figures

List of Tables

Technical Assessment Report

1.0 Notification and Authorization

The NASA Engineering and Safety Center (NESC) was requested to determine the feasibility of using modern system identification techniques for developing high-fidelity parachute models from parachute drop-test flight data, using full-scale Orion Capsule Parachute Assembly System (CPAS) drop-test pendulum-mode flight data as a test case.

Mr. Daniel G. Murri, NASA Technical Fellow for Flight Mechanics, was selected to lead the assessment team. The primary stakeholders for this assessment were the analysts, chief engineers, and project managers of current and future vehicles that use parachutes.

2.0 Signature Page

Submitted by:

Team Signature Page on File – 10/2/19

Mr. Daniel G. Murri	Date

Significant Contributors:

Dr. Eugene A. Morelli	Date	Mr. Jing Pei	Date
Dr. Carlos M. Roithmayr	Date	Mr. Daniel A. Matz	Date
Mr. Richard L. Barton	Date	Mr. Michael R. Mendenhall	Date

Signatories declare the findings, observations, and NESC recommendations compiled in the report are factually based from data extracted from program/project documents, contractor reports, and open literature, and/or generated from independently conducted tests, analyses, and inspections.

3.0 Team List

Name	Discipline	Organization
Core Team		
Dan Murri	NESC Lead	LaRC
Rick Barton	Equations of Motion, Simulation Validation	AMA
Daniel Matz	Simulation Modeling	JSC
Mike Mendenhall	Equations of Motion, Simulation Validation	AMA
Gene Morelli	System Identification	LaRC
Jing Pei	Equations of Motion, Simulation Validation	LaRC
Jessica Powell	Simulation Modeling	JSC
Phil Robinson	Flight Data Analysis	JSC
Carlos Roithmayr	Equations of Motion	LaRC
Jim Beaty	CAPDYN Simulation	LaRC, retired
Consultants		
David Schuster	NASA Technical Fellow for Aerosciences	LaRC
Business Management		
John LaNeave	Program Analyst	LaRC/MTSO
Assessment Support		
Linda Burgess	Scheduler	LaRC/AMA
Jonay Campbell	Technical Writer	LaRC/SGT
Missy Strickland	Project Coordinator	LaRC/AMA

3.1 Acknowledgments

The authors gratefully acknowledge the contributions of Dr. Jim Beaty, who retired from NASA and was the original developer of the Capsule Dynamics (CAPDYN) simulation tool used in this assessment.

4.0 Executive Summary

Parachute models are used in numerous flight simulation tools to predict a wide range of parachute flight performance characteristics (e.g., parachute inflation loads, parachute stability and dynamics, vehicle touchdown conditions, and, ultimately, the safety and survivability of the system using the parachute). The current state of the art in developing parachute models is to initially estimate the parachute characteristics based on the parachute geometry and historical data and then add increased model fidelity based on data from wind tunnel and/or flight tests. This approach, however, can be deficient in identifying which parachute states (e.g., angle of attack, sideslip, angular rates, flyout angles, descent rate, dynamic pressure, proximity to other parachutes) are responsible for the parachute motion, and the relationship between those states and the forces on the parachute.

In aircraft flight testing, system identification techniques have been used for many years to extract highly accurate flight simulation models from flight data. These methods use statistical metrics and optimization to identify the states and controls responsible for aircraft behavior and to characterize the relationship of the forces and moments to those states and controls. The application of these techniques relies on having accurate flight-test instrumentation to measure aircraft states, control deflections, and aircraft response during dynamic maneuvers.

Some parachute development programs are now obtaining more comprehensive high-quality data during wind tunnel and flight testing. These data provide the potential to extract highly accurate models using system identification techniques. The goal of this assessment was to evaluate the feasibility of using system identification techniques to develop high-fidelity parachute models from parachute drop-test flight data. If successful, the application of system identification could reduce the time and cost in developing parachute models, increase fidelity and accuracy of parachute simulations, provide better understanding of parachute aerodynamics and vehicle touchdown conditions, and reduce risk or improve understanding of the risk to vehicles and systems using the parachutes.

This assessment used full-scale Orion Capsule Parachute Assembly System (CPAS) drop-test flight data as a test case. The CPAS flight tests employed high-fidelity photogrammetry techniques and an inertial measurement unit (IMU) on the payload to measure the parachute states, which allowed the application of system identification techniques. Furthermore, the CPAS flight tests studied were conducted with one main parachute missing (i.e., two of the three parachutes remaining), where an undesirable dynamic pendulum motion was observed. This pendulum motion has proven difficult to model accurately in simulations. For example, the Multi-Purpose Crew Vehicle (MPCV) Program developed a CPAS pendulum-mode aerodynamic model by starting with historical data and then refining the model using a manual process of iteratively running the flight simulation and manually changing model parameters based on engineering judgment and comparison of the simulation results with flight data. The resulting model predicts parts of the flight time histories fairly well (e.g., the limit cycle amplitude, frequency, and descent rate of the pendulum mode) but misses some of the coupled motions and other details of the flight behavior. Ideally, a model developed using system identification techniques would remove much of the time-consuming manual tuning and provide a numerically optimized model that accurately predicts more flight behavior and coupling.

As part of this assessment, three-body (i.e., two parachutes and one capsule) nonlinear equations of motion were independently developed and implemented in a flight simulation written in MATLAB. In addition, analytical check cases for parachute modes of motion were developed and used to validate independent simulation and the Flight Analysis and Simulation Tool (FAST) used for the CPAS simulation at Johnson Space Center (JSC).

Motions of a dynamic system made up of two parachutes and a capsule connected by elastic lines can be extremely complicated and can include not only the pendulum mode but also other modes of motion (e.g., flyout, maypole, and breathing modes). Some of these modes can occur at the same time, which complicates the analysis. For example, changes to parachute inflated shapes (including the breathing mode) can occur simultaneously with other modes and affect parachute motion and aerodynamic characteristics. Because of these complicated mode combinations, two approaches were used to model and understand the behavior of the two-parachute CPAS system.

The first approach was to analyze the dynamics of each individual mode observed during flight using first principles and linear modal analysis, making necessary simplifications along the way. This approach is analogous to the traditional modal analysis technique used to study airplane flight dynamics, in which the full nonlinear behavior of the airplane is decomposed into the phugoid and short period modes for the longitudinal dynamics, and into the spiral, roll-subsidence, and Dutch-roll modes for the lateral dynamics. The modal analysis technique in this assessment provided accurate modeling of individual modes and important insight into the geometric and aerodynamic factors affecting these modes. However, it is important to note that the modal analysis does not address the mechanisms that cause the system to enter a mode of motion or transition from one mode to another, nor does it describe motions where two or more modes occur simultaneously.

The second approach used in this assessment was to attempt to model the global nonlinear behavior of the two parachutes and the capsule system using system identification techniques that have been successfully applied to aircraft flight testing. As opposed to the linear modal analysis, it was hoped that a global model developed from system identification would be able to accurately characterize all parachute motions, including illuminating the mechanisms that cause the system to enter a specific mode or transition from one mode to another and predicting motions where two or more modes occur simultaneously.

After an extensive development process, the first step in global modeling using system identification was successfully applied to identify a high-fidelity model for the aerodynamic coefficients from the CPAS drop test flight data using equation-error techniques. This aerodynamic model provides important insight into the quantities affecting the modes of motion and determines which terms to include in the aerodynamic model.

The second step in the system identification process used the output-error technique in an attempt to numerically optimize the aerodynamic model to accurately predict the overall time history of the two parachutes and capsule using flight simulation, including the onset, characteristics, and coupling of the various modes of motion. Unfortunately, because of practical and computational difficulties, the output-error optimization did not converge to a parachute model that, when used in flight simulation, compared well with flight data. Findings and observations related to the factors that complicated the output-error analysis are provided in this report. The primary factors were the limited flight envelope of this passive system, which did not allow identification of the strong aerodynamic restoring force at high total angle of attack; the non-physical rapid changes in aerodynamic states near zero total angle of attack, related to how the parachute axes were defined; and the sometimes unstable behavior of the parachutes that resulted in poorly conditioned and brittle output-error optimization. Recommendations are provided for the future application of system identification to parachute modeling, including techniques that could overcome the limitations found in this assessment.

5.0 Assessment Plan

The planned products for this assessment included a simulation model of the two-parachute CPAS, including conditions where pendulum motion has been observed; comparisons of the predicted motions from simulation to the observed motions during the flight tests; and recommendations regarding the applicability of system identification to current and future parachute development programs and on the process for developing parachute models using system identification, if appropriate.

Technical activities for this assessment included:

1. Acquire CPAS flight test data and parachute geometry characteristics.
2. Develop independent three-body equations of motion and implement in a MATLAB simulation.
3. Develop analytical check cases and conduct analytical validation of the MATLAB simulation and FAST used for the CPAS simulation at JSC.
4. Conduct system identification equation-error analysis of flight data to identify key modeling parameters and develop simulation model structure.
5. Conduct system identification output-error analysis of flight data to develop system identification CPAS pendulum-mode simulation model.
6. Compare predicted motions from the system identification simulation model with observed motions from flight tests. Update the simulation model as needed.
7. Develop findings, observations, and NESC recommendations, and prepare an NESC final report.

6.0 Problem Description

Parachute models are used in numerous flight simulation tools to predict a wide range of parachute flight performance characteristics (e.g., parachute inflation loads, parachute stability and dynamics, vehicle touchdown conditions, and, ultimately, the safety and survivability of the system using the parachute). The current state of the art in developing parachute models is to initially estimate the parachute characteristics based on the parachute geometry and historical data and then add increased model fidelity based on data from wind tunnel and/or flight tests.

It is relatively straightforward to enter data from parachute static wind tunnel tests into a parachute simulation model to represent the static stability and lift and drag at static conditions. Sometimes, however, these data have unknown scaling effects and may not accurately represent the characteristics of the full-scale parachute system. In addition, the information required to model parachute dynamic stability characteristics must be developed from parachutes freely flying in wind tunnel or flight tests. Extracting dynamic stability data from wind tunnel or flight tests is more difficult and typically relies on expert judgment to identify the important model terms and manually tune associated model parameters in a flight simulation model, until the predicted motions match the flight behavior as closely as possible. This approach can be deficient in identifying the explanatory variables (e.g., total angle of attack, angular rates, flyout angles, descent rate, dynamic pressure, proximity to other parachutes), or combinations thereof, which are needed to predict the parachute motion and to quantitatively characterize the relationship between the explanatory variables and the aerodynamic forces acting on the parachute.

In aircraft flight testing, system identification techniques have been used for many years to extract highly accurate simulation models from flight data. These methods use statistical metrics and optimization to identify the states and controls that are responsible for aircraft behavior and characterize the relationship of the forces and moments to those states and controls. The application of these techniques relies on accurate flight-test instrumentation to measure the aircraft states, control deflections, and aircraft response during dynamic maneuvers.

Some parachute development programs are now obtaining more comprehensive high-quality data during wind tunnel and flight testing. These data provide the potential to extract highly accurate models using system identification techniques. The goal of this assessment was to evaluate the feasibility of using system identification techniques to develop high-fidelity parachute models from parachute drop-test flight data, using full-scale CPAS drop-test pendulum-mode flight data as a test case. The CPAS flight tests employed high-fidelity photogrammetry techniques and an IMU on the payload to measure the parachute states, allowing the application of system identification techniques.

Successful application of system identification techniques for the development of high-fidelity parachute models could reduce time and cost in developing parachute models, increase fidelity and accuracy of parachute simulations, provide better understanding of parachute aerodynamics and vehicle touchdown conditions, and reduce risk or improve understanding of the risk to the vehicles and systems using the parachutes.

Note that the terms “capsule” and “payload” are used somewhat interchangeably throughout the report. The CPAS drop tests for this study utilized either a modified capsule Parachute Test Vehicle (PTV) or a dart-shaped Parachute Compartment Drop Test Vehicle (PCDTV) as a payload.

6.1 CPAS

A diagram of the CPAS flight test article is shown in Figure 6.1-1. The flight data analyzed for this assessment were drop tests with two parachutes fully inflated. The normal CPAS system uses three main parachutes. Figure 6.1-2 shows the Earth-axis and body-axis coordinate systems used for each parachute. Airflow angles used for the aerodynamic modeling are defined in Figure 6.1-3. Reference 1 describes the flight test article, instrumentation, and data reduction required to produce the test vehicle best estimated trajectory (BET), as well as the best estimated winds and atmosphere data used for the main parachute modeling and prediction testing. The main parachute BET is the best estimate of the parachute motion and was created from the CPAS test vehicle data and photogrammetry of the parachute positions relative to the test vehicle.

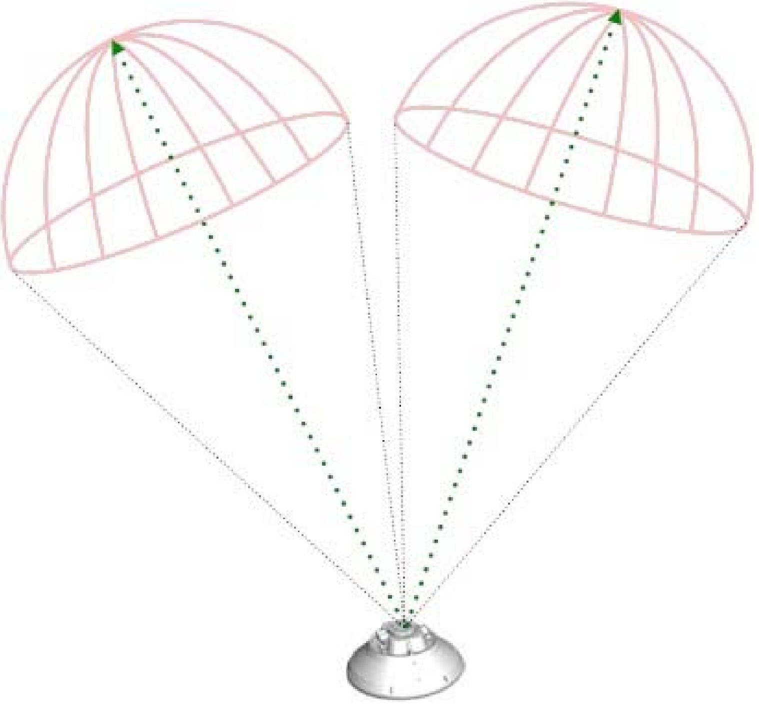

Figure 6.1-1. CPAS with Two of Three Main Parachutes Deployed

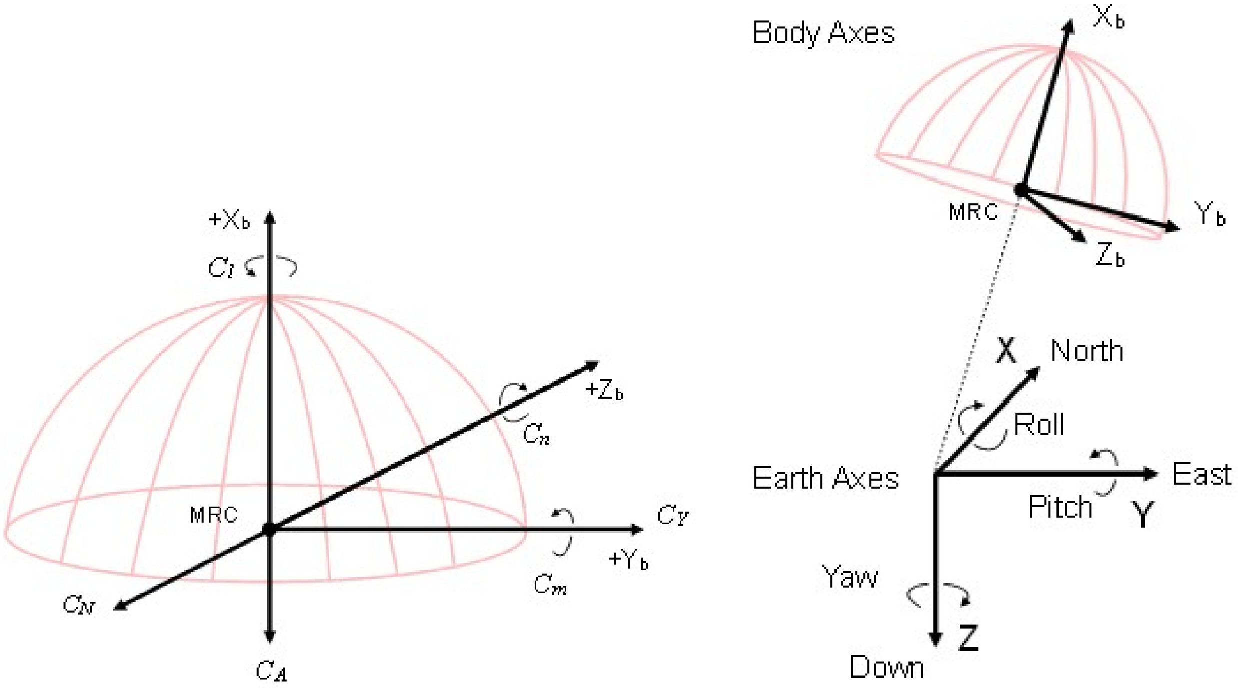

Figure 6.1-2. Reference Frames
(Credit: Phil Robinson, NASA JSC)

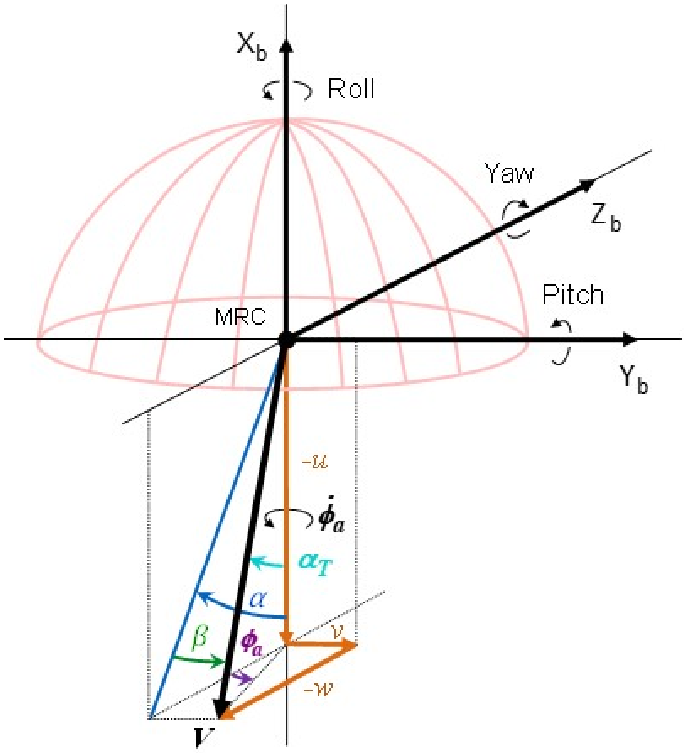

Figure 6.1-3. Flight Airflow Angle Definitions
(Credit: Phil Robinson, NASA JSC)

Airflow angles can be expressed in terms of body-axis air-relative velocity components as

$$\beta = \sin^{-1}(v/V) \tag{6.1-1}$$

$$\alpha = \tan^{-1}(-w/-u) \tag{6.1-2}$$

$$\alpha_T = \cos^{-1}(-u/V) \tag{6.1-3}$$

$$\phi_a = \tan^{-1}(v/-w) \tag{6.1-4}$$

$$V = \sqrt{u^2 + v^2 + w^2} \tag{6.1-5}$$

Time derivatives of the airflow angles can be expressed in terms of body-axis air-relative velocity components and their time derivatives as

$$\dot{\beta} = \frac{1}{\sqrt{V^2 - v^2}} \left[\dot{v} - v \frac{(u\dot{u} + v\dot{v} + w\dot{w})}{V^2} \right] \tag{6.1-6}$$

$$\dot{\alpha} = \frac{(u\dot{w} - w\dot{u})}{(u^2 + w^2)} \tag{6.1-7}$$

$$\dot{\alpha}_T = \frac{1}{\sqrt{V^2 - u^2}}\left[\dot{u} - \frac{u}{V^2}\left(u\dot{u} + v\dot{v} + w\dot{w}\right)\right] \tag{6.1-8}$$

$$\dot{\phi}_a = \frac{\left(v\dot{w} - w\dot{v}\right)}{\left(v^2 + w^2\right)} \tag{6.1-9}$$

Proximity of the parachutes was characterized as shown in Figure 6.1-4. Proximity effects on the parachute aerodynamics were assumed to depend on the normalized distance and speed along the line between the parachute centers:

$$\boldsymbol{D} = \begin{bmatrix} x_{E_{p1}} & y_{E_{p1}} & z_{E_{p1}} \end{bmatrix}^T - \begin{bmatrix} x_{E_{p2}} & y_{E_{p2}} & z_{E_{p2}} \end{bmatrix}^T \tag{6.1-10}$$

$$D_{prox} = \|\boldsymbol{D}\| / D_o \tag{6.1-11}$$

$$V_{prox} = \frac{d}{dt}\left(D_{prox}\right) \tag{6.1-12}$$

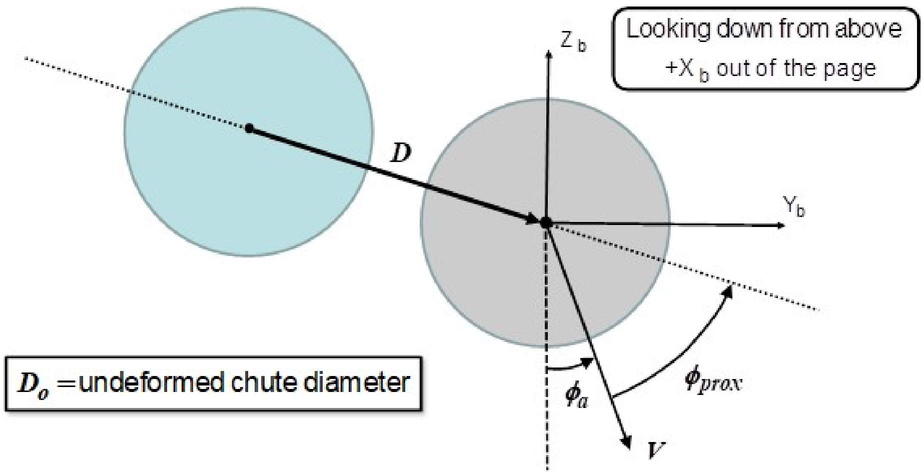

Figure 6.1-4. Parachute Proximity Quantities

The proximity angle ϕ_{prox} is defined as the angle between the air-relative velocity vector and the line connecting the parachute centers in the *y-z* plane in parachute body axes, which can be computed as

$$\phi_{prox} = \tan^{-1}\left(D_{w_y} / -D_{w_z}\right) \tag{6.1-13}$$

where $\boldsymbol{D}_w = \begin{bmatrix} D_{w_x} & D_{w_y} & D_{w_z} \end{bmatrix}^T$ is the $\boldsymbol{D}$ vector expressed in parachute wind axes, which are parachute body axes rotated through the aerodynamic azimuth angle ϕ_a, so that the air-relative velocity vector is directed along the negative *z* parachute wind axis.

Parachute cluster angles, called swing angle θ_s and flyout angle θ_f are shown in Figure 6.1-5.

Figure 6.1-5. Parachute Cluster Angles
(Credit: Tuan Truong, NASA JSC)

These angles can be computed from the parachute positions in Earth axes as

$$\boldsymbol{r}_{p1/a} = \begin{bmatrix} x_{E_{p1}} & y_{E_{p1}} & z_{E_{p1}} \end{bmatrix}^T - \begin{bmatrix} x_{E_a} & y_{E_a} & z_{E_a} \end{bmatrix}^T \tag{6.1-14}$$

$$\boldsymbol{r}_{p2/a} = \begin{bmatrix} x_{E_{p2}} & y_{E_{p2}} & z_{E_{p2}} \end{bmatrix}^T - \begin{bmatrix} x_{E_a} & y_{E_a} & z_{E_a} \end{bmatrix}^T \tag{6.1-15}$$

$$\bar{\boldsymbol{r}} = \left(\boldsymbol{r}_{p1/a} + \boldsymbol{r}_{p2/a}\right) / 2 \tag{6.1-16}$$

$$\bar{\boldsymbol{n}} = \bar{\boldsymbol{r}} \,/\, \left\| \bar{\boldsymbol{r}} \right\| = \begin{bmatrix} \bar{n}_x & \bar{n}_y & \bar{n}_z \end{bmatrix}^T \tag{6.1-17}$$

$$\theta_s = \tan^{-1}\left(\sqrt{\bar{n}_x^2 + \bar{n}_y^2} \,/\, \left| \bar{n}_z \right| \right) \tag{6.1-18}$$

$$\boldsymbol{n}_{p1/a} = \boldsymbol{r}_{p1/a} \,/\, \left\| \boldsymbol{r}_{p1/a} \right\| \qquad \boldsymbol{n}_{p2/a} = \boldsymbol{r}_{p2/a} \,/\, \left\| \boldsymbol{r}_{p2/a} \right\| \tag{6.1-19}$$

$$\theta_f = \frac{1}{2} \cos^{-1}\left(\boldsymbol{n}_{p1/a} \cdot \boldsymbol{n}_{p2/a} \right) \tag{6.1-20}$$

Table 6.1-1 contains the CPAS mass, geometry, and tension line properties.

Table 6.1.1. CPAS Properties used for System Identification

Quantity	Value	Units
l = reference length = nominal parachute canopy diameter	116	ft
S = parachute reference area = $\pi l^2/4$	10,568.3	ft^2
V_o = reference airspeed	32	ft/s
V_{ea} = parachute canopy enclosed air volume = $\pi(0.7l)^3/12$	140,164	ft^3
m_d, parachute dry mass	10.22	slug
g = gravitational acceleration	32.174	ft/s^2
L = nominal line length	234	ft
k = line spring constant	15,000	lbf/ft
ζ = line damping constant	10,000	lbf-s/ft
S_c = capsule reference area	213.8	ft^2
m_c, capsule mass	648.44	slug

Flight data came mainly from onboard instrumentation and videogrammetry. Airspeed, total angle of attack, aerodynamic azimuth angle, and dynamic pressure came from the BET data, which were based on flight instrumentation data and estimated atmospheric conditions and winds aloft at the time of the flight test. Velocities, accelerations, and related quantities for the parachutes were computed by smooth numerical differentiation of the position data obtained from an IMU on the payload, as well as videogrammetry. Flight data from onboard instrumentation were corrected for data dropouts and, in some cases, were interpolated to a uniform sampling rate. The sample rate for the flight data used in the analysis and modeling was 10 Hz, corresponding to a sampling interval of 0.10 s.

Enclosed mass within each parachute canopy was calculated using the volume of an undeformed hemisphere for each parachute canopy and the local air density from the BET data. As shown in Table 6.1.1, the nominal parachute canopy diameter was reduced using a factor of 0.7 in the calculation of parachute enclosed air volume to account for the shape of the parachute canopy in flight, compared with the measured 116-ft diameter circle formed by the canopy laid flat on the ground. The enclosed air volume was multiplied by air density at the current altitude, interpolated from BET data, to compute enclosed air mass. Dynamic air mass effects (e.g., spillage of the enclosed air mass around the canopy and apparent mass effects) were not modeled specifically but instead were subsumed into the identified aerodynamic model.

Tension forces in the lines connecting the payload to the parachutes were measured with load cells. However, the data exhibited non-physical variations because of practical problems with the measurements and was inconsistent across different parachutes and flights based on model prediction tests. Therefore, measured line tension forces were replaced with the mean values of estimated line tension forces computed by force balance using accelerometer data from the IMU on the payload, the mass of the payload, the estimated aerodynamic drag coefficient of the payload, airspeed, dynamic pressure, and the known position of the parachute canopies relative to the payload from videogrammetry. Figure 6.1-6 shows a free-body diagram illustrating the forces acting on the payload, which was used to estimate the line tension forces at each sample time. The line tension magnitudes at each sample time were determined by least squares because two line tension magnitudes were computed but all three components of the vectors in Earth axes were available. Note that the accelerometer measurements from the IMU on the payload quantify acceleration from applied forces and, therefore, exclude gravity.

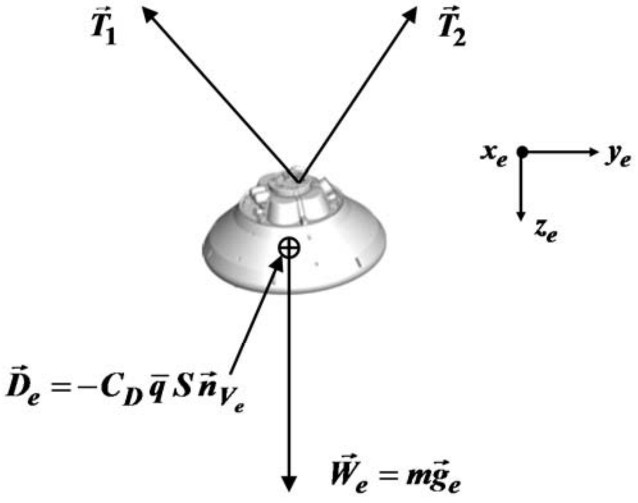

$$\vec{T}_1 + \vec{T}_2 = \left|\vec{T}_1\right| \vec{n}_{T_1} + \left|\vec{T}_2\right| \vec{n}_{T_2} = m\vec{a}_e - \vec{D}_e$$

All quantities except magnitudes $\left|\vec{T}_1\right|$ and $\left|\vec{T}_2\right|$ are known from measurements and capsule C_D

Figure 6.1-6. Capsule Free-body Diagram

6.2 Overview of CPAS Pendulum Mode and Other Benign Modes

Motions of a system made up of two parachutes and a capsule can be extremely complicated and can include not only the pendulum mode but also other modes of motion (e.g., flyout, maypole, and breathing modes). In addition, some of these modes can be coincident, and changes to the parachute's inflated shape (including the breathing mode) can occur during all of these modes and affect the parachute motion and aerodynamic characteristics.

As discussed in reference 2, it is apparent from flight tests that the system, made up of two main parachutes and a capsule, can undergo several distinct dynamical behaviors. The most significant and problematic of these is the pendulum mode, in which the system develops a pronounced swinging motion, which for CPAS exhibits an amplitude up to about 24 degrees. Large excursions away from vertical by the capsule could cause it to strike the ground at a large horizontal or vertical speed or at a dangerous incidence angle and jeopardize the safety of the astronauts during a crewed mission. In reference 2, Ali *et al.* summarized a series of efforts taken by the CPAS project to understand and mitigate the pendulum issue. The period of oscillation and the location of the system's pivot point are determined from post-flight analysis [ref. 3].

Other noticeable modes include: 1) the flyout (i.e., scissors) mode, in which the parachutes move back and forth symmetrically with respect to the vertical axis and come in contact with one another, similar to the motion of a pair of scissors; 2) the maypole mode, in which the two parachutes circle around the vertical axis at a nearly constant radius and period; and 3) the breathing mode, in which deformation of the non-rigid canopies affects the axial acceleration of the system in an oscillatory manner. These modes are considered more benign than the pendulum mode but are important to understand for evaluation and prediction of the overall parachute characteristics.

6.3 Approach and Description of Methods

Because of the complicated combinations of modes, two approaches were used to model and understand the behavior of the two-parachute CPAS system. The initial approach was to first analyze the dynamics of each individual mode observed during flight using first principles and modal analysis and make simplifications along the way. This approach is analogous to the traditional modal analysis technique used to study airplane flight dynamics [ref. 4], in which the full nonlinear behavior of the airframe is decomposed into the phugoid and short period modes for the longitudinal dynamics, and into the spiral, roll-subsidence, and Dutch-roll modes for the lateral dynamics. The modal analysis technique provided insight into the geometric and aerodynamic factors affecting these individual modes. However, it is important to note that the modal analysis does not address the mechanisms that cause the system to enter a mode of motion or transition from one mode to another, nor does it describe motions in which two or more modes occur simultaneously.

The other approach used in this assessment was to attempt to model the global nonlinear behavior of the two parachutes and capsule system using system identification techniques, which have been successfully applied to aircraft flight testing. This global system identification modeling technique used a two-step process: equation error modeling followed by output-error model optimization. As opposed to the modal analysis, it was hoped that a global model developed from system identification would be able to evaluate and model all the parachute motions, including the mechanisms that cause the system to enter a specific mode or transition from one mode to another, and describe motions in which two or more modes occur simultaneously.

As part of this assessment, an independent flight simulation was developed. Equations of motion were derived for a capsule connected to two parachutes. The capsule is modeled as a rigid body having 6 degrees of freedom (DOF), and each parachute is modeled as a particle having 3 DOF. This independent flight simulation was coupled with the system identification tools to allow the application of the equation-error and output-error methods. In addition, analytical check cases of parachute modes of motion were developed and used to validate the independent simulation and FAST, which was used for the CPAS simulation. The description of the equations of motion, the resulting flight simulation, and the analytical check cases are described in this section. Note that in Sections 6.3.1 and 6.3.2, which address system dynamics, the symbol ˆ is used to represent a unit vector; in Sections, 6.3.5 through 6.3.7, which address system identification, the symbol ˆ is used to represent a parameter estimate.

6.3.1 Pendulum Motion Modal Analysis

Key results from contemporary studies of the pendulum motion are provided here in brevity; details of the analyses are given in references 5 and 6.

6.3.1.1 Dynamics and Aerodynamics Model Structure

The planar dumbbell model used to study the underlying dynamics of the pendulum motion is illustrated in Figure 6.3.1-1. The capsule is modeled as a particle rather than an extended rigid body, and aerodynamic forces acting on the capsule are ignored [ref. 7]. The two parachutes are treated as a single particle. The rigid body B contains two particles. Particle P_C has a mass of m_C, the total mass of two parachutes, which includes dry mass as well as the mass of air trapped in each of the canopies. The mass of the entrapped air is calculated based on the method described in Section 6.1, assuming constant air density. Particle P_L has a mass of m_L and represents the capsule. Body B moves such that P_C and P_L remain at all times in a plane fixed in a Newtonian reference frame N. A right-handed set of mutually perpendicular unit vectors $\hat{\mathbf{n}}_1$, $\hat{\mathbf{n}}_2$, and $\hat{\mathbf{n}}_3$ is fixed in N. Unit vectors $\hat{\mathbf{n}}_1$ and $\hat{\mathbf{n}}_3$ lie in the plane in which motion takes place and are directed as shown in Figure 6.3.1-1; $\hat{\mathbf{n}}_1$ is horizontal, $\hat{\mathbf{n}}_2$ is directed into the page, and $\hat{\mathbf{n}}_3$ is vertical, directed downward. A right-handed set of mutually perpendicular unit vectors $\hat{\mathbf{b}}_1$, $\hat{\mathbf{b}}_2$, and $\hat{\mathbf{b}}_3$ is fixed in B. Unit vectors $\hat{\mathbf{b}}_1$ and $\hat{\mathbf{b}}_3$ are directed as shown in Figure 6.3.1-1; $\hat{\mathbf{b}}_1$ has the same direction as the position vector $\mathbf{r}^{P_C P_L}$ from P_C to P_L. Unit vector $\hat{\mathbf{b}}_2$ is directed into the page (note that it is fixed in N as well as in B).

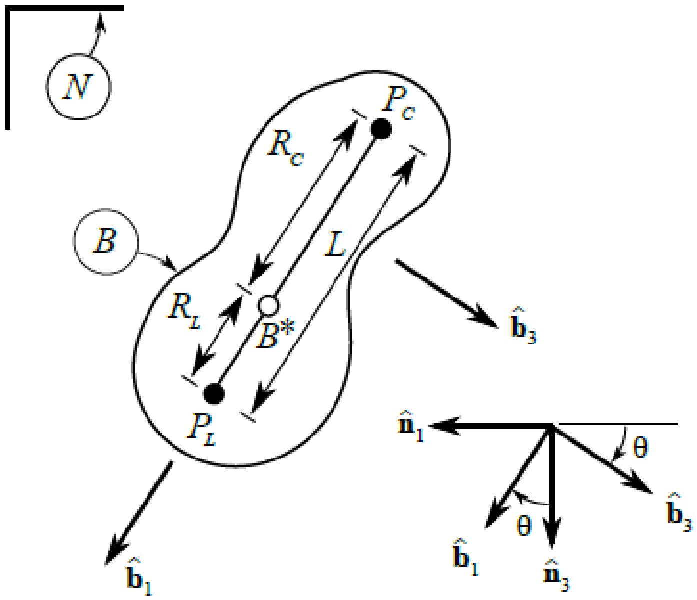

Figure 6.3.1-1. Dumbbell Model for Pendulum Motion

The mass center of B, B^*, is fixed in B between particles P_C and P_L. The distance R_L from B^* to P_L can be expressed in terms of the distance L between P_C and P_L:

$$R_L = \frac{m_C}{m_C + m_L} L \tag{6.3.1-1}$$

The distance R_C from B^* to P_C can be expressed similarly:

$$R_C = \frac{m_L}{m_C + m_L} L \tag{6.3.1-2}$$

The resultant of the forces acting on P_L is given by

$$\mathbf{F}_L = W_L\hat{\mathbf{n}}_3 - T\hat{\mathbf{b}}_1 \tag{6.3.1-3}$$

where $-T\hat{\mathbf{b}}_1$ represents the internal force applied to P_L to keep it fixed in rigid body B, $W_L = m_L g$, and g is the magnitude of the local gravitational force per unit mass. As mentioned earlier, aerodynamic force acting on the capsule is neglected. The resultant of the forces acting on P_C is given by

$$\mathbf{F}_C = W_C\hat{\mathbf{n}}_3 + (T - A_x)\hat{\mathbf{b}}_1 + A_z\hat{\mathbf{b}}_3 \tag{6.3.1-4}$$

where A_x and A_z characterize the resultant of the aerodynamic forces applied to the two parachutes represented by P_C. W_C is the sum of the dry weights of the two parachutes; the weight of the air trapped in their canopies is ignored because the gravitational force exerted on that air is assumed to be counteracted by buoyancy effects from the ambient atmosphere.

The following two relationships governing translation and rotation of the dumbbell are derived in reference 5:

$$\begin{aligned} {}^{N}\mathbf{a}^{B^*} = \frac{1}{m_C + m_L}\{&-[A_x \sin\,\theta + A_z \cos\,\theta]\hat{\mathbf{n}}_1 \\ &+ [W_C + W_L - A_x \cos\,\theta + A_z \sin\,\theta]\hat{\mathbf{n}}_3\} \end{aligned} \tag{6.3.1-5}$$

$$\left(m_C {R_C}^2 + m_L {R_L}^2\right)\ddot{\theta} = R_C(W_C \sin\theta + A_z) - R_L W_L \sin\theta \tag{6.3.1-6}$$

One can obtain Equation (6.3.1-6) by summing moments about the mass center, B^*, and writing Euler's equation of rotational motion for B; the coefficient multiplying $\ddot{\theta}$ is the central moment of inertia of B for a line parallel to $\hat{\mathbf{b}}_2$. In view of Equations (6.3.1-1) and (6.3.1-2) and the fact that $W_L = m_L g$, Equation (6.3.1-6) can be rewritten as

$$\ddot{\theta} + \frac{1}{m_C L}[(m_C\, g - W_C) \sin\,\theta - A_z] = 0 \tag{6.3.1-7}$$

A_x, the magnitude of the resultant of the aerodynamic axial forces applied to the two parachutes, can be expressed as

$$A_x = 2q_\infty S_{\text{ref}} C_A \tag{6.3.1-8}$$

where q_∞ is the dynamic pressure, S_{ref} is the reference area of a single parachute, and C_A is the drag coefficient for a single parachute. The absolute value of A_z is the magnitude of the resultant of the aerodynamic normal forces applied to the two parachutes; A_z can be expressed as

$$A_z = -2q_\infty S_{\text{ref}} C_N \tag{6.3.1-9}$$

where C_N is the aerodynamic normal force coefficient for a single parachute. As discussed in references 7 and 8, C_A and C_N are nonlinear functions of α, the instantaneous angle of attack of the parachute:

$$C_A(\alpha) = C_{A_o} + \frac{1}{2} C_{A_\alpha}\alpha_0\left(\frac{\alpha^2}{{\alpha_0}^2} - 1\right) \tag{6.3.1-10}$$

$$C_N(\alpha) = \frac{C_{N_\alpha}}{2\alpha_0^2}(\alpha^3 - {\alpha_0}^2\alpha) \tag{6.3.1-11}$$

Here, α_0 is the stable trim angle of attack, and C_{N_α} is the slope of the C_N curve at α_0.

In a steady-state flight condition, C_A and C_N are nonlinear functions of α, the instantaneous angle of attack of the parachute, as shown with the red curves in Figure 6.3.1-2 and discussed in reference 7. Equilibria exist at the three points where $C_N = 0$. The equilibrium point $\alpha = 0$ is unstable, and the two equilibrium points at $\alpha = \pm\alpha_0$ are stable. In this analysis, C_A is treated as a constant, and C_{N_α}, the slope of the curve for C_N, is taken to be constant in the neighborhood of an equilibrium point. C_N is expressed as

$$C_N = C_{N_\alpha}(\alpha - \alpha_0) + C_{N_{\dot\alpha}}\dot\alpha_Q = C_{N_\alpha}(\alpha - \alpha_0) + C_{N_{\dot\alpha}}\dot\theta \tag{6.3.1-12}$$

where α_0 is the trimmed angle of attack of the parachute and the term $C_{N_{\dot\alpha}}\dot\alpha_Q$ is added to account for unsteady flow when α is changing with time. In the literature (e.g., refs. 9 and 15), $C_{N_{\dot\alpha}}$ is multiplied by the time derivative of the angle of attack at the aircraft mass center, a point having steady-state velocity. Instead, we use the time derivative of angle of attack at a point *Q* because, as discussed here, the velocity of this point is nearly constant. $\alpha_Q = \theta - \gamma$; therefore, $\dot\alpha_Q = \dot\theta$ because γ is constant.

The location can be determined of a pivot point *Q* whose velocity ${}^N\mathbf{v}^Q$ in *N* is nearly constant. The magnitude of ${}^N\mathbf{v}^Q$ is denoted by V_∞ and regarded as constant. Hence, ${}^N\mathbf{v}^Q$ can be written as

$${}^N\mathbf{v}^Q = V_\infty\left(\cos\alpha_Q\,\hat{\mathbf{b}}_1 + \sin\alpha_Q\,\hat{\mathbf{b}}_3\right)$$

where α_Q is the angle of attack at *Q*. The velocity ${}^N\mathbf{v}^{P_C}$ of P_C in *N* then can be expressed as

$${}^N\mathbf{v}^{P_C} = {}^N\mathbf{v}^Q + L_C\dot\theta\hat{\mathbf{b}}_3 = V_\infty\cos\alpha_Q\,\hat{\mathbf{b}}_1 + \left(V_\infty\sin\alpha_Q + L_C\dot\theta\right)\hat{\mathbf{b}}_3 \tag{6.3.1-13}$$

where $\mathbf{r}^{QP_C} = -L_C\hat{\mathbf{b}}_1$ is the position vector from *Q* to P_C. The tangent of the angle of attack α at P_C is given by

$$\tan\alpha = \frac{{}^N\mathbf{v}^{P_C}\cdot\hat{\mathbf{b}}_3}{{}^N\mathbf{v}^{P_C}\cdot\hat{\mathbf{b}}_1} = \frac{V_\infty\sin\alpha_Q + L_C\dot\theta}{V_\infty\cos\alpha_Q} \tag{6.3.1-14}$$

When both angles of attack are small, the following approximation can be used:

$$\alpha \approx \alpha_Q + \frac{L_C\dot\theta}{V_\infty} \tag{6.3.1-15}$$

The second term on the right-hand side is referred to as angle of attack induced by $\dot\theta$; $\alpha_Q = \theta - \gamma = \theta + \alpha_0$, where $\alpha_0 = -\gamma$ is constant. Thus,

$$\alpha - \alpha_0 \approx \theta + \frac{L_C\dot\theta}{V_\infty} \tag{6.3.1-16}$$

Substitution from Equation (6.3.1-16) into Equation (6.3.1-12) yields

$$\begin{aligned} C_N &= C_{N_\alpha}\left(\theta + \frac{L_C\dot\theta}{V_\infty}\right) + C_{N_{\dot\alpha}}\dot\theta \\ &= C_{N_\alpha}\theta + \left(C_{N_{\dot\alpha}} + C_{N_\alpha}\frac{L_C}{V_\infty}\right)\dot\theta \\ &\triangleq C_{N_\alpha}\theta + \left(C_{N_{\dot\alpha}}\right)_{\text{tot}}\dot\theta \end{aligned} \tag{6.3.1-17}$$

where $\left(C_{N_{\dot{\alpha}}}\right)_{\text{tot}}$, total aerodynamic damping, is defined to be $C_{N_{\dot{\alpha}}} + C_{N_\alpha} L_C / V_\infty$.

Substitution from Equation (6.3.1-17) into (6.3.1-9) and then into (6.3.1-7) yields

$$A_z = -2q_\infty S_{\text{ref}} \left[\left(C_{N_{\dot{\alpha}}}\right)_{\text{tot}} \dot{\theta} + C_{N_\alpha} \theta \right] \tag{6.3.1-18}$$

and

$$\ddot{\theta} + \frac{2q_\infty S_{\text{ref}}}{m_C L} \left(C_{N_{\dot{\alpha}}}\right)_{\text{tot}} \dot{\theta} + \frac{1}{m_C L} \left[(m_C\, g - W_C) \sin\theta + 2q_\infty S_{\text{ref}} C_{N_\alpha} \theta \right] = 0 \tag{6.3.1-19}$$

The total weight of the system, W_{tot}, is equal to the sum of the weight of the load and the dry weight of the two parachutes (i.e., $W_{\text{tot}} = W_L + W_C$). During equilibrium descent in the $\hat{\mathbf{n}}_2 - \hat{\mathbf{n}}_3$ plane, the resultant axial force applied to the two parachutes balances the gravitational force $W_{\text{tot}} \hat{\mathbf{n}}_3$, resulting in zero acceleration in the vertical direction. Consequently, W_{tot} is equal to A_x, or $W_{\text{tot}} = A_x = 2q_\infty S_{\text{ref}} C_A$. Thus, $2q_\infty S_{\text{ref}}$ can be replaced with W_{tot}/C_A, and Equation (6.3.1-19) can be rewritten as

$$\ddot{\theta} + \frac{W_{\text{tot}}}{m_C L C_A} \left(C_{N_{\dot{\alpha}}}\right)_{\text{tot}} \dot{\theta} + \frac{1}{m_C L} \left[(m_C\, g - W_C) \sin\theta + \frac{W_{\text{tot}}}{C_A} C_{N_\alpha} \theta \right] = 0 \tag{6.3.1-20}$$

Over the past 50 years, a number of analytical, numerical, and experimental investigations have been performed, with the goal of understanding parachute pitch-plane dynamics (e.g., refs. 7 and 10). Reference 11 used computational fluid dynamics to study the stability of various main parachute configurations from the Apollo and MPCV Programs. It was demonstrated that an increase in the porosity of the parachute improved its stability characteristics, thus reducing the severity of the pendulum motion. Figure 6.3.1-2 shows representative plots of C_N and C_A, comparing a stable versus an unstable main parachute configuration. It is apparent from the C_N versus α plot that the unstable configuration has a negative slope at $\alpha = 0$ and two stable equilibrium points at $\pm\alpha_o$. As described in reference 11, by increasing the parachute porosity, the C_N slope becomes close to zero at $\alpha = 0$ and is considered the stable configuration. In addition, the two stable values α_o shift closer to $\alpha = 0$. However, this modification comes at a cost in the reduction of C_A, which results in a higher descent velocity. References 10 and 12 provide similar insight regarding the flow physics associated with non-porous versus porous configurations and how these affect the parachute stability characteristics. The current study focuses on the unstable Orion main parachute design (modeled by the red curves in Figure 6.3.1-2), which is highly susceptible to the pendulum motion under the two-main cluster configuration.

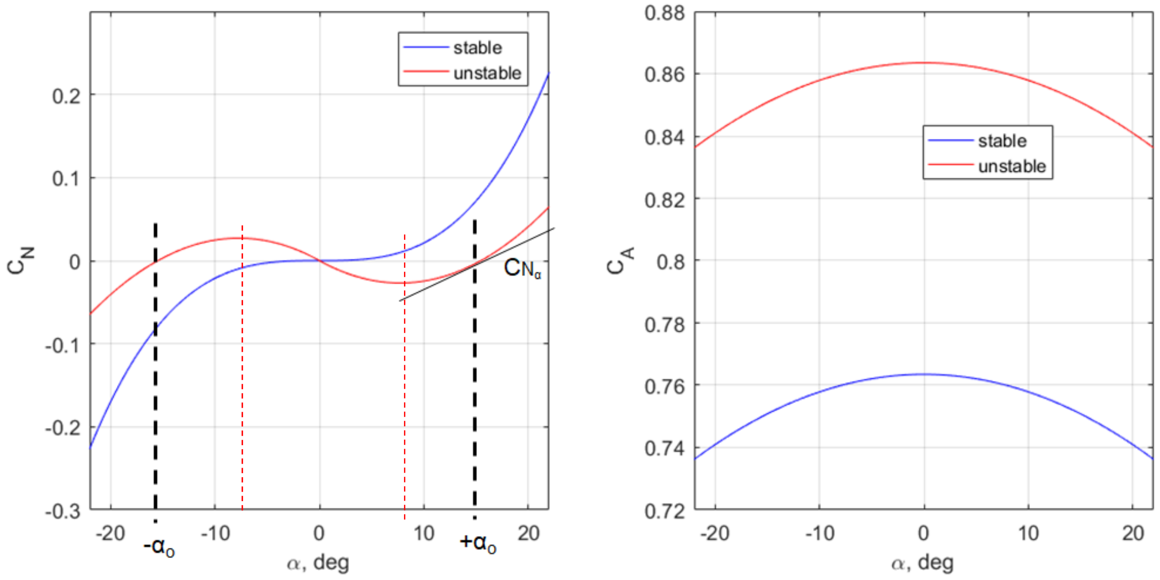

Figure 6.3.1-2. C_N and C_A Representative of Unstable and Stable Parachute Configurations

6.3.1.2 Linear Analysis

Much insight into the stability of the parachutes can be obtained by assuming that C_N is a linear function of α in the neighborhood of a stable equilibrium point, α_o. When the swing angle remains small, the rotational equation of motion is found to have the form of the second-order linear differential equation governing damped, free vibrations, and a general solution of the differential equation is given in Equation (6.3.1-25). A point on the dumbbell whose trajectory is nearly a straight line for undamped, small-amplitude oscillations is identified. The distance from this pivot point to the capsule is of interest because the capsule moves as though that distance is the length of a simple pendulum. In the case of a simple pendulum, the distance between the pivot point and the pendulum bob determines the distance traveled by the bob on a circular arc as the pendulum swings. The distance between the pivot point and the pendulum bob also determines the period of oscillation. Analogously, the distance from the pivot point to the capsule is an important parameter in capsule-parachute pendulum motion. When this distance is minimized, undesirable swinging motion of the capsule is minimized.

When θ remains small, Equation (6.3.1-20) can be approximated as

$$\ddot{\theta} + \frac{W_{\text{tot}}}{m_C L C_A}(C_{N_{\dot{\alpha}}})_{\text{tot}}\,\dot{\theta} + \frac{1}{m_C L}\left[(m_C\, g - W_C) + \frac{W_{\text{tot}}}{C_A}C_{N_\alpha}\right]\theta = 0 \qquad (6.3.1\text{-}21)$$

This second-order linear differential equation has the form

$$\ddot{x} + 2b\dot{x} + {\omega_n}^2 x = 0 \qquad (6.3.1\text{-}22)$$

which governs damped free vibrations. ω_n is referred to as the circular natural frequency, and b/ω_n is the fraction of critical damping or damping ratio. b and ${\omega_n}^2$ are defined as

$$b = \frac{W_{\text{tot}}}{2m_C L C_A}(C_{N_{\dot{\alpha}}})_{\text{tot}} \qquad (6.3.1\text{-}23)$$

and

$$\omega_n{}^2 = \frac{1}{m_C L}\left[(m_C\, g - W_C) + \frac{W_{\text{tot}}}{C_A} C_{N_\alpha}\right] \tag{6.3.1-24}$$

The general solution of Equation (6.3.1-21) is given by

$$\theta = e^{-bt}[C_1 \sin(\omega_d\, t) + C_2 \cos(\omega_d\, t)] \tag{6.3.1-25}$$

where the damped natural frequency, ω_d, is given by

$$\omega_d = \sqrt{\omega_n{}^2 - b^2} \tag{6.3.1-26}$$

and the constants C_1 and C_2 can be expressed in terms of the initial values $\theta_0 = \theta(t = 0)$ and $\dot{\theta}_0 = \dot{\theta}(t = 0)$ as

$$C_1 = \frac{1}{\omega_d}\left(\dot{\theta}_0 + b\theta_0\right) \tag{6.3.1-27}$$

$$C_2 = \theta_0 \tag{6.3.1-28}$$

The constants appearing in the fraction on the right-hand side of Equation (6.3.1-23) are all positive; therefore, the sign of b is determined by the sign of $(C_{N_{\dot{\alpha}}})_{\text{tot}}$. Exponential decay in θ occurs for $(C_{N_{\dot{\alpha}}})_{\text{tot}} > 0$, whereas there is exponential growth in θ for $(C_{N_{\dot{\alpha}}})_{\text{tot}} < 0$. In either case, the damped frequency ω_d of oscillations in θ is smaller than ω_n; consequently, the period of damped oscillations is larger than that of undamped oscillations.

Solutions of dynamical equations governing planar motions of the dumbbell reveal the existence of a point Q, on the line joining P_L and P_C, whose trajectory in N is very nearly a straight line; from this observation, it can be inferred that the magnitude of the acceleration ${}^N\mathbf{a}^Q$ of Q in N is nearly zero. In what follows, the distance L_L from P_L to Q is such that ${}^N\mathbf{a}^Q \cdot \hat{\mathbf{b}}_3 = 0$ for undamped oscillations having small amplitude. It is also shown that, under the same conditions, ${}^N\mathbf{a}^Q \cdot \hat{\mathbf{b}}_1$ is small when the initial values θ_0 and $\dot{\theta}_0$ are zero and small, respectively. Q is referred to as the pivot point; the smaller the value of L_L, the better the landing conditions will be for the capsule.

With the aid of Equation (6.3.1-5), the acceleration ${}^N\mathbf{a}^Q$ of Q in N is given by

$$\begin{aligned}{}^N\mathbf{a}^Q &= {}^N\mathbf{a}^{B^*} + (L_L - R_L)\left(\ddot{\theta}\,\hat{\mathbf{b}}_3 + \dot{\theta}^2\,\hat{\mathbf{b}}_1\right)\\ &= \left[\frac{(W_C + W_L)\cos\,\theta - A_x}{m_C + m_L} + (L_L - R_L)\dot{\theta}^2\right]\hat{\mathbf{b}}_1\\ &\qquad + \left[\frac{(W_C + W_L)\sin\,\theta + A_z}{m_C + m_L} + (L_L - R_L)\ddot{\theta}\right]\hat{\mathbf{b}}_3\end{aligned} \tag{6.3.1-29}$$

One can determine the value of L_L such that ${}^N\mathbf{a}^Q \cdot \hat{\mathbf{b}}_3 = 0$ when θ remains small and oscillations are undamped [ref. 5]:

$${}^N\mathbf{a}^Q \cdot \hat{\mathbf{b}}_3 = \frac{(W_C + W_L)\sin\,\theta + A_z - m_C L\ddot{\theta}}{m_C + m_L} + L_L\ddot{\theta} = 0 \tag{6.3.1-30}$$

In view of Equation (6.3.1-7) and the fact that $W_L = m_L\, g$,

$$\frac{(W_C + W_L)\sin\,\theta + (m_C\, g - W_C)\sin\,\theta}{m_C + m_L} + L_L\ddot{\theta} = g\sin\,\theta + L_L\ddot{\theta}\ = 0 \qquad (6.3.1\text{-}31)$$

Thus, after substitution from Equation (6.3.1-20) with $(C_{N_{\dot{\alpha}}})_{\text{tot}} = 0$,

$$-L_L\ddot{\theta} = \frac{L_L}{m_C L}\left[(m_C\, g - W_C)\sin\,\theta + \frac{W_{tot}}{C_A}C_{N_\alpha}\theta\right] = g\sin\,\theta \qquad (6.3.1\text{-}32)$$

When θ remains small, L_L can be expressed as

$$L_L = \frac{m_C\, g\, C_A}{(m_C\, g - W_C)C_A + W_{\text{tot}}C_{N_\alpha}}\,L \qquad (6.3.1\text{-}33)$$

It is easily shown that $L_L = R_L$ when $C_A = C_{N_\alpha}$, in which case Q is coincident with B^*. When $C_{N_\alpha} = 0$ (a hypothetical limiting case), it is evident that L_L slightly exceeds L because the numerator in Equation (6.3.1-33) becomes the sum of the masses of the dry parachutes and entrapped air, whereas the denominator consists only of the masses of entrapped air.

As the distance L_L decreases, the pivot point moves closer to the capsule, which decreases the distance the payload travels over a circular path during pendulum motion. Equation (6.3.1-33) is a key mathematical relationship that substantiates observations made in previous studies of pendulum motion:

1. Increasing the parachute C_{N_α} moves the pivot point toward the payload and reduces the distance traveled by the capsule as it swings. In other words, improving the static stability alleviates the severity of the pendulum motion.
2. Decreasing the parachute drag coefficient (by increasing its porosity) improves the static stability of the parachutes. In the context of the linear pendulum analysis, this is equivalent to moving the pivot point toward the payload and reducing the distance traveled by the capsule as it swings. However, this benefit comes at the expense of increasing the steady-state descent rate, which may not be desirable. Note that the overall stability of the pendulum motion is dependent on both static and dynamic stability. The latter is not addressed in this analysis.
3. Decreasing the payload mass (the largest contributor to W_{tot}) shifts the pivot point toward the parachutes and increases the distance traveled by the capsule as it swings.[1]
4. An increase in the atmospheric density increases the mass of the air entrapped in the canopy (the larger part of m_C) and moves the pivot point toward the parachutes.

These observations are consistent with conclusions drawn in references 7, 10, and 11.

---

[1] While this observation seems consistent with reference 7, experience from the CPAS drop tests suggests the opposite may be true. Half of the nominal two-parachute CPAS development drop tests experienced pendulum motion, but there were no observations of pendulum motion for the Capsule Pallet Separation System (CPSS), which used the same parachute configuration numerous times but with a payload that weighed about half as much. There may have been other contributing factors, and the number of tests is insufficient to draw a conclusion with high confidence; however, it is still worth noting this discrepancy as it directly applies to the parachute system analyzed in this study.

6.3.2 Flyout, Maypole, and Breathing Modal Analysis

The flyout (scissors), maypole, and breathing modes are described separately in this section. Reference 13 provides complete derivation of the equations of motion.

6.3.2.1 Flyout Mode

Reference 3 describes the flyout, or scissors, motion as two parachutes moving sinusoidally away from or toward the vertical axis in a symmetrical manner, while the capsule's descent speed changes sinusoidally. A simple planar model involving three particles is used to study the underlying dynamics of the scissors motion, as shown in Figure 6.3.2.1-1. Particle P_L has a mass of m_L and represents the capsule. The two parachutes are treated as identical particles, P_B and P_C; each has a mass of m_C, which includes dry mass as well as the mass of air trapped inside the canopy. The system moves such that the three particles remain at all times in a plane fixed in a Newtonian reference frame N. A right-handed set of mutually perpendicular unit vectors $\hat{\mathbf{n}}_1$, $\hat{\mathbf{n}}_2$, and $\hat{\mathbf{n}}_3$ is fixed in N. Unit vectors $\hat{\mathbf{n}}_1$ and $\hat{\mathbf{n}}_3$ lie in the plane in which motion takes place and are directed as shown in Figure 6.3.2.1-1; $\hat{\mathbf{n}}_1$ is horizontal, $\hat{\mathbf{n}}_2$ is directed out of the page, and $\hat{\mathbf{n}}_3$ is vertical, directed downward. P_B and P_C each are connected to P_L by a massless, rigid link; the two links are connected by a revolute joint whose axis is parallel to $\hat{\mathbf{n}}_2$. P_B and one link are fixed in a reference frame B, whereas P_C and the other link are fixed in a reference frame C. The orientations of B and C in N are described by angles θ_1 and θ_2, respectively. A dextral set of mutually perpendicular unit vectors $\hat{\mathbf{b}}_1$, $\hat{\mathbf{b}}_2$, and $\hat{\mathbf{b}}_3$ is fixed in B and directed as shown in Figure 6.3.2.1-1; $\hat{\mathbf{b}}_2$ is directed out of the page. A similar set of unit vectors $\hat{\mathbf{c}}_1$, $\hat{\mathbf{c}}_2$, and $\hat{\mathbf{c}}_3$ is fixed in C; $\hat{\mathbf{c}}_2$ is directed into the page. Note that $\hat{\mathbf{b}}_2$ and $\hat{\mathbf{c}}_2$ are each fixed in the three reference frames N, B, and C. The resultant external forces acting on P_L, P_B, and P_C are denoted by $\mathbf{F}_L$, $\mathbf{F}_B$, and $\mathbf{F}_C$, respectively.

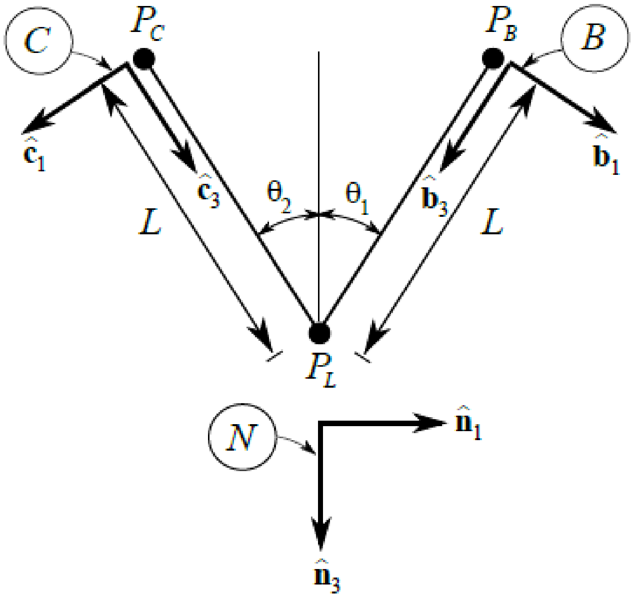

Figure 6.3.2.1-1. Scissors Mode Planar Model

The equation of motion governing the horizontal speed of P_L, which is not presented, shows that horizontal acceleration of P_L vanishes under the following conditions: $(\mathbf{F}_L + \mathbf{F}_B + \mathbf{F}_C) \cdot \hat{\mathbf{n}}_1 = 0$,

$\theta_1 = \theta_2$, $\dot{\theta}_1 = \dot{\theta}_2$, and $\ddot{\theta}_1 = \ddot{\theta}_2$. The latter three conditions simply correspond to the symmetric motion of the parachutes that characterizes the scissors behavior under consideration. In the following, all four conditions are assumed to exist, and the horizontal speed of P_L is taken to be constant and equal to zero. In that case, the three-particle system has three DOFs in N, and three motion variables u_1, u_2, and u_3 are introduced as follows: u_1 is the projection onto $\hat{\mathbf{n}}_3$ of the velocity of P_L in N, $u_2 = \dot{\theta}_1$, and $u_3 = \dot{\theta}_2$. Using Kane's method [ref. 14], the equations of motion can be written in matrix form as

$$\begin{bmatrix} m_L + 2m_C & m_C L \sin\,\theta_1 & m_C L \sin\,\theta_2 \\ m_C L \sin\,\theta_1 & m_C L^2 & 0 \\ m_C L \sin\,\theta_2 & 0 & m_C L^2 \end{bmatrix} \begin{Bmatrix} \dot{u}_1 \\ \dot{u}_2 \\ \dot{u}_3 \end{Bmatrix} = \begin{Bmatrix} \hat{\mathbf{n}}_3 \cdot (\mathbf{F}_L + \mathbf{F}_B + \mathbf{F}_C) - m_C L(\cos\,\theta_1\, u_2{}^2 + \cos\,\theta_2\, u_3{}^2) \\ L\hat{\mathbf{b}}_1 \cdot \mathbf{F}_B \\ L\hat{\mathbf{c}}_1 \cdot \mathbf{F}_C \end{Bmatrix} \tag{6.3.2-1}$$

The mass matrix is symmetric, as expected. One can divide the second and third equations by L. Symmetric motion of the parachutes occurs when the magnitude of the normal force $\hat{\mathbf{b}}_1 \cdot \mathbf{F}_B$ applied to P_B is identical to the magnitude of the normal force $\hat{\mathbf{c}}_1 \cdot \mathbf{F}_C$ applied to P_C, the initial values of θ_1 and θ_2 are identical, and the initial values of u_2 and u_3 are identical.

According to reference 7, the contribution of aerodynamic forces to $\mathbf{F}_L$ is ignored, and the force can be expressed as

$$\mathbf{F}_L = m_L g \hat{\mathbf{n}}_3 = W_L \hat{\mathbf{n}}_3 \tag{6.3.2-2}$$

The resultant external force applied to P_B is given by

$$\mathbf{F}_B = q_\infty S_{\text{ref}}[-(C_N)_{\text{tot}}\hat{\mathbf{b}}_1 - C_A \hat{\mathbf{b}}_3] + W_C \hat{\mathbf{n}}_3 \tag{6.3.2-3}$$

where W_C is the dry weight of a single parachute. The weight of the air trapped in the canopy is ignored because the gravitational force exerted on that air is assumed to be counteracted by buoyancy effects from the ambient atmosphere. The total normal force coefficient, $(C_N)_{\text{tot}}$, is the sum of the free-stream normal force coefficient, $(C_N)_{\text{fs}}$, and the normal force coefficient due to parachute proximity effects, $(C_N)_{\text{prox}}$:

$$(C_N)_{\text{tot}} = (C_N)_{\text{fs}} + (C_N)_{\text{prox}} \tag{6.3.2-4}$$

As shown in Figure 6.3.1-2 and Equation (6.3.1-11), $(C_N)_{\text{fs}}$ is generally a nonlinear function of α. In general, it is also a function of $\dot{\alpha}$. For this analysis it is assumed that the parachutes are oscillating about some trimmed α. Small angles are assumed, $\theta' \approx \alpha'$, where θ' and α' are deviations about the trimmed θ and α, respectively, and C_N varies linearly with α. This small angle assumption is valid for α' within approximately 15 degrees; however, this is not generally the case, which may introduce significant errors. $(C_N)_{\text{prox}}$ is a function of D_{prox}, the distance between the parachute centers, and V_{prox}, the time derivative of D_{prox}. Proximity distance can be expressed as $D_{\text{prox}} = 2L \sin\,\theta$; thus, its time derivative is $V_{\text{prox}} = 2L \cos\,\theta\,\dot{\theta}$. The derivatives of the normal force coefficients have a relationship similar to Equation (6.3.2-4):

$$(C_{N_\alpha})_{\text{tot}} = (C_{N_\alpha})_{\text{fs}} + (C_{N_\alpha})_{\text{prox}} \tag{6.3.2-5}$$

The resultant external force applied to P_C is given by

$$\mathbf{F}_C = q_\infty S_{\text{ref}}[-(C_N)_{\text{tot}}\hat{\mathbf{c}}_1 - C_A\hat{\mathbf{c}}_3] + W_C\hat{\mathbf{n}}_3 \tag{6.3.2-6}$$

If the dynamic coupling in Equations (6.3.2-1) is ignored (valid approximation since the contribution of $\dot{u}_1$ to $\dot{u}_2$ is small), damping is neglected, and θ_1 is assumed to remain small, then the second of Equations (6.3.2-1) describes an undamped harmonic oscillation:

$$\dot{u}_2 = \ddot{\theta}_1 \approx \frac{W_C - q_\infty S_{\text{ref}}(C_{N_\alpha})_{\text{tot}}}{m_C L}\,\theta_1 \tag{6.3.2-7}$$

The period associated with the scissors motion, T, is found to be inversely proportional to $(C_{N_\alpha})_{\text{tot}}$:

$$T = 2\pi\sqrt{\frac{m_C L}{q_\infty S_{\text{ref}}(C_{N_\alpha})_{\text{tot}} - W_C}} \tag{6.3.2-8}$$

$(C_{N_\alpha})_{\text{tot}}$ can be expressed as a function of T and key system parameters:

$$(C_{N_\alpha})_{\text{tot}} = \frac{1}{q_\infty S_{\text{ref}}}\left(\frac{4\pi^2 m_C L}{T^2} + W_C\right) \tag{6.3.2-9}$$

6.3.2.2 Maypole Mode

Maypole motion described in reference 2 consists of two parachutes orbiting about the vertical axis. It is referred to as the spiral mode in reference 12. A simplified model used to study maypole motion is illustrated in Figure 6.3.2.2-1. The three particles P_L, P_B, and P_C are the same as those described in Section 6.3.2.1; in the present model, however, all three are assumed to be fixed in a rigid body B. A right-handed set of mutually perpendicular unit vectors $\hat{\mathbf{b}}_1$, $\hat{\mathbf{b}}_2$, and $\hat{\mathbf{b}}_3$ is fixed in B and directed as shown in Figure 6.3.2.2-1; $\hat{\mathbf{b}}_2$ is normal to the plane containing P_L, P_B, and P_C; and $\hat{\mathbf{b}}_3$ is parallel to an axis of symmetry of B, which is therefore a central principal axis of inertia of B. A dextral set of mutually perpendicular unit vectors $\hat{\mathbf{n}}_1$, $\hat{\mathbf{n}}_2$, and $\hat{\mathbf{n}}_3$ is fixed in a Newtonian reference frame N. $\hat{\mathbf{n}}_1$ is horizontal, $\hat{\mathbf{n}}_2$ is directed out of the page, and $\hat{\mathbf{n}}_3$ is vertical, directed downward. B moves in N such that $\hat{\mathbf{b}}_3 = \hat{\mathbf{n}}_3$ at all times. Moreover, the velocity in N of every point on the axis of symmetry of B has the same constant magnitude and the same direction as $\hat{\mathbf{n}}_3$.

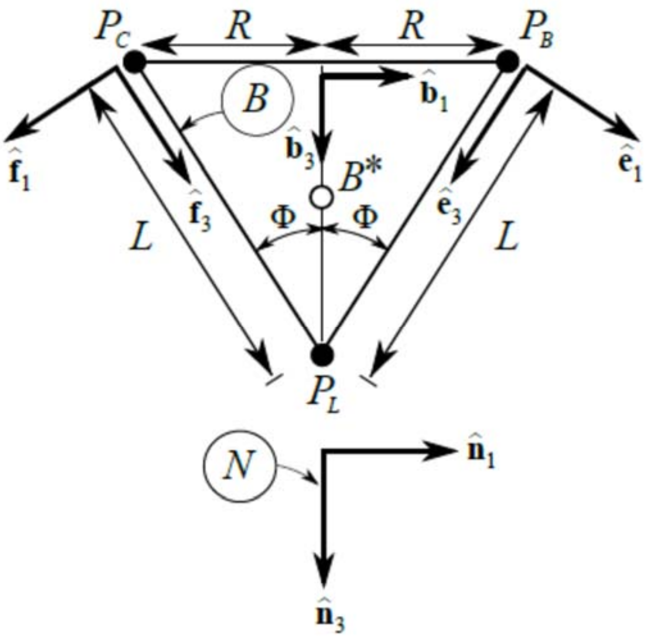

Figure 6.3.2.2-1. Maypole Mode Model

For example, P_L lies on the axis of symmetry, so the velocity of P_L in N can be written as

$$^{N}\mathbf{v}^{P_L} = V_3\hat{\mathbf{n}}_3 \tag{6.3.2-10}$$

where V_3 is a constant. Hence, the acceleration in N of P_L and every point on the axis of symmetry is zero:

$$^{N}\mathbf{a}^{P_L} = \mathbf{0} \tag{6.3.2-11}$$

The mass center of B, denoted by B^*, lies on the axis of symmetry and, therefore, has an acceleration in N equal to zero. Based on first principles, this requires that the resultant of all external forces applied to B is equal to zero. The angular velocity $^{N}\boldsymbol{\omega}^{B}$ of B in N that characterizes maypole motion is parallel to a central principal axis of inertia of B:

$$^{N}\boldsymbol{\omega}^{B} = \Omega\hat{\mathbf{b}}_3 = \Omega\hat{\mathbf{n}}_3 \tag{6.3.2-12}$$

where Ω is a constant. Thus, the angular acceleration $^{N}\boldsymbol{\alpha}^{B}$ of B in N is zero:

$$^{N}\boldsymbol{\alpha}^{B} = \mathbf{0} \tag{6.3.2-13}$$

Euler's rotational equations of motion are satisfied by Equations (6.3.2-12) and (6.3.2-13) only if the resultant moment about B of all external forces applied to B is equal to zero. The accelerations in N of P_B and P_C are then determined to be

$$^{N}\mathbf{a}^{P_B} = \Omega L \sin\,\Phi\;\Omega\hat{\mathbf{b}}_3 \times \hat{\mathbf{b}}_2 = -R\Omega^2\hat{\mathbf{b}}_1 \tag{6.3.2-14}$$

$$^{N}\mathbf{a}^{P_C} = -\Omega L \sin\,\Phi\;\Omega\hat{\mathbf{b}}_3 \times \hat{\mathbf{b}}_2 = R\Omega^2\hat{\mathbf{b}}_1 \tag{6.3.2-15}$$

where $R = L\sin\,\Phi$, as indicated in Figure 6.3.2.2-1.

Two additional sets of dextral, mutually perpendicular unit vectors are introduced for convenience in conducting kinematic analysis and expressing the forces applied to B. Both sets of unit vectors are fixed in B. The first set contains $\hat{\mathbf{e}}_1$, $\hat{\mathbf{e}}_2$, and $\hat{\mathbf{e}}_3$, whereas the second set contains $\hat{\mathbf{f}}_1$, $\hat{\mathbf{f}}_2$, and $\hat{\mathbf{f}}_3$.

The resultants of the external forces acting on P_L, P_B, and P_C are once again denoted by $\mathbf{F}_L$, $\mathbf{F}_B$, and $\mathbf{F}_C$, respectively. As in Section 6.3.2.1, $\mathbf{F}_L$ is expressed as

$$\mathbf{F}_L = m_L g \hat{\mathbf{n}}_3 = W_L \hat{\mathbf{n}}_3 \tag{6.3.2-16}$$

The resultant external force applied to P_B is, in general, given by

$$\mathbf{F}_B = q_\infty S_{\text{ref}}[-(C_N)_{\text{tot}} \hat{\mathbf{e}}_1 + C_Y \hat{\mathbf{e}}_2 - C_A \hat{\mathbf{e}}_3] + W_C \hat{\mathbf{n}}_3 \tag{6.3.2-17}$$

where W_C is the dry weight of a single parachute. $(C_N)_{\text{tot}}$ can in this case be expressed as in Equation (6.3.2-4). In addition, it is assumed that $\Phi = \alpha$ and the parachutes are in static equilibrium with constant flyout angles and at some trimmed angle of attack α_{trim} while performing the maypole motion. The resultant external force applied to P_C is similar to F_B:

$$\mathbf{F}_C = q_\infty S_{\text{ref}}[-(C_N)_{\text{tot}} \hat{\mathbf{f}}_1 + C_Y \hat{\mathbf{f}}_2 - C_A \hat{\mathbf{f}}_3] + W_C \hat{\mathbf{n}}_3 \tag{6.3.2-18}$$

However, the side forces associated with C_Y would yield a nonzero moment about B^* that is parallel to $\hat{\mathbf{b}}_3$. Hence, maypole motion requires

$$C_Y = 0 \tag{6.3.2-19}$$

Because P_L and P_B are connected by a rigid link, each exerts a force on the other. The force exerted by P_L on P_B can be expressed as $T\hat{\mathbf{e}}_3$. This internal force must be accounted for when applying Newton's second law to P_B; however, forming dot products with $\hat{\mathbf{e}}_1$ will eliminate T. That is,

$$(\mathbf{F}_B + T\hat{\mathbf{e}}_3) \cdot \hat{\mathbf{e}}_1 = \mathbf{F}_B \cdot \hat{\mathbf{e}}_1 = m_C {}^N\mathbf{a}^{P_B} \cdot \hat{\mathbf{e}}_1 \tag{6.3.2-20}$$

Substitution from Equations (6.3.2-14) and (6.3.2-17) yields

$$\begin{aligned} \{q_\infty S_{\text{ref}}[-(C_N)_{\text{tot}} \hat{\mathbf{e}}_1 - C_A \hat{\mathbf{e}}_3] + W_C \hat{\mathbf{n}}_3\} \cdot \hat{\mathbf{e}}_1 &= -q_\infty S_{\text{ref}} (C_N)_{\text{tot}} + W_C \sin\,\Phi \\ &= -m_C R \Omega^2 \hat{\mathbf{b}}_1 \cdot \hat{\mathbf{e}}_1 \\ &= -m_C R \Omega^2 \cos\,\Phi \end{aligned} \tag{6.3.2-21}$$

This relationship can be solved for $(C_N)_{\text{tot}}$:

$$(C_N)_{\text{tot}} = \frac{m_C R \Omega^2 \cos\,\Phi + W_C \sin\,\Phi}{q_\infty S_{\text{ref}}} \tag{6.3.2-22}$$

Thus, the aerodynamic normal force is seen to be directly proportional to the magnitude of the centripetal acceleration of P_B (or P_C). One can also conclude that the radius and period of the maypole mode is dependent on the value of $(C_N)_{\text{tot}}$ at α_{trim}. For a given orbital radius, R, the orbital angular rate is given by

$$\Omega = \sqrt{\frac{q_\infty S_{\text{ref}} (C_N)_{\text{tot}} - W_C \sin\,\Phi}{m_C R \cos\,\Phi}} \tag{6.3.2-23}$$

The orbital period of maypole motion is thus seen to be inversely proportional to $(C_N)_{\text{tot}}$.[2] Finally, by appealing to the fact that the resultant external force applied to B must be $\mathbf{0}$ for maypole motion to take place, a relationship between $(C_N)_{\text{tot}}$ and C_A can be obtained. The resultant is given by

$$\begin{aligned}\mathbf{F}_B + \mathbf{F}_C + \mathbf{F}_L = q_\infty S_{\text{ref}}[-(C_N)_{\text{tot}}(\hat{\mathbf{e}}_1 + \hat{\mathbf{f}}_1) - C_A(\hat{\mathbf{e}}_3 + \hat{\mathbf{f}}_3)] \\ + (2W_C + W_L)\hat{\mathbf{n}}_3 = \mathbf{0}\end{aligned} \tag{6.3.2-24}$$

Hence,

$$\begin{aligned}(\mathbf{F}_B + \mathbf{F}_C + \mathbf{F}_L) \cdot \hat{\mathbf{b}}_3 &= \{q_\infty S_{\text{ref}}[-(C_N)_{\text{tot}}(\hat{\mathbf{e}}_1 + \hat{\mathbf{f}}_1) - C_A(\hat{\mathbf{e}}_3 + \hat{\mathbf{f}}_3)] + (2W_C + W_L)\hat{\mathbf{n}}_3\} \cdot \hat{\mathbf{b}}_3 \\ &= -q_\infty S_{\text{ref}}[2(C_N)_{\text{tot}} \sin\,\Phi + 2C_A \cos\,\Phi)] + 2W_C + W_L \\ &= 0\end{aligned} \tag{6.3.2-25}$$

or

$$(C_N)_{\text{tot}} = \frac{2W_C + m_L g - 2q_\infty S_{\text{ref}} C_A \cos\,\Phi}{2q_\infty S_{\text{ref}} \sin\,\Phi} \tag{6.3.2-26}$$

6.3.2.3 Breathing Mode

Parachutes are made using flexible materials and are inherently non-rigid objects. As they deform during flight, the projected reference area S_{proj} changes and affects the axial motion of the system. Reference 2 describes this axial oscillatory behavior as the “breathing mode.” Cluster Development Test (CDT) 3-02 flight test data showed that during the breathing mode as the canopies contracted from the nominal reference area, V_{down} increased; conversely, as the canopies increased from the nominal reference area, V_{down} decreased. This oscillatory behavior occurred with a period of 4.5 seconds.

The underlying dynamics of the breathing mode are straightforward and can be represented by Equations (6.3.2-27) through (6.3.2-29). The parameter η is used to approximate the deformation of the parachute away from its nominal projected area, with $\eta < 0$ depicting a contracted canopy and $\eta > 0$ an expanded canopy. The oscillatory deformation behavior can be represented by a second-order harmonic oscillator. The natural frequency, ω_n, is dependent on many parameters (e.g., the parachute material properties, porosity, natural environments).

$$\ddot{\eta} + d\dot{\eta} + \omega_n^2 \eta = 0 \tag{6.3.2-27}$$

The C_A consists of a baseline term and a term dependent on η:

$$C_A = C_{A_0} + C_{A_\eta} \eta \tag{6.3.2-28}$$

The equation of motion in the down direction is

$$(m_L + 2m_{C,\text{dry}})\dot{w} = S_{\text{ref}} \rho w^2 C_A + (m_L + 2m_{C,\text{dry}})g \tag{6.3.2-29}$$

where $m_{C,\text{dry}}$ is the dry mass of the parachutes and w is the velocity in the down direction.

---

[2] This conclusion appears to contradict the findings in reference 12, which suggests that the orbital period increases with C_N. However, the authors of reference 12 state that those results are only applicable to a narrow range of initial conditions, which may explain the discrepancy.

6.3.3 Independent Parachute/Capsule Simulations Implementing Full Three-object Nonlinear Equations of Motion

A MATLAB-based standalone CAPDYN simulation was created to investigate the motion of a generic crew module capsule connected to one or two parachutes. MATLAB was selected for the simulation for greater ease in integrating it with existing MATLAB-based system identification tools. CAPDYN is a complex, multiple DOF simulation that models the interaction of one or two parachutes connected with flexible riser lines (modeled as springs with damping that apply tension-only forces along the direction of the lines) to a crew module capsule, each under the influence of forces due to gravitational attraction, aerodynamics, and the force exerted by each riser line. The gravitational force exerted on the air entrapped in each canopy is assumed to be counteracted by buoyancy effects from the ambient atmosphere.

6.3.3.1 CAPDYN Notations

Many authors use different and varied notations for expressing vector quantities, as well as direction cosine matrices (DCMs) and quaternions. This section explains the notations used herein. To define a vector that is directed from one point “A” to another point “B,” the notation $\underline{\mathbf{R}}_{B/A}$ is used. With this notation, no specific coordinate frame is implied. To identify the coordinate frame in which a vector is expressed, the vector is enclosed in parentheses with a subscript identifying the frame. For example, if the vector $\underline{\mathbf{R}}_{B/A}$ is expressed in the North-East-Down (NED) frame (defined in the next section), then it is denoted by $(\underline{\mathbf{R}}_{B/A})_{NED}$. If the vector $\underline{\mathbf{R}}_{B/A}$ is expressed in the capsule body frame (“b”) (also defined in the next section), then it is denoted by $(\underline{\mathbf{R}}_{B/A})_{b}$.

Likewise, DCM and quaternion notation used herein employs a similar notation. Assume some quaternion represents the orientation of coordinate frame “C” relative to the axes of coordinate frame “D,” then the quaternion that represents the orientation of frame D relative to frame C is written as $\underline{\mathbf{q}}_{D/C}$, which can be thought of as the quaternion that transforms vectors *from* frame C *to* frame D. Similarly, a DCM expressing the relative orientations of those frames could be denoted as $\boldsymbol{C}_{D/C}$.

Throughout this document, the orientations of coordinate frames is defined using quaternions rather than DCMs, although either is mathematically suitable. However, throughout the mathematical literature, there are two forms of quaternions, which are distinguished by how they are used. One form of quaternion seen in mathematical literature is used to rotate a specified vector through some angle in a right-hand sense about some direction as defined by the quaternion. The other form used in flight mechanics applications (and in this document) describes the relative orientations of two different coordinate frames in which the components of a common vector are defined. In the latter application used herein, the vector itself is not rotated by the quaternion; rather, a common fixed vector as observed in two coordinate frames whose relative orientations are defined by a quaternion can be transformed from one frame to the other using that quaternion. The defining relationship between a vector expressed in coordinate frame C, or $(\underline{\mathbf{R}})_C$, and the same vector expressed in another coordinate frame D, or $(\underline{\mathbf{R}})_D$, is provided in the quaternion notation used herein as the following quaternion product of three quaternions: $(\underline{\mathbf{R}})_D = (\underline{\mathbf{q}}_{D/C})^* \ (\underline{\mathbf{R}})_C \ \ \underline{\mathbf{q}}_{D/C}$. The middle quaternion shown on the right-hand side of the equation is a quaternion representation of the vector being transformed, with zero scalar part, and vector part equal to the components of the vector $(\underline{\mathbf{R}})_C$. The asterisk superscript on the leading quaternion on the right side of the equation represents the conjugate of quaternion $\underline{\mathbf{q}}_{D/C}$.

6.3.3.2 CAPDYN Coordinate Frames

For the equation of motion derived herein, a right-handed reference frame with its x-axis pointed north, its y-axis pointed east, and its z-axis pointed down with its origin placed at some arbitrary location is defined as the NED frame. For the purposes of this analysis, oblate or spherical Earth geometry and kinematics are not considered, nor is the rotation of the Earth or its orbit around the Sun. Per these simplifications, the NED frame is considered an inertial frame for applying Newton's laws of motion. The precise location of the origin of the NED frame is arbitrary and, without loss of generality, in this analysis is assumed to be located on the surface of the Earth somewhere in the general vicinity of the three bodies being analyzed (i.e., the capsule and each of the two parachutes).

Additionally, the analysis described herein does not model the inverse-square gravity model ($g = \mu/r^2$, where r is the distance from the center of the Earth to the center of mass (CM) of an object, including its altitude above the surface of the spherical or oblate Earth, and μ is the product of the gravitational constant and the mass of the Earth). Instead of the inverse-square gravity model, the analyses described herein use a fixed value of gravity at the mean surface of the Earth, or 9.80665 meters per second squared (m/s^2), or 32.17405 ft/s^2, which is assumed to be constant at all altitudes.

The capsule includes two coordinate frames defined as the *capsule structural reference frame* and the *capsule body frame*. The capsule structural frame is used to define the location of specific elements of the capsule geometry and the placement of items in the capsule. Its x-axis is located along the axis of symmetry of the capsule with its direction pointed aft, toward the capsule heat shield; its y-axis points toward the crew entry hatch, and its z-axis completes a right-handed coordinate frame. Its origin is arbitrary and is normally positioned some distance forward of the capsule's top, and it is sometimes defined as the virtual point that is the apex of the capsule's conical shape. However, the precise location is not important for the derivation of the equation of motion in this document (the relative locations of items of interest in the capsule are important).

The capsule body frame is a right-handed coordinate frame with its origin located at the CM of the capsule with its x-axis pointed forward or away from the crew module heat shield; its y-axis is parallel to the y-axis of the capsule structural frame, and its z-axis completes a right-handed coordinate frame. The axes of the capsule body frame are rotated 180 degrees about the y-axis compared with the capsule structural reference frame, and its origin is offset from the origin of the capsule structural frame. It is offset axially along the axis of symmetry from the arbitrary location specified for the origin of the capsule structural frame to the actual CM of the capsule. In general, it is located off the axis of symmetry of the capsule due to the non-zero lateral CM location of the capsule relative to its axis of symmetry. The distribution of mass in the capsule is designed intentionally so that its CM is offset from the axis of symmetry to allow the desired steady-state "hang angle" of the capsule as it descends under the influence of its parachutes.

Figure 6.3.3.2-1 is a depiction of the crew module geometry showing the two coordinate frames and their relative positions and orientation.

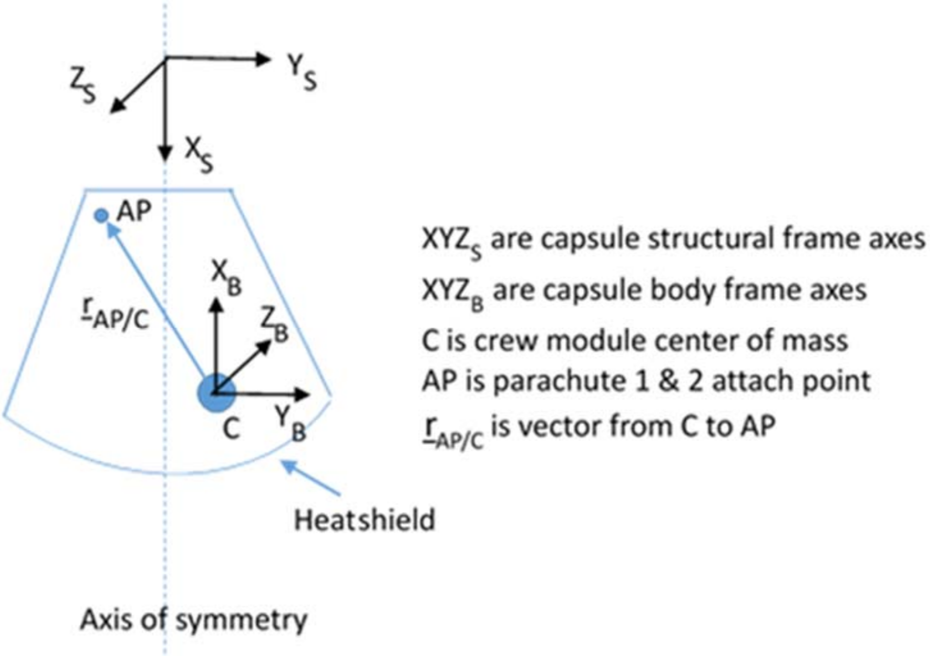

Figure 6.3.3.2-1. Capsule Coordinate Frame Definitions

Each parachute is modeled as a “point mass” whose dynamics are influenced only by forces exerted on them from aerodynamics, tension in the riser lines connecting them to the capsule, and gravity, resulting in three translational DOFs for each parachute. The parachute orientations change due to the translation of each parachute relative to the attach point on the capsule, while connected by their riser lines to the capsule. The parachutes are not modeled as rigid bodies with specified moments of inertia whose rotational dynamics could be computed by moments applied to them. However, the rotational orientation of the parachute canopies caused by their translation relative to their attach point on the capsule is obtained in these derivations by consideration of the kinematics of such motion.

For the purposes of the derivations included herein, each parachute is assumed to be a point mass with no rotational dynamics. Affixed to each parachute is a “wind” reference frame whose origin is located at the point-mass representation of the parachute mass at a specified distance above the plane of the opening to the parachute canopy’s hemispherical shape and along its axis of symmetry. Such a parachute “wind” reference frame allows for traditional aerodynamic forces to be applied to the parachutes using air relative velocity and angle of attack. For the purposes of the derivations herein, the x-axis of each parachute “wind” reference frame is defined such that it points toward its attach point on the capsule, in the direction of its riser line force that connects it to the crew-module attach point. Its z-axis is defined such that the instantaneous air relative velocity vector (i.e., the velocity of each parachute relative to winds applied to it) is contained in the parachute wind frame x-z plane. Finally, the y-axis of each parachute wind frame completes a right-handed reference frame. As a consequence of these parachute “wind” reference frame definitions, the orientations of the axes continually change relative to NED as each parachute’s air relative velocity vector changes direction due to parachute translational motion and winds applied, and due to the effects of the forces from the riser lines connecting the parachutes to the capsule. Due to the definitions used for the parachute wind reference-frame axes, the total angle of attack of each parachute is contained in the x-z plane with no sideslip aerodynamic angle in the y-axis directions, as for “wind axis” coordinate frames often described in airplane and missile aerodynamic and dynamics analyses. However, these definitions of the x-, y-, z-axes do not preclude applying aerodynamic forces along the y-axis of each parachute.

Figure 6.3.3.2-2 is a depiction of the relative orientations and positions of the two parachutes relative to the capsule and the inertial NED frame. The figure shows the parachute “wind” reference-frame axis definitions as described and the geometric parameters used to define the relative orientation and position of each parachute from the capsule.

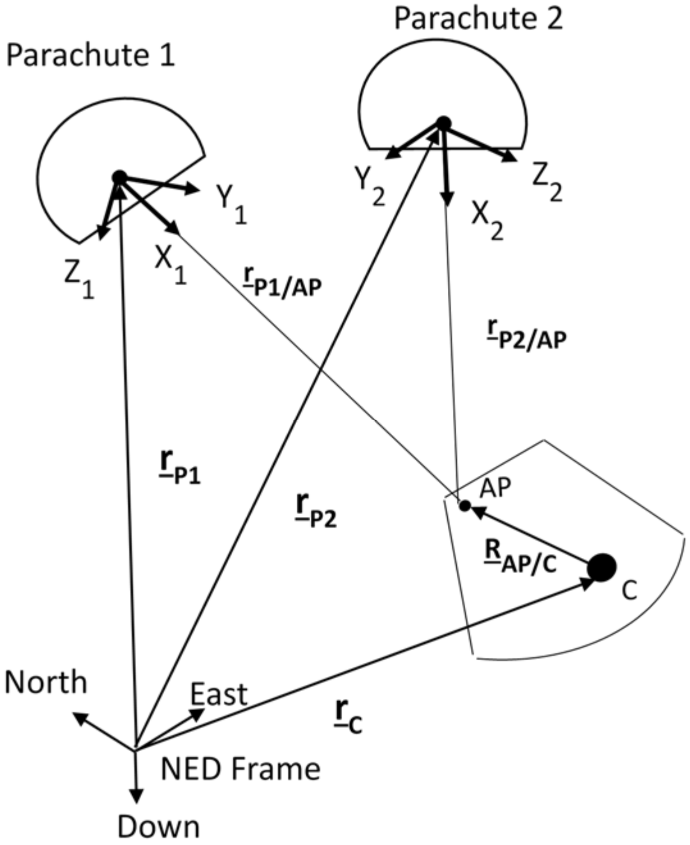

Figure 6.3.3.2-2. Parachute Wind Reference Frame Definitions

6.3.3.3 Parachute Equations of Motion

The forces applied to each parachute and the forces and moments applied to the capsule are created by aerodynamic, gravity, and tension forces in the riser lines that connect each parachute with its corresponding attach point on the capsule. The riser lines are considered elastic lines that apply tension-only forces modeled as springs with damping (numerical values are provided in Table 7.1-1). Those forces and moments are shown in the free-body diagrams of each parachute and the capsule in Figure 6.3.3.3-1.

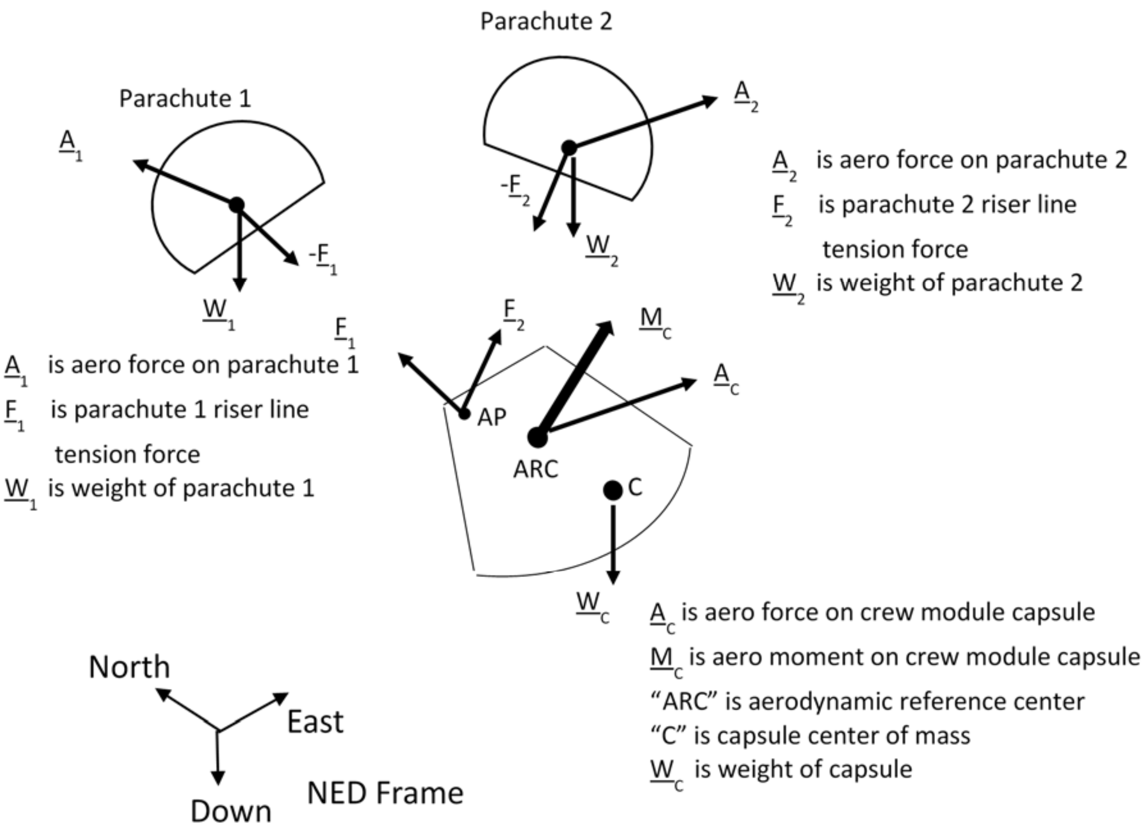

Figure 6.3.3.3-1. Free-body Diagram of Three-object Equation of Motion

The forces applied to each parachute by the riser lines connecting them to the capsule are, by Newton's third law of motion, equal in magnitude and opposite in direction to the forces applied by the riser lines to the capsule. This is illustrated in Figure 6.3.3.3-1 by the vectors $\underline{\mathbf{F}}_1$ and $-\underline{\mathbf{F}}_1$ and $\underline{\mathbf{F}}_2$ and $-\underline{\mathbf{F}}_2$ as identified in the free-body diagram of each body. Since the riser lines are assumed to provide tension-only connections that allow line stretch but no compression forces, the force provided by each riser line is consistent with modeling as a spring with damping so that the force applied is computed as shown in Equations (6.3.3-1) through (6.3.3-3):

$$\underline{\mathbf{F}}_1 = T_1\,\underline{\hat{\mathbf{n}}}_1 \qquad \underline{\mathbf{F}}_2 = T_2\,\underline{\hat{\mathbf{n}}}_2 \tag{6.3.3-1}$$

$$T_1 = k_T{}^*\,(\boldsymbol{\ell}_1 - \boldsymbol{\ell}_{1\_initial}) + k_D\,\dot{\boldsymbol{\ell}}_1 \tag{6.3.3-2}$$

$$T_2 = k_T{}^*\,(\boldsymbol{\ell}_2 - \boldsymbol{\ell}_{2\_initial}) + k_D\,\dot{\boldsymbol{\ell}}_2 \tag{6.3.3-3}$$

In the equations above, k_T is the spring constant (lbf/ft), k_D is the spring damping constant (lbf-s/ft), $\boldsymbol{\ell}_1$ and $\boldsymbol{\ell}_2$ are the current lengths of the riser lines for parachutes 1 and 2, $\boldsymbol{\ell}_{1\text{initial}}$ and $\boldsymbol{\ell}_{2\text{initial}}$ are the initial (unstretched) lengths of the parachute riser lines, and the $\boldsymbol{\ell}_1$ and $\boldsymbol{\ell}_2$ dot terms are the rates of change of the riser line lengths. The unit vectors from the parachute attach point on the capsule to each parachute are computed as shown in Equations (6.3.3-4):

$$\underline{\hat{\mathbf{n}}}_1 = \frac{\underline{\mathbf{r}}_{P1/AP}}{\left|\underline{\mathbf{r}}_{P1/AP}\right|} \tag{6.3.3-4a}$$

$$\underline{\hat{\mathbf{n}}}_2 = \frac{\underline{\mathbf{r}}_{\mathrm{P2/AP}}}{\left|\underline{\mathbf{r}}_{\mathrm{P2/AP}}\right|} \tag{6.3.3-4b}$$

If the unit vectors shown in Equations (6.3.3-4) are computed in the NED reference frame, then they can be transformed to the capsule body frame, b, as needed.

For the purposes of this analysis, it is assumed that the aerodynamic forces exerted on the two parachutes ($\underline{\mathbf{A}}_1$ and $\underline{\mathbf{A}}_2$, as shown in Figure 6.3.3.3-1) will be specified in the parachute's wind frame as described earlier, using typical aerodynamic conventions with axial force applied opposite its x-axis, normal force applied opposite its z-axis, and side force applied in the direction of its y-axis. The total angle of attack will be computed in Equation (6.3.3-10b) to compute the aerodynamic force coefficients, and the aerodynamic forces will be computed from those coefficients and each parachute's aerodynamic reference area and dynamic pressure. The aerodynamic coefficients C_A, C_Y, and C_N represent the axial force, side force, and normal force coefficients, respectively, for each parachute, and are used to compute the aerodynamic forces in the parachute wind frame as shown in Equations (6.3.3-5):

$$(\underline{\mathbf{A}}_1)_{P1} = q_{o\,1}\ S_{\mathrm{Ref}\,1} \begin{Bmatrix} -C_{A1} \\ C_{Y1} \\ -C_{N1} \end{Bmatrix} \tag{6.3.3-5a}$$

$$(\underline{\mathbf{A}}_2)_{P2} = q_{o\,2}\ S_{\mathrm{Ref}\,2} \begin{Bmatrix} -C_{A2} \\ C_{Y2} \\ -C_{N2} \end{Bmatrix} \tag{6.3.3-5b}$$

The notation $(\ )_{\mathrm{P1}}$, $(\ )_{\mathrm{P2}}$ indicates that the aerodynamic force shown in Equations (6.3.3-5) is in the wind frame of parachute 1 or 2. The terms $q_{o\,1}\ S_{\mathrm{Ref}\,1}$ and $q_{o\,2}\ S_{\mathrm{Ref}\,2}$ in Equations (6.3.3-5) represent the product of the dynamic pressure (pounds per square foot (psf)) and aerodynamic reference area (square feet (ft^2)) of parachutes 1 and 2, respectively, and convert the nondimensional aerodynamic coefficients into physical aerodynamic forces (pounds force (lbf)) exerted on the parachutes. As described earlier, the parachutes are assumed to be point masses, or particles, subject only to forces applied that result in 3-DOF translational motion. Therefore, no aerodynamic moments are considered for the parachutes in this analysis.

Once the aerodynamic forces of each parachute have been computed in their respective wind reference frames, as defined in Equations (6.3.3-5), those aerodynamic forces are transformed to the NED frame before combining with the other forces applied to the parachutes (also represented in the NED frame). Newton's second law of motion is applied to compute the parachute translational accelerations and velocities. Later in this section, the mathematical steps necessary for computing the orientation of each parachute's wind reference-frame axes are presented. Steps are presented for computing the DCM and/or quaternion that defines the orientation of the parachute wind reference frames relative to the NED frame that allows a transformation of the parachute's aerodynamic forces to the NED frame.

Once the aerodynamic forces applied to each parachute have been transformed to the NED frame, they can be combined with the riser line forces and the weight of each parachute to apply Newton's law since the NED frame is assumed to be an inertial reference frame. The translational dynamics equations for each parachute in the NED frame are shown in Equations (6.3.3-6):

$$(\underline{\mathbf{a}}_1)_{NED} = \frac{\sum \underline{\mathbf{F}}_{1\,NED}}{m_1} = \frac{\left(\underline{\mathbf{A}}_1 - T_1\,\underline{\hat{\mathbf{n}}}_1\right)_{NED}}{m_1} + \underline{\mathbf{g}}_{NED} \qquad (6.3.3\text{-}6a)$$

$$(\underline{\mathbf{a}}_2)_{NED} = \frac{\sum \underline{\mathbf{F}}_{2\,NED}}{m_2} = \frac{\left(\underline{\mathbf{A}}_2 - T_2\,\underline{\hat{\mathbf{n}}}_2\right)_{NED}}{m_2} + \underline{\mathbf{g}}_{NED} \qquad (6.3.3\text{-}6b)$$

The term $\underline{\mathbf{g}}_{NED}$ in Equations (6.3.3-6) represents the gravity vector at the surface of the Earth with components (0 0 g_0) since gravity is assumed to be directed in the down direction, or along the | z-axis of the NED frame. The negative sign on the riser line force applied to each parachute is needed because the direction of the unit vectors $\underline{\hat{\mathbf{n}}}_1$ and $\underline{\hat{\mathbf{n}}}_2$ is directed from the capsule parachute attach point to each parachute, and so the force exerted on each parachute is equal in magnitude and opposite in direction per application of Newton's third law. Once the acceleration of each parachute in the NED frame has been computed, that acceleration can be integrated to compute the velocity of each parachute relative to the NED frame. This velocity can then be integrated again to compute the translation of each parachute relative to the NED frame. Summarizing, the following equations of motion are provided for each parachute's translational DOF, as shown in Equations (6.3.3-7):

$$\frac{d}{dt}(\underline{\mathbf{V}}_1)_{NED} = (\underline{\mathbf{a}}_1)_{NED} \rightarrow (\underline{\mathbf{V}}_1)_{NED} = \int (\underline{\mathbf{a}}_1)_{NED}\,dt \qquad (6.3.3\text{-}7a)$$

$$\frac{d}{dt}(\underline{\mathbf{R}}_1)_{NED} = (\underline{\mathbf{V}}_1)_{NED} \rightarrow (\underline{\mathbf{R}}_1)_{NED} = \int (\underline{\mathbf{V}}_1)_{NED}\,dt \qquad (6.3.3\text{-}7b)$$

$$\frac{d}{dt}(\underline{\mathbf{V}}_2)_{NED} = (\underline{\mathbf{a}}_2)_{NED} \rightarrow (\underline{\mathbf{V}}_2)_{NED} = \int (\underline{\mathbf{a}}_2)_{NED}\,dt \qquad (6.3.3\text{-}7c)$$

$$\frac{d}{dt}(\underline{\mathbf{R}}_2)_{NED} = (\underline{\mathbf{V}}_2)_{NED} \rightarrow (\underline{\mathbf{R}}_2)_{NED} = \int (\underline{\mathbf{V}}_2)_{NED}\,dt \qquad (6.3.3\text{-}7d)$$

As described earlier, the definition of the parachute wind reference frame places its x-axis along the riser lines connecting each parachute to the capsule attach point and pointed toward the capsule attach point. The z-axis is defined so that it and the x-axis are contained in a plane that contains the x-axis and the instantaneous air relative velocity vector (i.e., the velocity of the parachute relative to local wind ($\underline{\mathbf{V}}_{\text{rel}} = \underline{\mathbf{V}}_{\text{ground relative}} - \underline{\mathbf{V}}_{\text{wind}}$)). Finally, the y-axis is defined such that it completes a right-handed frame.

Equations (6.3.3-4) define unit vectors that point from the capsule parachute attach point to each parachute's wind frame origin. If the vectors used in those calculations are measured in the NED frame, then $\hat{\mathbf{n}}_1$ and $\hat{\mathbf{n}}_2$ unit vectors define unit vectors that point from the capsule attach point to each parachute in the NED frame. This is so that, per the definition of the x-axis described in the preceding paragraph, the x-axis unit vectors of each parachute's wind reference frame are represented by the unit vectors $-\hat{\mathbf{n}}_1$ and $-\hat{\mathbf{n}}_2$.

Because the y-axis of each parachute's wind reference frame is defined to be perpendicular to the plane containing its x-axis and the air relative velocity vector, the unit vector for the y-axis can be computed using a cross-product operation as $\hat{\mathbf{j}} = (\hat{\mathbf{i}} \times \mathbf{V}_{\text{rel}})/|\hat{\mathbf{i}} \times \mathbf{V}_{\text{rel}}|$, where $\hat{\mathbf{i}}$ and $\hat{\mathbf{j}}$

represent the unit vectors for the x-axis and the y-axis of the parachute wind reference frame; $\mathbf{V}_{\text{rel}}$ is the air relative velocity vector, with all defined relative to the NED frame; × represents the vector cross-product operator; and the vertical bars (| |) indicate the magnitude of a vector quantity.

The cross product $\hat{\mathbf{i}} \times \mathbf{V}_{\text{rel}}$ is defined as the magnitude of unit vector $\hat{\mathbf{i}}$ times the magnitude of $\mathbf{V}_{\text{rel}}$ times the sine of the angle between them, and its direction is in a right-hand rule sense of crossing the $\hat{\mathbf{i}}$ unit vector with the $\mathbf{V}_{\text{rel}}$ vector. The sine of the angle between the $\hat{\mathbf{i}}$ unit vector and $\mathbf{V}_{\text{rel}}$ is the sine of the total angle of attack of each parachute. To define polarity of the angle of attack consistent with typical aerospace applications (e.g., positive sideslip angle produces aerodynamic force in the positive y-axis direction, and positive angle of attack produces aerodynamic force in the negative z-axis direction), the cross product $(-\hat{\mathbf{i}}) \times \mathbf{V}_{\text{rel}}$ will define the proper direction of the y-axis unit vector $\hat{\mathbf{j}}$ of the parachute wind frame. Once the x-axis and y-axis unit vectors of each parachute's wind frame are known, then the z-axis unit vector $\hat{\mathbf{k}}$ can be computed as $\hat{\mathbf{k}} = \hat{\mathbf{i}} \times \hat{\mathbf{j}}$ to define a right-hand reference frame. The following equations describe this approach:

$$\left(\underline{\hat{\mathbf{i}}}_{P1}\right)_{NED} = \frac{-\left(\underline{\mathbf{r}}_{P1/AP}\right)_{NED}}{\left|-\left(\underline{\mathbf{r}}_{P1/AP}\right)_{NED}\right|} = -\left(\underline{\hat{\mathbf{n}}}_{1}\right)_{NED} \tag{6.3.3-8a}$$

$$\left(\underline{\hat{\mathbf{j}}}_{P1}\right)_{NED} = \frac{-\left(\underline{\hat{\mathbf{i}}}_{P1}\right)_{NED} \times \left(\underline{\mathbf{V}}_{P1\,\text{rel}}\right)_{NED}}{\left|-\left(\underline{\hat{\mathbf{i}}}_{P1}\right)_{NED} \times \left(\underline{\mathbf{V}}_{P1\,\text{rel}}\right)_{NED}\right|} \tag{6.3.3-8b}$$

$$\left(\underline{\hat{\mathbf{k}}}_{P1}\right)_{NED} = \left(\underline{\hat{\mathbf{i}}}_{P1} \times \underline{\hat{\mathbf{j}}}_{P1}\right) \tag{6.3.3-8c}$$

$$\left(\underline{\hat{\mathbf{i}}}_{P2}\right)_{NED} = \frac{-\left(\underline{\mathbf{r}}_{P2/AP}\right)_{NED}}{\left|-\left(\underline{\mathbf{r}}_{P2/AP}\right)_{NED}\right|} = -\left(\underline{\hat{\mathbf{n}}}_{2}\right)_{NED} \tag{6.3.3-8d}$$

$$\left(\underline{\hat{\mathbf{j}}}_{P2}\right)_{NED} = \frac{-\left(\underline{\hat{\mathbf{i}}}_{P2}\right)_{NED} \times \left(\underline{\mathbf{V}}_{P2\,\text{rel}}\right)_{NED}}{\left|-\left(\underline{\hat{\mathbf{i}}}_{P2}\right)_{NED}\right| \times \left(\underline{\mathbf{V}}_{P2\,\text{rel}}\right)_{NED}} \tag{6.3.3-8e}$$

$$\left(\underline{\hat{\mathbf{k}}}_{P2}\right)_{NED} = \left(\underline{\hat{\mathbf{i}}}_{P2} \times \underline{\hat{\mathbf{i}}}_{P2}\right) \tag{6.3.3-8f}$$

Once the unit vectors of each parachute's wind reference frame relative to the NED frame are computed as defined by Equations (6.3.3-8), the DCM or quaternion that defines their orientations relative to the NED frame can readily be computed. For example, the DCM for the orientation of the parachute's wind reference frame relative to the NED frame is defined, with its rows equal to the elements of the $\hat{\mathbf{i}}, \hat{\mathbf{j}}$, and $\hat{\mathbf{k}}$ unit vectors of the parachute's body frame, as:

$$\underline{\underline{C}}_{P1/NED} = \begin{Bmatrix} \left(\underline{\hat{\mathbf{i}}}_{P1}\right)_{NED} \\ \left(\underline{\hat{\mathbf{j}}}_{P1}\right)_{NED} \\ \left(\underline{\hat{\mathbf{k}}}_{P1}\right)_{NED} \end{Bmatrix} = \begin{bmatrix} \left(\underline{\hat{\mathbf{i}}}_{P1}\right)_{NED_x} & \left(\underline{\hat{\mathbf{i}}}_{P1}\right)_{NED_y} & \left(\underline{\hat{\mathbf{i}}}_{P1}\right)_{NED_z} \\ \left(\underline{\hat{\mathbf{j}}}_{P1}\right)_{NED_x} & \left(\underline{\hat{\mathbf{j}}}_{P1}\right)_{NED_y} & \left(\underline{\hat{\mathbf{j}}}_{P1}\right)_{NED_z} \\ \left(\underline{\hat{\mathbf{k}}}_{P1}\right)_{NED_x} & \left(\underline{\hat{\mathbf{k}}}_{P1}\right)_{NED_y} & \left(\underline{\hat{\mathbf{k}}}_{P1}\right)_{NED_z} \end{bmatrix} \tag{6.3.3-9a}$$

$$\underline{\underline{C}}_{P2/NED} = \begin{Bmatrix} (\hat{\underline{\mathbf{i}}}_{P2})_{NED} \\ (\hat{\underline{\mathbf{j}}}_{P2})_{NED} \\ (\hat{\underline{\mathbf{k}}}_{P2})_{NED} \end{Bmatrix} = \begin{bmatrix} (\hat{\underline{\mathbf{i}}}_{P2})_{NED_x} & (\hat{\underline{\mathbf{i}}}_{P2})_{NED_y} & (\hat{\underline{\mathbf{i}}}_{P2})_{NED_z} \\ (\hat{\underline{\mathbf{j}}}_{P2})_{NED_x} & (\hat{\underline{\mathbf{j}}}_{P2})_{NED_y} & (\hat{\underline{\mathbf{j}}}_{P2})_{NED_z} \\ (\hat{\underline{\mathbf{k}}}_{P2})_{NED_x} & (\hat{\underline{\mathbf{k}}}_{P2})_{NED_y} & (\hat{\underline{\mathbf{k}}}_{P2})_{NED_z} \end{bmatrix} \tag{6.3.3-9b}$$

Once the orientation of each parachute's wind frame is defined with a DCM as shown in Equations (6.3.3-9) or equivalently with a quaternion, the aerodynamic forces applied to each parachute can be transformed from body frame to NED.

6.3.3.4 Derivation of Capsule Equations of Motion

For the purposes of this analysis, it is assumed the aerodynamic forces and moments exerted on the capsule ($\underline{\mathbf{A}}_C$ and $\underline{\mathbf{M}}_C$, as shown in Figure 6.3.3.3-1), are specified in its body frame as described in Section 6.3.3.2. Typical aerodynamic conventions are used, with axial force applied opposite the x-axis, normal force applied opposite the z-axis, and side force applied in the direction of the y-axis. The aerodynamic moments are defined relative to the capsule's aerodynamic reference center (ARC), which is an arbitrary location chosen by the developers of the aerodynamic model. The location of the ARC is specified in the capsule's structural reference frame, as defined in Section 6.3.3.2. As a result, aerodynamic moments exerted on the capsule must be transferred from the ARC to its CM before applying Euler's law for the capsule rotational equations of motion.

The aerodynamic forces applied to the capsule are computed using nondimensional aerodynamic coefficients for axial force, side force, and normal force denoted as C_A, C_Y, and C_N, respectively. By traditional definitions, aerodynamic axial force is directed in the negative x-axis direction of the capsule body frame, aerodynamic side force is directed in the positive y-axis direction, and aerodynamic normal force is directed in the negative z-axis direction. These coefficients generally are defined as functions of Mach number, angle of attack, and sideslip angle, or alternatively for axisymmetric or nearly axisymmetric bodies, as Mach number, total angle of attack, and aerodynamic roll angle. The relationship of the total angle of attack (α_{Total}) and aerodynamic roll angle (ϕ_{Aero}) with angle of attack (α) and sideslip angle (β) are

$$\tan(\phi_{\text{Aero}}) = \frac{\tan(\beta)}{\sin(\alpha)} \tag{6.3.3-10a}$$

$$\cos(\alpha_{\text{Total}}) = \cos(\alpha)\cos(\beta) \tag{6.3.3-10b}$$

Once the aerodynamic angles (α and β) or (α_{Total} and ϕ_{Aero}) and the aerodynamic force coefficients have been computed, the capsule aerodynamic forces in its body reference frame can be computed as

$$(\underline{\mathbf{A}}_C)_b = q_{o\,C}\, S_{\text{Ref}\,C} \begin{Bmatrix} -C_{AC} \\ C_{YC} \\ -C_{NC} \end{Bmatrix} \tag{6.3.3-11}$$

The term "$q_{o\,C}\, S_{\text{Ref}\,C}$" in Equation (6.3.3-11) represents the product of the capsule dynamic pressure, $q_{o\,C}$ (psf), and its aerodynamic reference area, $S_{\text{Ref}\,C}$ (ft^2), and converts the nondimensional aerodynamic coefficients into physical aerodynamic forces (lbf) exerted on the capsule. The subscript b for the capsule aerodynamic force $\underline{\mathbf{A}}_C$ indicates that it is resolved in its body axis frame.

As was the case with the parachute equations of motion, the aerodynamic forces applied to the capsule can be transformed from the body frame to the NED frame for application of Newton's second law.

In a similar manner, the aerodynamic moments applied to the capsule are computed using nondimensional aerodynamic coefficients for roll axis, pitch axis, and yaw axis denoted as C_ℓ, C_m, and C_n, respectively. By traditional definitions, aerodynamic moment coefficients are defined to produce positive right-hand rule moments about the body frame x-, y-, and z-axes. These coefficients generally are defined as functions of Mach number, angle of attack, and sideslip angle, or alternatively for axisymmetric or nearly axisymmetric bodies, as Mach number, total angle of attack, and aerodynamic roll angle. The aerodynamic angles were defined previously, with Equations (6.3.3-10) showing the relationship between them. Once the aerodynamic angles (α and β) or (α_{Total} and ϕ_{Aero}) and the aerodynamic moment coefficients have been computed, the aerodynamic moments about the capsule aerodynamic reference center can be computed as

$$(\underline{\mathbf{M}}_{C\,ARC})_b \;=\; q_{o\,C}\, \mathrm{S}_{\mathrm{Ref\,C}}\, \ell_{\mathrm{Ref}\,C} \begin{Bmatrix} C_\ell \\ C_m \\ C_n \end{Bmatrix} \qquad (6.3.3\text{-}12)$$

The term "$q_{o\,C}\, \mathrm{S}_{\mathrm{Ref\,C}}\, \ell_{\mathrm{Ref}\,C}$" in Equation (6.3.3-12) represents the product of the capsule dynamic pressure, $q_{\mathrm{o}\,C}$ (psf), with its aerodynamic reference area, $S_{\mathrm{Ref}\,C}$ (ft^2), and its aerodynamic reference length, $\ell_{\mathrm{Ref}\,C}$ (ft), to convert the nondimensional aerodynamic moment coefficients into physical aerodynamic moments (ft-lbf) exerted on the capsule at the aerodynamic reference center. The subscript b for the capsule aerodynamic moments, $(\underline{\mathbf{M}}_{\mathrm{C\,ARC}})_b$, in Equation (6.3.3-12), indicates that it is resolved in the capsule body axis frame. The subscript "$_{\mathrm{C\,ARC}}$" indicates that the moment computed as in Equation (6.3.3-12) is about the capsule's aerodynamic reference center and must be transferred to the crew module capsule CM before use in the rotational equation of motion.

In addition to the static or steady-state aerodynamic moments exerted on the capsule, there are also moments exerted due to aerodynamic damping caused by the angular velocity of the crew module and/or the rate of change of angle of attack and sideslip angle. The aerodynamic damping moments are computed from nondimensional aerodynamic damping coefficients $C_{\ell\mathrm{p}}$, C_{mq}, C_{nr}, , $C_{m\,\dot{\alpha}}$, and $C_{\mathrm{n}\,\dot{\beta}}$. The aerodynamic damping derivative coefficients are converted to physical moments exerted on the capsule as

$$\left(\underline{\mathbf{M}}_{C\,\mathrm{damping}}\right)_b = q_{o\,C}\; S_{\mathrm{Ref}\,C}\; \ell_{\mathrm{Ref}\,C}\; \frac{\ell_{\mathrm{Ref}\,C}}{2V_{Rel}\,C} \begin{Bmatrix} C_{\ell p}\, p \\ C_{mq}\, q \;+\; C_{m\dot{\alpha}}\, \dot{\alpha} \\ C_{nr}\, r \;+\; C_{n\dot{\beta}}\, \dot{\beta} \end{Bmatrix} \qquad (6.3.3\text{-}13)$$

The transfer of the aerodynamic moments from the capsule's ARC to its CM can be accomplished by computing the additional aerodynamic moment on the capsule about its CM, due to the aerodynamic forces applied at the ARC by computing the vector cross product of the vector from the capsule CM to its ARC and its aerodynamic force vector as

$$\left(\Delta\underline{\mathbf{M}}_{C}\right)_{b} = \left(\underline{\mathbf{r}}_{ARC/C}\right)_{b} \times \left(\underline{\mathbf{A}}_{C}\right)_{b} \tag{6.3.3-14a}$$

$$\left(\underline{\mathbf{r}}_{ARC/C}\right)_{b} = \begin{Bmatrix} -(x_{ARC} - x_{C})_{S} \\ (y_{ARC} - y_{C})_{S} \\ -(z_{ARC} - z_{C})_{S} \end{Bmatrix} \tag{6.3.3-14b}$$

where $x_{ARC}, y_{ARC}, z_{ARC}$, are the locations of the ARC and x_{C}, y_{C}, z_{C} are the locations of the capsule CM, each in the capsule structural reference frame (denoted by the subscript *s*). The negative signs on the x-axis and z-axis differences are used to transform from capsule structural frame to capsule body frame because the x-axis and z-axis directions are reversed for the capsule structural reference frame and the capsule body reference frame.

The total aerodynamic moment exerted on the capsule about its CM in the capsule body reference frame is the sum of the static aerodynamic moment relative to the aerodynamic moment reference center $(\underline{\mathbf{M}}_{C\,ARC})_b$ in Equation (6.3.3-12), the incremental moment of the aerodynamic forces about the capsule CM $(\Delta\underline{\mathbf{M}}_{C})_b$ in Equation (6.3.3-14a), and the aerodynamic damping moment $\left(\underline{\mathbf{M}}_{C\,\text{damping}}\right)_{b}$ in Equation (6.3.3-13):

$$\left(\underline{\mathbf{M}}_{C}\right)_{b} = \left(\underline{\mathbf{M}}_{C\,ARC}\right)_{b} + \left(\Delta\underline{\mathbf{M}}_{C}\right)_{b} + \left(\underline{\mathbf{M}}_{C\,\text{damping}}\right)_{b} \tag{6.3.3-15}$$

Once the aerodynamic forces applied to the capsule have been computed and transformed to the NED frame as described in the previous section, they can be combined with the riser line forces from each parachute and with the capsule weight to apply Newton's second law of motion since the NED frame is assumed to be an inertial reference frame. The translational equation of motion for the capsule in the NED frame are

$$\left(\underline{\mathbf{a}}_{C}\right)_{NED} = \frac{\sum \underline{\mathbf{F}}_{C\,NED}}{m_{C}} = \frac{\left(\underline{\mathbf{A}}_{C} + T_{1}\,\underline{\hat{\mathbf{n}}}_{1} + T_{2}\,\underline{\hat{\mathbf{n}}}_{2}\right)_{NED}}{m_{c}} + \underline{\mathbf{g}}_{NED} \tag{6.3.3-16}$$

As before, the term $\underline{\mathbf{g}}_{NED}$ in Equation (6.3.3-16) represents the gravity vector at the surface of the Earth with NED frame components (0 0 g_o) since gravity is assumed to be directed in the down direction, or along the z-axis of the NED frame. The terms T_1 and T_2 and $\underline{\hat{\mathbf{n}}}_1$ and $\underline{\hat{\mathbf{n}}}_2$ were defined previously as the forces applied to the capsule by each parachute's riser lines and the unit vector from the capsule parachute attach point to each parachute, respectively. Once the acceleration of the capsule in the NED frame is computed, it can be integrated to compute the velocity of the capsule CM relative to the NED frame, and then that velocity can be integrated again to compute the translation of the crew module CM relative to the NED frame. Summarizing, the following integrations are performed for the capsule translational DOFs:

$$\frac{d}{dt}\left(\underline{\mathbf{V}}_{c}\right)_{NED} = (\underline{\mathbf{a}}_{c})_{NED} \quad \rightarrow \quad \left(\underline{\mathbf{V}}_{c}\right)_{NED} = \int (\underline{\mathbf{a}}_{c})_{NED}\,dt \tag{6.3.3-17a}$$

$$\frac{d}{dt}\left(\underline{\mathbf{R}}_{c}\right)_{NED} = (\underline{\mathbf{V}}_{c})_{NED} \quad \rightarrow \quad \left(\underline{\mathbf{R}}_{c}\right)_{NED} = \int (\underline{\mathbf{V}}_{c})_{NED}\,dt \tag{6.3.3-17b}$$

Once the aerodynamic forces applied to the capsule are computed as defined in the previous section, the capsule rotational dynamics can be computed from the application of Euler's law of motion for rotational angular momentum of the capsule. This indicates the change in angular momentum of an object relative to an inertial frame of reference is equal to the sum of the moments applied to that body.

If $\underline{\mathbf{I}}_C$ is the moment of inertia tensor (or dyadic) of the body and $\underline{\boldsymbol{\omega}}_c$ is the angular rate of that body relative to some inertial frame of reference, then the angular momentum of that body $\underline{\mathbf{H}}_C$ is defined as $\underline{\mathbf{H}}_C = \underline{\mathbf{I}}_C\, \underline{\boldsymbol{\omega}}_c$. Further, application of Euler's law of rotational motion can be used to compute the time derivative of the angular momentum as

$$\frac{d}{dt}\left(\underline{\mathbf{H}}_C\right)_{NED} = \frac{d}{dt}\left(\underline{\underline{\mathbf{I}}}_C \cdot \underline{\boldsymbol{\omega}}_C\right)_{NED} = \frac{d}{dt}\left(\underline{\underline{\mathbf{I}}}_C\right)_b \cdot \underline{\boldsymbol{\omega}}_C + \underline{\underline{\mathbf{I}}}_C \cdot \frac{d}{dt}\left(\underline{\boldsymbol{\omega}}_C\right)_b + \underline{\boldsymbol{\omega}}_C \times \left(\underline{\underline{\mathbf{I}}}_C \cdot \underline{\boldsymbol{\omega}}_C\right) = \Sigma\left(\underline{\mathbf{M}}\right)_b \tag{6.3.3-18}$$

The cross-product term shown in Equation (6.3.3-18) is required because the reference frame used for the calculations is the capsule body frame, which is rotating with an angular velocity of $\underline{\boldsymbol{\omega}}$ relative to the inertial NED frame (although the components of $\underline{\boldsymbol{\omega}}$ are expressed in the rotating capsule body frame *b*). Assuming the capsule moment of inertia tensor (or dyadic) is constant, Equation (6.3.3-18) can be rearranged to compute the time rate of change of the angular velocity of the capsule body reference frame axes relative to the inertial NED frame in the capsule body frame as

$$\frac{d}{dt}\left(\underline{\boldsymbol{\omega}}_C\right)_b = \underline{\underline{\mathbf{I}}}_C^{-1}\left\{\Sigma\left(\underline{\mathbf{M}}\right)_b - \left(\underline{\boldsymbol{\omega}}_C\right)_b \times \left(\underline{\underline{\mathbf{I}}}_C \cdot \left(\underline{\boldsymbol{\omega}}_C\right)_b\right)\right\} \tag{6.3.3-19}$$

The sum of the moments applied to the capsule CM in its body reference frame $\Sigma(\underline{\mathbf{M}})_b$ consists of the aerodynamic moment as defined in Equations (6.3.3-12) through (6.3.3-15), and the moment about the capsule CM due to each parachute's riser line force applied to the attach point on the capsule, which is offset from its CM. The moments exerted about the capsule CM from the parachute riser lines in its capsule body frame are defined as

$$\left(\underline{\mathbf{M}}_{P1\,C}\right)_b = \left(\underline{\mathbf{r}}_{AP/C}\right)_b \times T_1\left(\underline{\hat{\mathbf{n}}}_1\right)_b \tag{6.3.3-20a}$$

$$\left(\underline{\mathbf{r}}_{AP/C}\right)_b = \begin{Bmatrix} -(x_{AP} - x_C)_S \\ (y_{AP} - y_C)_S \\ -(z_{AP} - z_C)_S \end{Bmatrix} \tag{6.3.3-20b}$$

$$\left(\underline{\mathbf{M}}_{P2\,C}\right)_b = \left(\underline{\mathbf{r}}_{AP/C}\right)_b \times T_2\left(\underline{\hat{\mathbf{n}}}_2\right)_b \tag{6.3.3-20c}$$

As with the aerodynamic moment calculation, the vector from the capsule CM to its parachute attach point $(\underline{\mathbf{r}}_{AP/C})_b$ in Equations (6.3.3-20) is defined relative to the locations in the capsule structural reference frame and transformed to its body frame by negating the x- and z-axis components. The force applied by each parachute's riser line is the product of a scalar force magnitude, T_1 or T_2, and a unit vector in capsule frame, denoted by $(\underline{\hat{\mathbf{n}}}_1)_b$ or $(\underline{\hat{\mathbf{n}}}_2)_b$ in Equations (6.3.3-20a) and (6.3.3-20c) and defined in Equation (6.3.3-4). In summary, the sum of moments about the capsule CM is

$$\Sigma\left(\underline{\mathbf{M}}\right)_b = \left(\underline{\mathbf{M}}_C\right)_b + \left(\underline{\mathbf{M}}_{P1\,C}\right)_b + \left(\underline{\mathbf{M}}_{P2\,C}\right)_b \tag{6.3.3-21}$$

Equation of motion (6.3.3-19) provides capsule-body-frame components of the angular acceleration of the capsule relative to the inertial NED frame. Capsule-body-frame components of the angular velocity of the capsule relative to the NED frame are obtained by integration:

$$\left(\underline{\boldsymbol{\omega}}_c\right)_b = \int \left(\dot{\underline{\boldsymbol{\omega}}}_C\right)_b \, dt \qquad (6.3.3\text{-}22)$$

6.3.4 Analytic Check Cases for Simulation Verification

This section presents an overview of a series of analytical check cases developed for the purpose of verification of the new flight simulation tool, CAPDYN. The individual verification cases are identified in Table 6.3.4-1. Cases 1 through 5 were designed to isolate and verify limited aspects of the numerical solution of the equations of motion in CAPDYN by reducing the configuration to its simplest form and simplifying the motion characteristics to their basic components. The CAPDYN results were verified for cases 1 through 5 by comparing the predicted motion with the analytical solution and with results from FAST (i.e., the Flight Analysis and Simulation Tool) in three of the five cases. Cases 6 through 10 describe more complex motion, where a comparison of results from CAPDYN and FAST was used to assess verification of CAPDYN. The details of the derivation and development of each case, as well as the verification results from CAPDYN and FAST, are included in the appendices (see Volume II).

Table 6.3.4-1. Table of Contents of Analytical Verification Cases

		Development	**Verification**
Case #	**Title**	**Appendix**	**Simulations**
1	Constant Density Descent	A	CAPDYN and FAST
2	Exponential Density Descent	B	CAPDYN and FAST
3	Vertical Wind Shear, Constant Density	C	CAPDYN
4	Steady State Glide	D	CAPDYN and FAST
5	Horizontal Wind Shear, Constant Density	E	CAPDYN
6	Pendulum Motion	F	CAPDYN and FAST
7	Damped Pendulum Motion	G	CAPDYN and FAST
8	Maypole Motion	H	CAPDYN and FAST
9	Nonplanar Pendulum Motion	I	CAPDYN and FAST
10	Nonplanar Flyout Motion	J	CAPDYN and FAST

FAST is a multi-body, variable-DOF simulation developed for the study of atmospheric and powered flight. It has been used extensively by the CPAS project for pretest analysis and post-test reconstruction, including modeling two-parachute cluster pendulum dynamics.

6.3.5 Nonlinear Aerodynamic Modeling from Flight Data using Equation Error

The equation-error method is applied most commonly to calculate aerodynamic model parameter estimates that minimize the sum of squared differences between values of nondimensional force and moment coefficients determined from measured flight data and corresponding values computed using the model. A separate modeling problem can be solved for each force or moment coefficient, corresponding to minimizing the equation-error in each individual equation of motion for the six rigid-body DOF. Nondimensional force coefficients are computed from flight data as follows

$$C_A = -C_X = -\frac{1}{\bar{q}S}\left(m\,a_x - T - g_x\right) \tag{6.3.5-1a}$$

$$C_Y = \frac{1}{\bar{q}S}\left(m\,a_y - g_y\right) \tag{6.3.5-1b}$$

$$C_N = -C_Z = -\frac{1}{\bar{q}S}\left(m\,a_z - g_z\right) \tag{6.3.5-1c}$$

where the quantities a_x, a_y, a_z are components of the acceleration vector in parachute body axes, and not the output from accelerometers. The quantities g_x, g_y, g_z are the components of gravitational acceleration in parachute body axes. For parachute aerodynamic modeling, the aerodynamic moments are assumed to be small, so that

$$C_l = C_m = C_n = 0 \tag{6.3.5-2}$$

This results in *N* values of the nondimensional force coefficients, where *N* is the number of data points for the flight data. These values often are called measured nondimensional force and moment coefficients even though they are not measured directly, but rather are computed from other measurements and known quantities using Equations (6.3.5-1).

Analytic parameterized models are postulated for the dependence of the nondimensional aerodynamic force coefficients on a linear combination of model terms assembled from the measured explanatory variables, known as regressors. Note that although the combination of regressors is linear, each regressor can be an arbitrary linear or nonlinear function of the explanatory variables. The unknown parameters in the models are estimated using a least-squares optimization criterion. Using the C_N modeling as an example, a selected model structure might include four regressors, as follows:

$$C_N = C_{N_1}\xi_1 + C_{N_2}\xi_2 + C_{N_3}\xi_3 + C_{N_4}\xi_4 \tag{6.3.5-3}$$

where $C_{N_1}, C_{N_2}, C_{N_3}, C_{N_4}$ are unknown model parameters and $\xi_1, \xi_2, \xi_3, \xi_4$ are regressors computed from measured explanatory variable data (e.g., total angle of attack and airspeed data). Substituting force coefficient values computed from Equation (6.3.5-1c) on the left, with regressor values computed from the measured explanatory variable data on the right, results in an over-determined set of equations for the unknown aerodynamic model parameters $C_{N_1}, C_{N_2}, C_{N_3}, C_{N_4}$. This problem can be solved using a standard least-squares method applied to Equation (6.3.5-3) and other similar model equations for the other nondimensional aerodynamic force coefficients, individually. Determining which particular regressors (model terms) should be included in models such as the example shown in Equation (6.3.5-3) is called model structure determination, which is discussed in Section 6.3.6.

For example, the least-squares problem for the normal force coefficient C_N is formulated using the model structure in Equation (6.3.5-3) as

$$\boldsymbol{z} = \boldsymbol{X\theta} + \boldsymbol{\varepsilon} \tag{6.3.5-4}$$

where

$\boldsymbol{z} = \left[C_N(1) \quad C_N(2) \quad \ldots \quad C_N(N) \right]^T = N \times 1$ vector of values computed from flight data

$\boldsymbol{\theta} = \left[C_{N_1} \quad C_{N_2} \quad C_{N_3} \quad C_{N_4} \right]^T = 4 \times 1$ vector of unknown parameters

$\boldsymbol{X} = [\xi_1 \quad \xi_2 \quad \xi_3 \quad \xi_4] = N \times 4$ matrix of explanatory data vectors or regressors

$\boldsymbol{\varepsilon} = \left[\varepsilon(1) \quad \varepsilon(2) \quad \ldots \quad \varepsilon(N) \right]^T = N \times 1$ vector of equation errors

The matrix $\boldsymbol{X}$ is assembled using flight data, with each column representing a regressor (modeling function). The best estimate of the unknown model parameters $\boldsymbol{\theta}$ in a least-squares sense comes from minimizing the sum of squared differences between the dependent variable measurements $\boldsymbol{z}$ and the model output:

$$J(\boldsymbol{\theta}) = \frac{1}{2}(\boldsymbol{z} - \boldsymbol{X\theta})^T (\boldsymbol{z} - \boldsymbol{X\theta}) \tag{6.3.5-5}$$

The least-squares solution for the unknown parameter vector $\boldsymbol{\theta}$ is [ref. 15]

$$\hat{\boldsymbol{\theta}} = \left(\boldsymbol{X}^T \boldsymbol{X} \right)^{-1} \boldsymbol{X}^T \boldsymbol{z} \tag{6.3.5-6}$$

and the estimated parameter covariance matrix is computed from

$$Cov\left(\hat{\boldsymbol{\theta}}\right) = \hat{\sigma}^2 \left(\boldsymbol{X}^T \boldsymbol{X} \right)^{-1} \tag{6.3.5-7}$$

The model output is

$$\hat{\boldsymbol{y}} = \boldsymbol{X}\hat{\boldsymbol{\theta}} \tag{6.3.5-8}$$

and the model fit-error variance estimate is

$$\hat{\sigma}^2 = \frac{(\boldsymbol{z} - \hat{\boldsymbol{y}})^T (\boldsymbol{z} - \hat{\boldsymbol{y}})}{\left(N - n_p\right)} \tag{6.3.5-9}$$

where the number of unknown parameters is $n_p = 4$ for this example. The standard errors of the estimated parameters are given by the square root of the diagonal elements of the covariance matrix

$$s\left(\hat{\theta}_j\right) = \sqrt{C_{jj}} \qquad j = 1, 2, \ldots, n_p \tag{6.3.5-10}$$

The vector of equation-error residuals is computed from

$$\hat{\boldsymbol{\varepsilon}} = \boldsymbol{z} - \hat{\boldsymbol{y}} \tag{6.3.5-11}$$

The equations above show that the equation-error method for parameter estimation has a relatively simple, non-iterative solution, based on linear algebra. The modeling can be done using Equation (6.3.5-3) (or analogous versions of these equations for the other DOF, with different model terms), one at a time. The equation-error method can be considered a method wherein the model matches nondimensional aerodynamic coefficients rather than the measured outputs, as in the output-error method described later. This can be seen in Equations (6.3.5-1) and (6.3.5-3), where the dependent variable data in the equation-error method are nondimensional aerodynamic coefficient data computed from measured flight data. Consequently, a model that uses equation-error parameter estimates will not produce the best match to the measured responses of the dynamic system (such as total angle of attack or airspeed), because that is not what is being optimized. On the other hand, there is no need to integrate equations of motion to get model outputs when using the equation-error method, because the matching is done in the equations of motion directly, hence, the name "equation-error." One important practical consequence is that the equation-error method can be applied equally well to data from inherently stable or unstable dynamic systems. Another important consequence is that the model structure can be efficiently determined using equation-error because the equation-error problem has a rapid, one-shot linear algebra solution, whereas output-error requires an iterative nonlinear optimization involving integration of the equations of motion. The equation-error method is implemented in the System IDentification Programs for AirCraft or SIDPAC [refs. 15 and 21], program `lesq.m`, and this tool was applied to the flight data.

In theory, the model residuals $\hat{\boldsymbol{\varepsilon}} = \boldsymbol{z} - \hat{\boldsymbol{y}}$ are assumed to be white noise with no deterministic character. However, because of small aerodynamic model structure errors and unmodeled effects (e.g., aeroelasticity and unsteady aerodynamics), most practical applications of aerodynamic modeling produce residuals that resemble colored noise with dominant low-frequency content. Colored noise is time-correlated with non-uniform variance as a function of frequency, whereas white noise has no time correlation and constant variance as a function of frequency. This mismatch between theory and practice adversely impacts the computed uncertainties for the model parameter estimates.

A method that corrects for colored residuals to produce accurate parameter uncertainties is described in references 15 and 16. This method accounts for colored residuals by modifying the calculation of the covariance matrix in Equations (6.3.5-7) and (6.3.5-9) with an improved estimate of the residual variance and time correlations. The correction is implemented in SIDPAC program `r_colores.m`, which was used to compute equation-error model parameter uncertainties.

Two important indicators of the suitability of the flight data for modeling purposes are signal-to-noise ratio (SNR) of the measured outputs to be modeled (nondimensional aerodynamic force coefficient data in this case), and correlations among the regressors. Measured output SNR can be computed independently from the modeling process using a global optimal Fourier smoothing technique[15] to separate deterministic signal from random noise. This technique is implemented in the SIDPAC program `smoo.m`. Pairwise correlations for the regressors are quantified by the correlation coefficients, which can be computed using SIDPAC program `regcor.m`. Each correlation coefficient is an inner product of two data vectors scaled to unit length with their mean values removed. The simple pairwise correlation between regressors $\boldsymbol{\xi}_j$ and $\boldsymbol{\xi}_k$ is given by

$$r_{jk} = \frac{S_{jk}}{\sqrt{S_{jj} S_{kk}}} \qquad (6.3.5\text{-}12)$$

where

$$S_{jk} = \sum_{i=1}^{N} \left[\xi_j(i) - \bar{\xi}_j \right] \left[\xi_k(i) - \bar{\xi}_k \right] \tag{6.3.5-13a}$$

$$S_{jj} = \sum_{i=1}^{N} \left[\xi_j(i) - \bar{\xi}_j \right]^2 \qquad S_{kk} = \sum_{i=1}^{N} \left[\xi_k(i) - \bar{\xi}_k \right]^2 \tag{6.3.5-13b}$$

$$\bar{\xi}_j = \frac{1}{N} \sum_{i=1}^{N} \xi_j(i) \qquad \bar{\xi}_k = \frac{1}{N} \sum_{i=1}^{N} \xi_k(i) \tag{6.3.5-13c}$$

Similarly, the correlation between a regressor ξ_j and the measured dependent variable z is

$$r_{jz} = \frac{S_{jz}}{\sqrt{S_{jj} S_{zz}}} \tag{6.3.5-14}$$

where

$$\bar{z} = \frac{1}{N} \sum_{i=1}^{N} z(i) \tag{6.3.5-15a}$$

$$S_{jz} = \sum_{i=1}^{N} \left[\xi_j(i) - \bar{\xi}_j \right] \left[z(i) - \bar{z} \right] \qquad S_{zz} = \sum_{i=1}^{N} \left[z(i) - \bar{z} \right]^2 \tag{6.3.5-15b}$$

Correlation coefficients lie in the range $[-1, 1]$. A value of 1 indicates data vectors with identical normalized variations. A value of –1 indicates data vectors with normalized variations that differ only by a minus sign. A value of 0 indicates that the normalized variations are completely uncorrelated, which means the normalized data vectors are orthogonal.

In general, output SNR greater than 3 and pairwise regressor correlations with magnitude less than 0.9 are acceptable. However, acceptable values of these metrics do not guarantee that a good model can be identified from the data. That determination must come from actually identifying models and testing their prediction capability.

6.3.6 Model Structure Determination Using Multivariate Orthogonal Functions

The task of determining which modeling functions should appear on the right sides of Equations (6.3.5-3) through (6.3.5-5) is called model structure determination. One effective method to accomplish this task is called multivariate orthogonal function modeling [refs. 15, 17–19]. The technique begins by generating candidate multivariate functions of the selected explanatory variable data, up to a selected maximum model complexity. Although any function of the explanatory variables could be used, multivariate polynomials and spline functions are preferred because of their similarity to a truncated Taylor series and their easy physical interpretation. These ordinary functions are orthogonalized so that each of the resulting orthogonal functions retains only the explanatory capability that is unique to that modeling function. With this data transformation, it is a straightforward process to select which of the orthogonal modeling functions are most effective in modeling the measured data for the dependent variable, and how many of these orthogonal functions should be included to identify a model that exhibits both a good fit to the modeling data and good prediction capability for other data. The final steps are an error-free transformation from the selected orthogonal modeling functions back to physically meaningful ordinary functions of the explanatory variables, and calculation of the uncertainties for the associated model parameter estimates.

The orthogonalization can be implemented using a standard $\boldsymbol{QR}$ decomposition of the matrix of candidate regressors:

$$\boldsymbol{X} = \boldsymbol{QR} \tag{6.3.6-1}$$

where the columns of $\boldsymbol{X}$ contain the candidate modeling functions, $\boldsymbol{Q}$ is an orthonormal matrix with the same dimensions as $\boldsymbol{X}$, and $\boldsymbol{R}$ is a square upper triangular matrix. Implementations of $\boldsymbol{QR}$ decomposition algorithms are available in many numerical analysis software packages, including MATLAB, which was used for this work. Substituting the decomposition in Equation (6.3.6-1) into Equation (6.3.5-8) yields

$$\boldsymbol{R}^T \boldsymbol{R}\hat{\boldsymbol{\theta}} = \boldsymbol{R}^T \boldsymbol{Q}^T \boldsymbol{z} \tag{6.3.6-2}$$

$$\boldsymbol{R}\hat{\boldsymbol{\theta}} = \boldsymbol{Q}^T \boldsymbol{z} \tag{6.3.6-3}$$

From Equation (6.3.6-3), the elements of $\hat{\boldsymbol{\theta}}$ can be found by simple back substitution, because $\boldsymbol{R}$ is an upper triangular matrix. Rewriting Equation (6.3.6-3) in component form yields

$$\begin{bmatrix} r_{11} & r_{12} & \cdots & r_{1n_c} \\ 0 & r_{22} & \cdots & r_{2n_c} \\ \vdots & & \ddots & \vdots \\ 0 & \dots & 0 & r_{n_c n_c} \end{bmatrix} \begin{bmatrix} \hat{\theta}_1 \\ \hat{\theta}_2 \\ \vdots \\ \hat{\theta}_{n_c} \end{bmatrix} = \begin{bmatrix} \boldsymbol{q}_1^T \boldsymbol{z} \\ \boldsymbol{q}_2^T \boldsymbol{z} \\ \vdots \\ \boldsymbol{q}_{n_c}^T \boldsymbol{z} \end{bmatrix} \tag{6.3.6-4}$$

where $\boldsymbol{q}_j$ is the *j*th column of the matrix $\boldsymbol{Q}$. The right side of Equation (6.3.6-4) is a vector of projections of the dependent variable vector $\boldsymbol{Z}$ onto the orthonormal functions in the columns of $\boldsymbol{Q}$. The absolute values of these quantities indicate the degree of correlation of the orthonormal functions in the columns of $\boldsymbol{Q}$ with $\boldsymbol{Z}$ and, consequently, the effectiveness of each orthonormal function in modeling the dependent variable data. Note that the model parameters $\hat{\theta}_j,\ j = 1, 2, \dots, n_c$, are associated with the original multivariate modeling functions in the columns of $\boldsymbol{X}$ and not with the orthonormal functions in the columns of $\boldsymbol{Q}$.

The form of a multivariate orthonormal function model is

$$\boldsymbol{z} = a_1 \boldsymbol{q}_1 + a_2 \boldsymbol{q}_2 + \dots + a_n \boldsymbol{q}_n + \boldsymbol{\varepsilon} \tag{6.3.6-5}$$

where $\boldsymbol{z}$ is an *N*-dimensional vector of dependent variable data (e.g., nondimensional force coefficient data), $\boldsymbol{z} = \left[z_1, z_2, \dots, z_N\right]^T$, modeled in terms of a linear combination of *n* mutually orthonormal modeling functions $\boldsymbol{q}_j,\ j = 1, 2, \dots, n$. Each $\boldsymbol{q}_j$ is an *N*-dimensional vector that in general depends on the explanatory variables. The $a_j,\ j = 1, 2, \dots, n$, are constant model parameters to be determined, and $\boldsymbol{\varepsilon}$ denotes the model residual vector. Equation (6.3.6-5) represents a mathematical model for the dependent variable $\boldsymbol{z}$ in terms of orthonormal functions generated from the explanatory variable data. The importance of determining which modeling functions should be included in Equation (6.3.6-5), which determines the model structure, is addressed below.

Assembling the n orthonormal modeling functions from Equation (6.3.6-5) in the columns of an $N \times n$ matrix $\boldsymbol{Q}$,

$$\boldsymbol{Q} = [\boldsymbol{q}_1, \boldsymbol{q}_2, \ldots, \boldsymbol{q}_n] \tag{6.3.6-6}$$

and defining the unknown parameter vector $\boldsymbol{a} = [a_1, a_2, \ldots, a_n]^T$, Equation (6.3.6-5) can be written as

$$\boldsymbol{z} = \boldsymbol{Q}\boldsymbol{a} + \boldsymbol{\varepsilon} \tag{6.3.6-7}$$

Equation (6.3.6-7) is the same equation error-model equation discussed earlier, except that the modeling functions are now mutually orthonormal functions. In this case, it is easier to determine an appropriate model structure because the explanatory capability of each modeling function is completely distinct from all the others due to the mutual orthogonality of the columns of $\boldsymbol{Q}$. This decouples the least-squares modeling problem, as shown here.

For mutually orthonormal functions,

$$\boldsymbol{q}_i^T \boldsymbol{q}_j = \begin{cases} 1 & \text{for } i = j \\ 0 & \text{for } i \neq j \end{cases} \qquad i, j = 1, 2, \ldots, n \tag{6.3.6-8}$$

and $\boldsymbol{Q}^T \boldsymbol{Q}$ is the identity matrix. Using Equation (6.3.6-8) in the least-squares solution from Equation (6.3.5-8), the *j*th element of the estimated parameter vector $\hat{\boldsymbol{a}}$ is given by

$$\hat{a}_j = \boldsymbol{q}_j^T \boldsymbol{z} \tag{6.3.6-9}$$

The least-squares cost function using orthonormal functions is then

$$J(\hat{\boldsymbol{a}}) = \frac{1}{2}\left(\boldsymbol{z}^T \boldsymbol{z} - \hat{\boldsymbol{a}}^T \hat{\boldsymbol{a}}\right) = \frac{1}{2}\left[\boldsymbol{z}^T \boldsymbol{z} - \sum_{j=1}^{n} \left(\boldsymbol{q}_j^T \boldsymbol{z}\right)^2\right] \tag{6.3.6-10}$$

Equation (6.3.6-10) shows that when the modeling functions are orthonormal, the reduction in the least-squares cost function resulting from including the term $a_j \boldsymbol{q}_j$ in the model depends only on the dependent variable data $\boldsymbol{z}$ and the added orthonormal modeling function $\boldsymbol{q}_j$. The least-squares modeling problem is therefore decoupled, which means each orthonormal modeling function can be evaluated independently in terms of its ability to reduce the least-squares model fit to the data, regardless of which other orthonormal modeling functions are already selected for the model. If the modeling functions were instead polynomials in the explanatory variables (or any other non-orthogonal function set), then the least-squares problem would be coupled and iterative analysis would be required to find a subset of the candidate modeling functions for an adequate model structure.

The quantities $\boldsymbol{q}_j^T \boldsymbol{z}$ are calculated for all n_c candidate modeling functions and are used to identify the model structure, which involves selecting the functions to be included in the model from the pool of n_c candidate modeling functions.

The orthonormal modeling functions to be included in the model are chosen to minimize the predicted squared error metric predicted squared error (PSE) defined by [refs. 15 and 20]:

$$\text{PSE} = \frac{1}{N}\left(\boldsymbol{z} - \boldsymbol{Q}\hat{\boldsymbol{a}}\right)^T\left(\boldsymbol{z} - \boldsymbol{Q}\hat{\boldsymbol{a}}\right) + \sigma_{max}^2 \frac{n}{N} \tag{6.3.6-11}$$

where the first term on the right is the mean squared fit error for the model, and the second term on the right is a model complexity penalty term proportional to the number of terms in the model, n. The latter term prevents overfitting the data with too many model terms, which is detrimental to model prediction accuracy [refs. 15 and 20]. The PSE metric quantifies expected squared prediction error for an identified model when applied to data not used in the model identification process. The constant σ_{max}^2 is an upper-bound estimate of the squared error between future data and the model (i.e., the upper-bound squared error for prediction cases). An estimate of σ_{max}^2 that is independent of the model structure can be obtained by applying a global optimal Fourier smoother [ref. 15] to the measured dependent variable data. This quantification of the dependent variable noise variance can then be multiplied by a safety factor to implement a conservative estimate for σ_{max}^2. The process is analogous to choosing a confidence level for an F-ratio test in model structure determination. In this assessment, the estimated dependent variable noise variance was multiplied by a factor of 25 (equal to a factor of 5 for the standard deviation) to obtain a conservative estimate of σ_{max}^2,

$$\sigma_{max}^2 = 25\hat{\sigma}^2 \quad \text{or} \quad \sigma_{max} = 5\hat{\sigma} \tag{6.3.6-12}$$

Using a conservative upper bound estimate for σ_{max}^2 means the PSE metric will tend to overestimate actual squared prediction errors for new data. Therefore, the PSE metric conservatively estimates the squared error for prediction cases.

Combining Equations (6.3.6-10) and (6.3.6-11) yields

$$\text{PSE} = \frac{1}{N}\left[\boldsymbol{z}^T\boldsymbol{z} - \sum_{j=1}^{n}\left(\boldsymbol{q}_j^T\boldsymbol{z}\right)^2\right] + \sigma_{max}^2 \frac{n}{N} \tag{6.3.6-13}$$

While the mean squared fit error must decrease with the addition of each orthonormal modeling function to the model (because $-\left(\boldsymbol{q}_j^T\boldsymbol{z}\right)^2$ is always negative), the model complexity penalty term $\sigma_{max}^2\, n/N$ must increase with each added model term (n increases). Introducing the orthonormal modeling functions into the model in order of most to least effective in reducing the mean squared fit error (quantified by $\left(\boldsymbol{q}_j^T\boldsymbol{z}\right)^2$ for the jth orthonormal modeling function) means that the PSE metric will always have a single global minimum.

Because the quantities $\boldsymbol{z}^T\boldsymbol{z}$, σ_{max}^2, and N depend only on the dependent variable data and therefore cannot be altered by the model, Equation (6.3.6-13) shows that the criterion for including each $\boldsymbol{q}_j$ in the model can be reduced to

$$\left(\boldsymbol{q}_j^T \boldsymbol{z}\right)^2 > \sigma_{max}^2 \tag{6.3.6-14}$$

The criterion in Equation (6.3.6-14) is the mathematical statement of a simple physical idea that only modeling functions that reduce the mean squared fit error by an amount that exceeds the maximum expected noise variance should be included in the model. This is the condition necessary for PSE to decrease when $\boldsymbol{q}_j$ is added to the model. Reference 20 contains further statistical arguments and analysis for the PSE metric, including justification for its use in modeling problems.

Using orthonormal functions to model the dependent variable data makes it possible to evaluate the merit of including each modeling function *individually*, based on the PSE metric. The goal is to select a model structure with minimum PSE, and the PSE always has a single global minimum for orthonormal modeling functions. Model structure determination based on the PSE metric is therefore a well-defined and straightforward process that can be (and was) automated.

The model parameters and uncertainties associated with the original modeling functions in the columns of the $\boldsymbol{X}$ matrix are determined from Equation (6.3.6-3), using all rows and columns of the $\boldsymbol{R}$ matrix up to and including the index associated with the last element of vector $\boldsymbol{Q}^T\boldsymbol{z}$ selected for the model [ref. 15]. SIDPAC program `mof.m` implements this model structure determination procedure using multivariate orthogonal functions and was used for this assessment. SIDPAC program `r_colores.m` was used to compute the model parameter uncertainties accounting for colored residuals.

Note that there are no requirements regarding the form of the candidate modeling functions - they can be multivariate polynomials, multivariate spline functions, or any other linear or nonlinear function that can be computed from the explanatory variable data. Inputs required from the analyst relate only to the limits of what should be considered (e.g., which explanatory variables to consider, maximum order of multivariate polynomial functions to consider, spline knot locations). Obviously, the identified model is dependent on the candidate modeling terms available for selection. However, the pool of candidate modeling terms can be specified generously, subject to computational constraints, because the modeling algorithm automatically sorts which terms are important, based on the data, and omits the rest. The result is a global parsimonious model that characterizes the functional dependencies accurately and predicts well.

6.3.7 Model Refinement using Output-Error

The results of equation-error modeling are an identified model structure (specific model terms selected for inclusion in the model) and estimates of the model parameters (multipliers for the selected model terms) and their uncertainties, based on the flight data. The previous subsections showed that equation-error results come from matching model outputs to flight data for the nondimensional aerodynamic force coefficients.

A common desire is to have model outputs match the physical system outputs. This can be done using the output-error approach, wherein model parameters are automatically adjusted inside a nonlinear simulation so that the simulation outputs match the physical system outputs in a weighted least-squares sense.

To do this effectively for the CPAS flight data, a nonlinear simulation of the two-parachute-with-payload dynamic system was required. Section 6.3.3 describes the development of the equations of motion for the two-parachute-with-payload dynamic system, as well as the development and testing of a nonlinear simulation implemented in MATLAB, based on these equations of motion. A modified version of this simulation, called the CP2 nonlinear simulation (for the capsule and two parachutes), was implemented in MATLAB and used for the output-error analysis and prediction testing. The CP2 nonlinear simulation differs from the nonlinear simulation described earlier, called CAPDYN, in that CP2 was developed with the simulation architecture and interfaces necessary for use with SIDPAC programs. CP2 also used standard SIDPAC routines for utilities (e.g., quaternion algebra, interpolation, and numerical integration). The CP2 nonlinear simulation was validated against CAPDYN using check cases, and CAPDYN was validated using analytic solutions, as described earlier and documented in Appendices A through J in Volume II. The CP2 nonlinear simulation was further validated by back-driving the CP2 nonlinear simulation with flight accelerations, and noting that this produced a perfect match with measured flight responses of the parachutes (see Figures 7.4-1 through 7.4-3).

Although it is possible to use FAST for output-error analysis (and that was attempted initially, with significant effort), FAST was not built to be used inside an output-error optimization loop, which is required for output-error parameter estimation. In addition, the long run times in FAST, the requirement to work remotely from NASA LaRC on NASA JSC computers (where FAST must run), and the difficulties in accessing and modifying the aerodynamic model in FAST, were practical problems that could not be overcome. This drove the need to develop the CP2 MATLAB simulation, which was less general than FAST (i.e., specific to the CPAS problem), but faster, easier to modify and test, and readily used in the SIDPAC output-error optimizer.

The CP2 nonlinear simulation implemented equations of motion for the two-parachute-with-payload dynamic system, which can be described by the following general nonlinear equations of motion:

$$\frac{d\boldsymbol{x}}{dt} = f\left[\boldsymbol{x}(t), \boldsymbol{u}(t), \boldsymbol{\theta}\right] \qquad \boldsymbol{x}(0) = \boldsymbol{x}_o \tag{6.3.7-1a}$$

$$\boldsymbol{y}(t) = h\left[\boldsymbol{x}(t), \boldsymbol{u}(t), \boldsymbol{\theta}\right] \tag{6.3.7-1b}$$

$$\boldsymbol{z}(i) = \boldsymbol{y}(i) + \boldsymbol{v}(i) \qquad i = 1, 2, \ldots, N \tag{6.3.7-1c}$$

where f represents the nonlinear equations of motion, h represents equations for computing the outputs, $\boldsymbol{x}(t)$ is the state vector for the parachute cluster at time *t*, which includes positions and velocities of the parachutes and payload, $\boldsymbol{u}(t)$ represents the input vector to the dynamic system at time, *t*, which is composed of estimated winds aloft in this case, and the elements of the unknown parameter vector $\boldsymbol{\theta}$ are aerodynamic model parameters, such as those shown on the right side of Equation (6.3.5-3). The discrete measured output vector is $\boldsymbol{z}(i)$, the discrete model output vector is $\boldsymbol{y}(i)$, and $\boldsymbol{v}(i)$ is the discrete output measurement noise. Note that the nonlinear simulation is built to compute outputs at the discrete measurement times associated with the measured outputs from flight data $\boldsymbol{z}(i)$, using estimated winds aloft for $\boldsymbol{u}(t)$, current values of the model parameters $\boldsymbol{\theta}$, and a Runge-Kutta numerical method to solve the nonlinear equations of motion.

The unknown parameters in vector $\boldsymbol{\theta}$ can be estimated from measured data using an output-error formulation. In this approach, $\boldsymbol{\theta}$ is chosen to minimize the cost function

$$J(\boldsymbol{\theta}) = \frac{1}{2}\sum_{i=1}^{N}\left[\boldsymbol{z}(i) - \boldsymbol{y}(i)\right]^T \boldsymbol{R}^{-1}\left[\boldsymbol{z}(i) - \boldsymbol{y}(i)\right] \tag{6.3.7-2}$$

where $\boldsymbol{R}^{-1}$ is a weighting matrix. This cost function represents minimizing the weighted sum of squared differences between the measured outputs $\boldsymbol{z}$ and the model outputs $\boldsymbol{y}$ for the same measured input $\boldsymbol{u}$. For the current problem, the measured outputs to be matched might be true airspeed of each parachute and various angular deflections of the parachute cluster, among other outputs, and the measured inputs are the estimated winds aloft. This formulation is called "output error" because the unknown parameters are chosen to minimize the weighted squared-error between the physical measured outputs and the model outputs computed using a simulation.

The weighting matrix $\boldsymbol{R}^{-1}$ is, in general, arbitrary, but if the noise $\boldsymbol{v}$ in Equation (6.3.7-1c) is assumed to be zero-mean Gaussian and $\boldsymbol{R}$ is chosen as the discrete noise covariance matrix, i.e.,

$$\boldsymbol{v} \text{ is } \mathbf{N}(\mathbf{0}, \boldsymbol{R}) \tag{6.3.7-3a}$$

$$Cov\left[\boldsymbol{v}(i)\right] = E\left[\boldsymbol{v}(i)\,\boldsymbol{v}^T(j)\right] = \boldsymbol{R}\,\delta_{ij} \tag{6.3.7-3b}$$

then minimizing the cost function in Equation (6.3.7-2) corresponds to maximizing a Gaussian likelihood function, which means that the resulting parameter estimates are maximum likelihood estimates. Maximum likelihood parameter estimates have several desirable properties as the number of data points gets large (e.g., being unbiased, approaching the true value, and having error bounds that approach the theoretical minimum).

Because of the nonlinearity of the cost function in Equation (6.3.7-2), along with the generally coupled dynamics in Equations (6.3.7-1), the output-error cost function depends nonlinearly on the unknown parameter vector $\boldsymbol{\theta}$. Consequently, output-error parameter estimates must be computed using a nonlinear optimization method. Typically, a relaxation method is used with the modified Newton-Raphson method (also called the Gauss-Newton method) and the simplex method (see reference 15 for details). When this process converges, an estimate for the noise covariance matrix $\boldsymbol{R}$ can be found from the simple closed-form expression:

$$\hat{\boldsymbol{R}} = \frac{1}{N}\sum_{i=1}^{N}\left[\boldsymbol{z}(i) - \boldsymbol{y}(i)\right]\left[\boldsymbol{z}(i) - \boldsymbol{y}(i)\right]^T \tag{6.3.7-4}$$

where $\hat{\boldsymbol{R}}$ is the value of $\boldsymbol{R}$ that minimizes the cost function in Equation (6.3.7-2) given that the parameters $\boldsymbol{\theta}$ are fixed. The relaxation method alternates between the nonlinear optimization to estimate $\boldsymbol{\theta}$ and the closed-form $\boldsymbol{R}$ matrix update in Equation (6.3.7-4), until estimates of both $\boldsymbol{\theta}$ and $\boldsymbol{R}$ converge. This procedure has been mechanized in SIDPAC program `oe.m` and used successfully for a wide variety of aerospace dynamic modeling problems. Reference 15 provides further theoretical and practical details on the output-error parameter estimation method and the solution procedure outlined here. The output-error solution, therefore, includes maximum likelihood estimates for both the unknown parameter vector $\boldsymbol{\theta}$ and the noise covariance matrix $\boldsymbol{R}$, where the estimates from flight data are denoted by $\hat{\boldsymbol{\theta}}$ and $\hat{\boldsymbol{R}}$, respectively.

In practice, the number of data points for most flight test maneuvers is large because of relatively high sample rates used to collect data for dynamic analysis, and the parameter covariance matrix can be computed using maximum likelihood estimates $\hat{\boldsymbol{\theta}}$ and $\hat{\boldsymbol{R}}$ as [ref. 15]:

$$Cov\left(\hat{\boldsymbol{\theta}}\right) = \left[\sum_{i=1}^{N} \boldsymbol{S}^T(i)\, \hat{\boldsymbol{R}}^{-1}\, \boldsymbol{S}(i)\right]^{-1} \tag{6.3.7-5}$$

The quantity $\boldsymbol{S}(i)$ is the output sensitivity matrix, which quantifies the sensitivity of the model outputs to the model parameters, with model parameters equal to their estimated value

$$\boldsymbol{S}(i) = \left.\frac{\partial \boldsymbol{y}(i)}{\partial \boldsymbol{\theta}}\right|_{\boldsymbol{\theta}=\hat{\boldsymbol{\theta}}} \tag{6.3.7-6}$$

Output sensitivities can be calculated analytically by solving a set of sensitivity equations derived by differentiating Equations (6.3.7-1) with respect to $\boldsymbol{\theta}$, or by finite differences applied to Equations (6.3.7-1). Reference 15 provides theoretical and practical details on computing output sensitivities and solving the output-error parameter estimation problem.

When the columns of the output sensitivity matrix (the output sensitivity to individual parameters) are linearly independent and nonzero, each model parameter has a unique and significant impact on the model outputs, so that minimizing the output error will be a well-conditioned optimization problem leading to accurate values for the unknown parameters, with small uncertainties. The inputs will influence the output sensitivities through the dynamic and output Equations (6.3.7-1) and the covariance matrix calculation (Equation (6.3.7-5)). Output noise levels (quantified by $\hat{\boldsymbol{R}}$) also affect the covariance matrix calculation in Equation (6.3.7-5). In a rough sense, the covariance matrix is determined by squared noise-to-signal ratio, where $\hat{\boldsymbol{R}}$ represents the noise variance (square of the noise level) and the output sensitivities $\boldsymbol{S}(i)$ represent the signal for the parameter estimation problem.

The estimated parameter standard errors are computed as the square root of the diagonal elements of the covariance matrix

$$\hat{\sigma}_j = \sqrt{C_{jj}} \qquad j = 1, 2, \ldots, n \tag{6.3.7-7}$$

The 95% confidence interval for each estimated parameter is based on the Gaussian distribution assumption for the measurement noise and the likelihood function and can be calculated as

$$\theta_j \in \left[\hat{\theta}_j - 2\hat{\sigma}_j, \hat{\theta}_j + 2\hat{\sigma}_j\right] \qquad j = 1, 2, \ldots, n \tag{6.3.7-8}$$

The estimated parameter uncertainty calculations in Equations (6.3.7-5) through (6.3.7-8) are based on the assumption that the model residuals are white Gaussian noise. In practice, however, the model residuals are typically not white Gaussian with constant variance, as assumed in the theory, but are colored (time correlated) with non-uniform variance, typically as a result of relatively small model structure errors or unmodeled effects. The mismatch between theory and practice regarding the character of the model residuals results in estimated parameter uncertainty bounds that are overly optimistic (too small) when computed using the standard procedure of Equations (6.3.7-5) through (6.3.7-8). References 15 and 16 describe a rigorous and flight-validated solution to this problem, which involves improving the $\hat{\boldsymbol{R}}$ estimate and using that improved estimate to compute a corrected covariance matrix. The necessary correction can be done as a post-processing of the model residuals because only the covariance matrix is affected (and consequently the estimated parameter uncertainties), but not the parameter estimate $\hat{\boldsymbol{\theta}}$. The computations are analogous to those used to correct the parameter uncertainties for equation-error parameter estimates, which were described earlier. This post-processing was applied using SIDPAC program `m_colores.m` to compute accurate parameter uncertainties for the output-error modeling results.

7.0 Data Analysis

This section describes the system identification methods used to develop parachute aerodynamic models from flight data. A general description of the equation-error and output-error modeling approaches are provided in Sections 6.3.5 and 6.3.7 and can be found in reference 15. The material describing multivariate orthogonal function modeling is provided in Section 6.3.6 and is based on references 15 and 17–19. Data analysis and modeling tasks in this assessment were done using SIDPAC software written in MATLAB [refs. 15 and 21].

Flight data came mainly from onboard instrumentation and videogrammetry. Airspeed, total angle of attack, aerodynamic azimuth angle, and dynamic pressure came from the BET data, which was based on flight instrumentation data and estimated atmospheric conditions and winds aloft at the time of the flight test. Flight data from onboard instrumentation were corrected for data dropouts and were interpolated to a uniform sampling rate. Sample rate for the flight data used in the analysis and modeling was 10 Hz, corresponding to a sampling interval of 0.10 s. CPAS mass, geometry, and tension line properties are given in Table 6.1.1.

7.1 Results for Pendulum Motion Modeling using Simplified Linear Equations and Defined Aerodynamic Model Structure

The first CPAS drop test with two main parachutes that exhibited significant pendulum motion was CDT 3-11 [refs. 2 and 3]. According to reference 2, one-third of the way into the full open portion of the main parachute flight, the system developed a swinging motion of approximately 15 degrees in amplitude, which increased up to 24 degrees as it approached the ground. During the pendulum motion, the system was translating toward the Northeast due to the direction of the wind as it descended. The parachute cluster appears to have aligned its “weak" axis with the direction of the wind. Reference 3 defines the “weak" axis as being parallel with the wind direction and orthogonal to the plane of oscillation that contains the two parachutes. The motion can be approximated as planar in nature; hence, Equations 6.3.1-5 through 6.3.1-11 should be adequate for capturing the gross characteristics of the pendulum motion. The simplified planar model, however, does not predict the onset of the pendulum motion nor does it predict system behavior with no pendulum motion.

It is important to note that in Section 6.3.1.2, a linear analysis (small disturbance theory) was performed by linearizing the nonlinear C_N versus α curve shown in Figure 6.3.1-2 about one of the stable equilibrium points at $\pm\alpha_o$ and yields many insights into the pendulum motion using the concept of the pivot point. However, in reality the pendulum motion is a nonlinear phenomenon at which the parachutes sustain large oscillations between the two stable trim points at $\pm\alpha_o$. Reference 6 provides nonlinear analysis of the pendulum motion.

As a part of the nonlinear analysis of the pendulum motion described in reference 6, the output-error method [ref. 15], widely used in parameter estimation for aircraft, was applied to the pendulum portion of the CDT 3-11 flight data. To perform the optimization, the routine called `oe.m` in the SIDPAC toolbox [ref. 21] was used. The vector of parameters to be estimated was

$$\Theta = [C_{A_o} \quad C_{A_\alpha} \quad \alpha_o \quad C_{N_\alpha} \quad C_{N_{\dot{\alpha}}}] \tag{7.1.1}$$

The aerodynamic model structures shown in Equations 6.3.1-10 and 6.3.1-11 are based on previous studies [refs. 7, 8, 11, and 12] and are not identified from the flight data. An additional damping term, $C_{N_{\dot{\alpha}}}$, was added in Equation (6.3.1-12) to account for unsteady time lag effects in the rotational DOF [refs. 5 and 9]. The MPCV aerodynamic database suggests that for pendulum motion to occur an unstable (negative) value of $C_{N_{\dot{\alpha}}}$ is required. The measurements from the flight data to match are θ (swing angle), $V_{\mathrm{n_3,air}}$ (air relative velocity in the Down direction), and $V_{\mathrm{lat,air}}$ (root-sum-square of the air relative velocity in North and East directions). System properties used in the planar dynamics model are recorded in Table 7.1-1. Note that these properties differ slightly compared with the nominal properties used for System ID given in Table 6.1.1. Furthermore, the simplified model assumes constant air density and, hence, a constant m_C.

Table 7.1-1. Approximate CPAS Properties used for Modal Analysis

Parameter	Value	Units
S_{ref} (single parachute)	10,563	ft^2
L	235	ft
Capsule weight, W_L	21,906	lbf
Dry weight of two parachutes, W_C	656	lbf
Total mass of two parachutes, (dry and entrapped air), m_C	614	slugs
Distance from system CM to capsule CM, R_L	114	ft
Line spring constant, K	15,000	lbf/ft
Line damping constant, η	10,000	lbf-s/ft

Winds act as the main source of excitation to the two-parachute cluster system. In the flight data, the best estimated winds are provided in the NED directions. For flight winds to be used in the planar dynamics model, the flight winds in the North and East directions were resolved along the plane of the pendulum oscillation, as shown in Figure 7.1-1. Output-error analysis converged within 80 iterations. Figure 7.1-2 shows a comparison between the output-error model and the flight data. Other than the initial amplitude mismatch during the first 15 seconds (s), the identified planar model appears to provide a good match with flight data in the swing-angle time history. The fundamental frequency (0.068 Hz) of the swing angle is virtually identical between the identified model and the flight data, while there appears to be a 2-second phase lag toward the end of the data set. The model swing-angle amplitude is within 20% of the flight data. $V_{\mathrm{lat,air}}$ from the flight data and the model also compare well. The slightly larger differences in $V_{\mathrm{n_3,air}}$ are likely due to the lack of best estimated winds in the Down direction. Considering the drastic simplification of the actual system dynamics (e.g., 18 DOF, flexible riser lines, non-rigid parachutes), it is noteworthy that the fundamental characteristics of the pendulum motion can be captured using only three output variables (swing angle, $V_{\mathrm{lat,air}}$, $V_{\mathrm{n_3,air}}$).

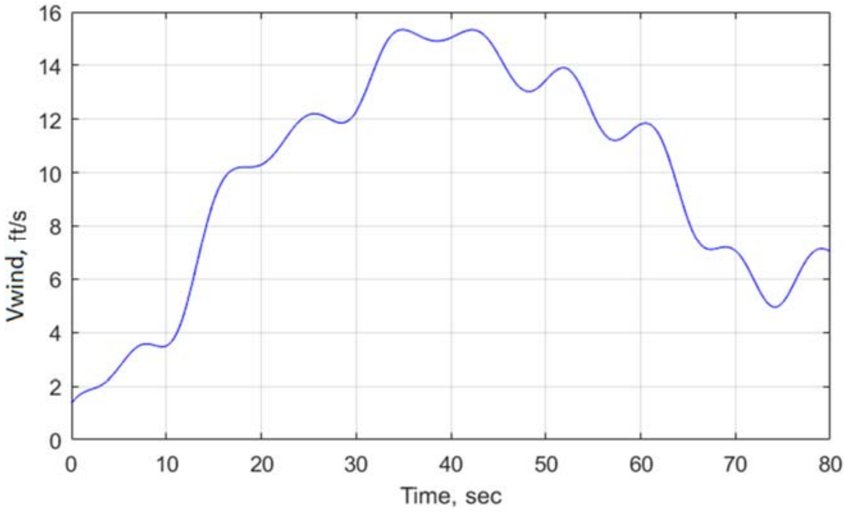

Figure 7.1-1. CDT 3-11 Flight Winds

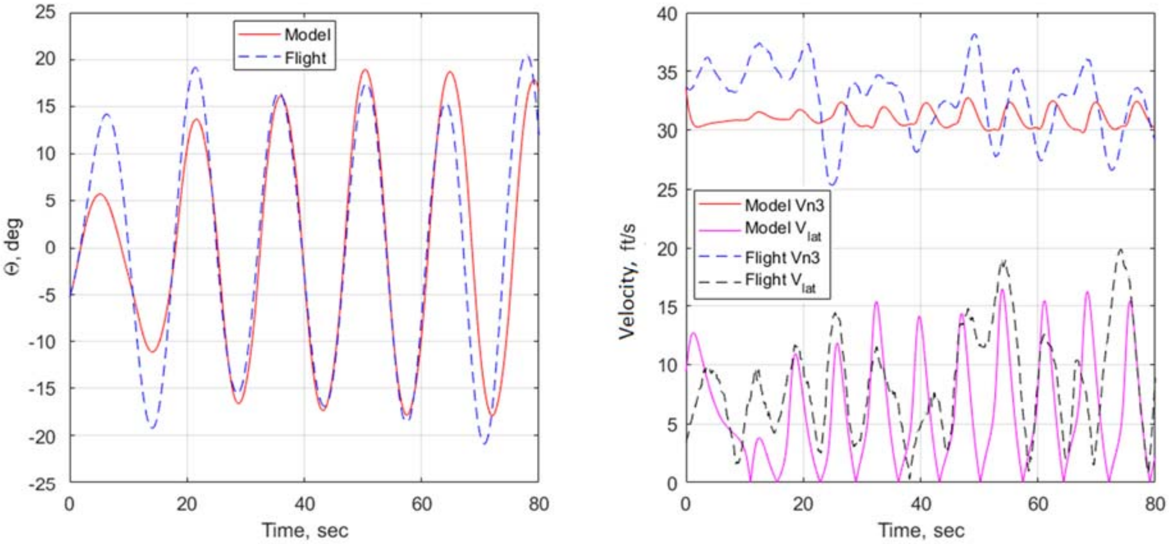

Figure 7.1-2. Output-error Model with CDT 3-11 Flight Data

Table 7.1-2 shows the parameter estimation results from the output-error method by using the planar pendulum model described in Section 6.3.1 to match the pendulum portion of the 3-11 flight. The estimated parameters and their standard errors are listed in columns 2 and 3, respectively. The standard errors were corrected for colored residuals using the `m_colores.m` function in SIDPAC [ref. 21]. The standard error on $C_{N_{\dot{\alpha}}}$ is about 48% of the estimated parameter value, which is fairly high. This is largely due to the initial mismatch between the model and flight. The standard error on C_{N_α} drops to 20% of the estimated value if data only between 30 and 60 seconds are considered. Furthermore, the large standard error on C_{N_α} may be attributed to model structure error by assuming a constant value of $C_{N_{\dot{\alpha}}}$. In the current MPCV aerodynamic database, $C_{N_{\dot{\alpha}}}$ is a function of α.

Figures 7.1-3 to 7.1-5 compare the identified C_N, $C_{N_{\dot{\alpha}}}$, and C_A versus α models with the current MPCV aerodynamic database. For the static C_N model, the trends are similar, with the database showing a greater value for α_o but a shallower slope value of C_N at α_o (smaller restoring force). For the damping derivative, the model indicates a constant $C_{N_{\dot{\alpha}}}$, whereas the database shows variations with α. Furthermore, the model shows significantly higher value of $C_{N_{\dot{\alpha}}}$ (more dynamic instability). For C_A, the database and the model show similar trends, with the database having a constant value of C_A between $\alpha = -16$ and 16 degrees.

Table 7.1-2. Pendulum Mode Parameter Estimation Results from CDT 3-11

Parameter	$\hat{\Theta}$	$s(\hat{\Theta})$
C_{A_o}	0.927	0.034
C_{A_α} (rad^{-1})	–0.329	0.179
α_o (rad)	0.189	0.038
C_{N_α} (rad^{-1})	0.1901	0.091
$C_{N_{\dot{\alpha}}}$ (rad/s)$^{-1}$	–0.988	0.0684

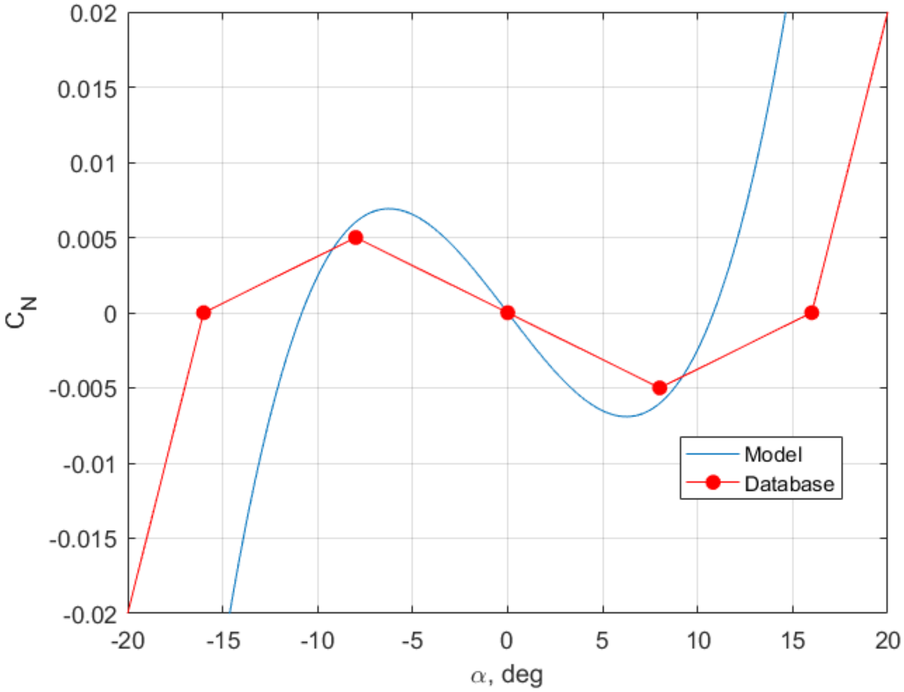

Figure 7.1-3. C_N versus α, Identified Model versus MPCV Database

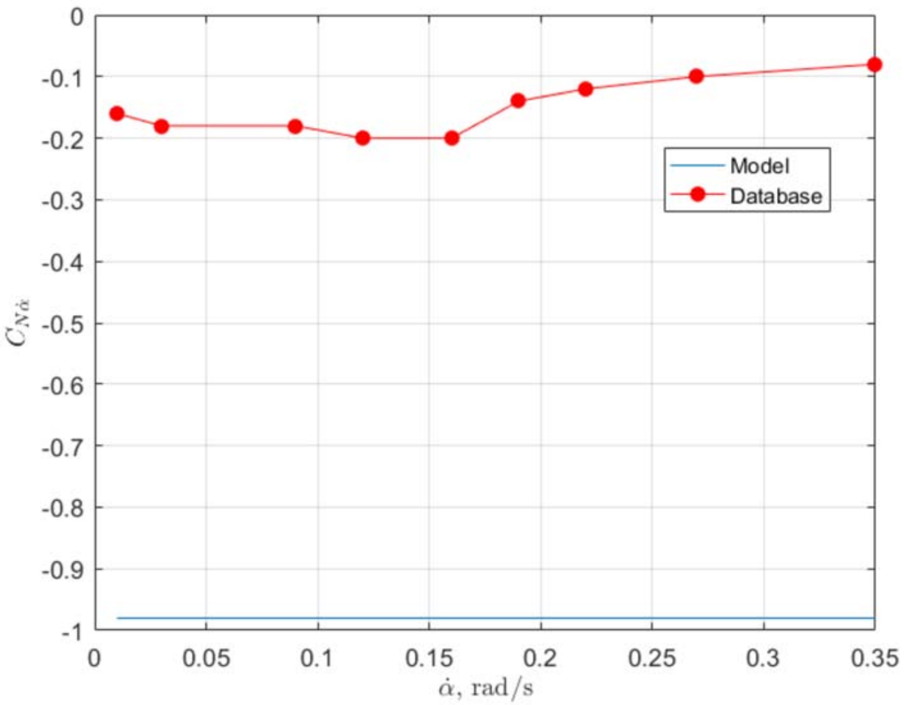

Figure 7.1-4. $C_{N\dot{\alpha}}$ versus α, Identified Model versus MPCV Database

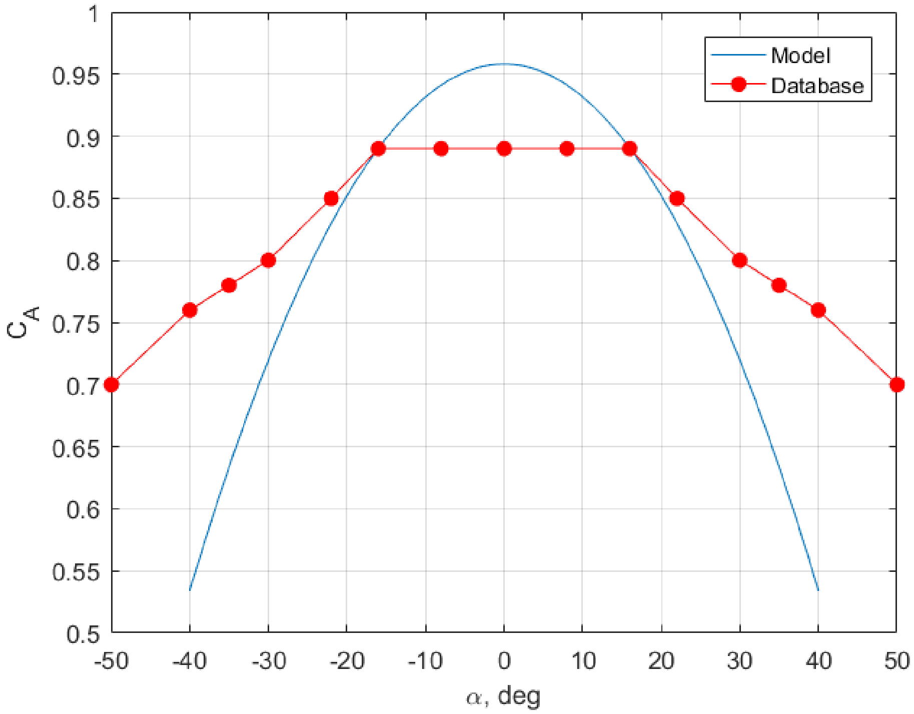

Figure 7.1-5. C_A versus α, Identified Model versus MPCV Database

As part of the model validation, the parameters identified from the pendulum portion of the CDT 3-11 flight shown in Table 7.1-2 were used to predict the pendulum motion from the CDT 3-12 flight. According to reference 2, during the CDT 3-12 drop test the pendulum motion occurred almost immediately after full inflation of the main parachutes and gradually increased to an amplitude of approximately 24 degrees until impact. Similar to the CDT 3-11 flight, the system was also translating toward the Northeast due to the direction of the winds as it descended. Figure 7.1-6 shows the CDT 3-12 flight winds resolved in the plane of the pendulum oscillation, which were used in the simulation as a forcing function. Figure 7.1-7 shows a comparison of the model (using the aero parameters identified from the CDT 3-11 flight) with the CDT 3-12 flight data. Once again, other than the initial amplitude mismatch, the identified planar model appears to provide an excellent match with flight data in the swing-angle time history. Both model and flight data show the swing angle fundamental frequency to be 0.07 Hz, while error in the amplitude of oscillation is within 10%. $V_{n_3,\mathrm{air}}$ and $V_{\mathrm{lat,air}}$ also show good comparisons.

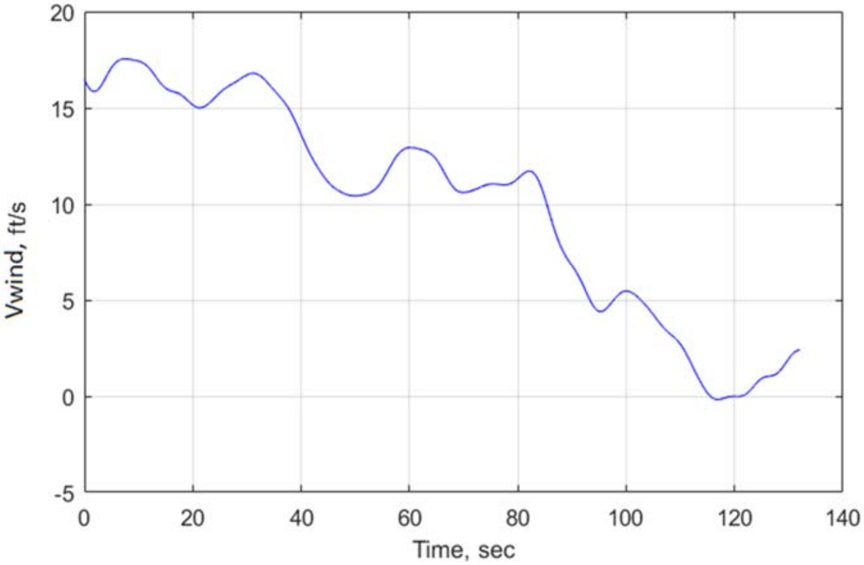

Figure 7.1-6. CDT 3-12 Flight Winds

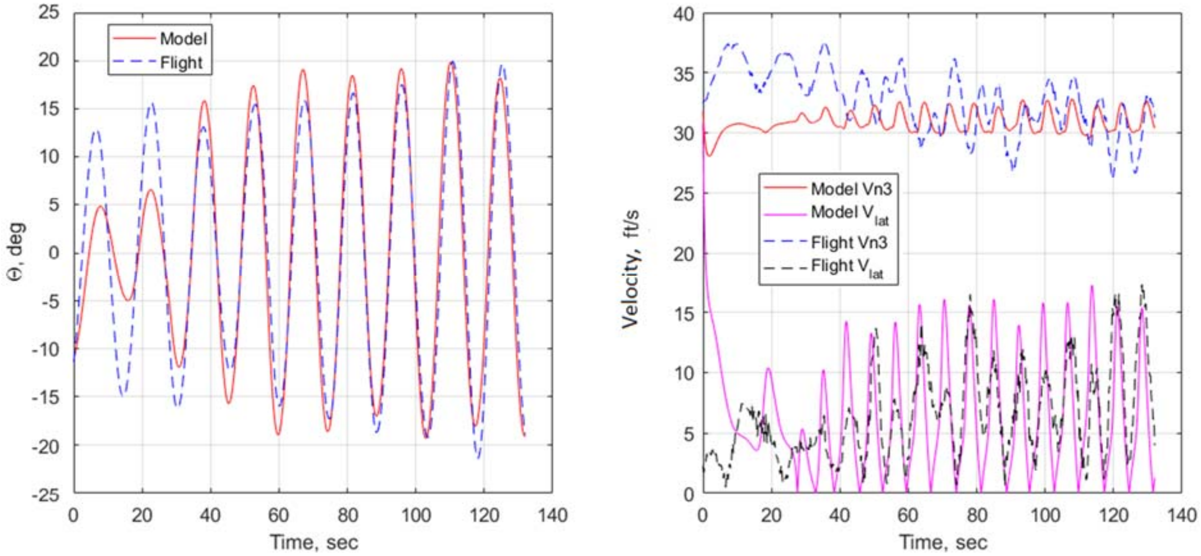

Figure 7.1-7. Prediction Test using CDT 3-12 Flight Data

It is apparent from Figures 7.1-2 and 7.1-7 that the identified planar dumbbell model does a good job matching the underlying dynamics of the pendulum motion from both the CDT 3-11 and 3-12 flight data. However, its limitations should be reemphasized. The dumbbell model is not capable of producing some of the more complicated behaviors (e.g., the maypole and flyout motions) observed during the CDT 3-02 and 3-08 flights in which the pendulum motion did not occur [refs. 2 and 3]. The model also does not predict how pendulum motion is triggered. Visual inspection of the flight data with pendulum motion (3-11 and 3-12) and without pendulum motion (3-02 and 3-08) suggests there is a correlation between a large gradient in the wind direction while the magnitude exceeds a certain threshold and propensity to pendulum motion. It is a topic for future research.

Finally, the current model does not provide much insight into why a cluster of three parachutes is more resistant toward the pendulum motion compared with a cluster of two parachutes. According to reference 3, CDT 3-07 involved three parachutes. Pendulum motion was observed during a brief interval in which the configuration of the parachutes changed from the usual triangular arrangement to a collinear one with coincident projections of all three parachutes onto the plane parallel to the wind direction. The oscillations damped out after the parachutes regained their triangular configuration. Equations 6.3.1-5 through 6.3.1-11, therefore, are applicable in the case of pendulum motion with three parachutes, with the following modifications: 1) W_C and M_C are the dry weight and total mass of three parachutes, and 2) a coefficient of 3 replaces 2 in Equations 6.3.1-8 and 6.3.1-9.

Simulations of the planar pendulum model with the identified output error nonlinear aerodynamics based on CDT 3-11 were performed to provide further insight into the pendulum motion. This is similar to the large disturbance studies described in reference 7. The left plot in Figure 7.1-8 shows the swing angle time history, and the right plot shows the phase portrait of the parachute α. The blue dots represents the two stable equilibrium points at $\pm\alpha_o$ (reference 7 refers to α_o as the stable glide point), while the green dot represents the unstable equilibrium point at $\alpha = 0$. The parachute-capsule system starts out in a steady descent and is subject to a disturbance in θ. Due to the unstable aerodynamic damping, the parachute immediately seeks out the stable equilibrium at $+\alpha_o$ and attempts to trim there. Meanwhile, the swing angle amplitude is still fairly small (between ~ ±0.1 rad). However, due to the negative damping, the parachute is unable to stay at $+\alpha_o$ and jumps to the other stable equilibrium at $-\alpha_o$ (crossing $\alpha = 0$ along the way). Eventually, the system manifests into a stable limit cycle where the parachutes oscillate back and forth between the two stable equilibrium α, resulting in large swing angles (±0.4 rad or 23 degrees).

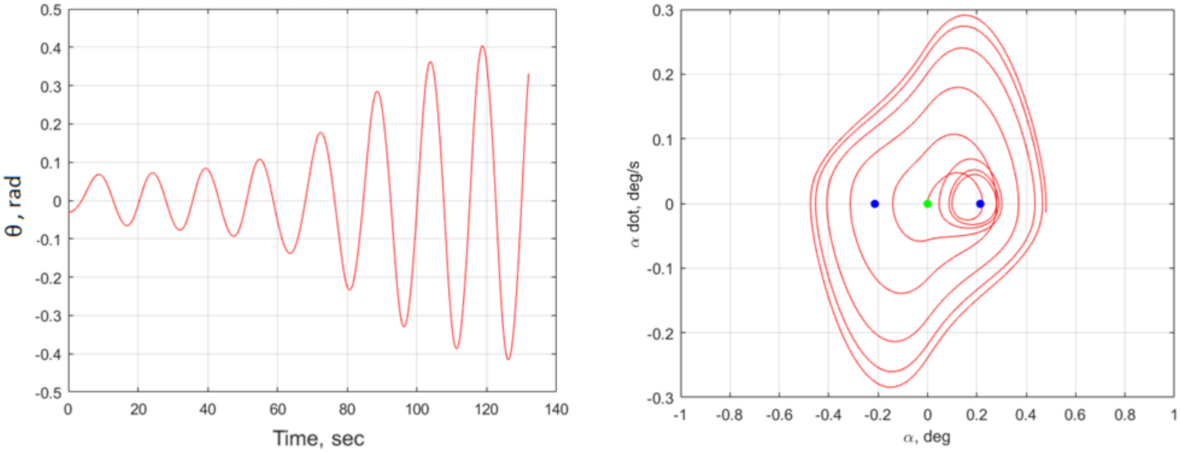

Figure 7.1-8. Simulation of Planar Pendulum Model with Identified Output Error Model (swing angle (left), angle of attack phase portrait (right))

Figure 7.1-9 shows simulation results of the same system, except, at $T = 50$ seconds, positive (stable) aerodynamic damping is artificially introduced. Due to the large initial swing angle and rate, the system almost immediately develops into the limit cycle oscillation (α jumps from 0 to $\pm\alpha_o$). At $T = 50$ seconds, the sign on $C_{N\dot{\alpha}}$ is flipped from negative to positive. The stable aerodynamic damping causes the amplitude of the swing angle to diminish gradually over time (reducing the kinetic energy of the system). At around $T = 160$ sec, the parachute eventually settles at one of the stable equilibrium α, and the amplitude of the swing angle asymptotically reduces to zero. Note that this is merely a simulation study highlighting the role of the unstable aerodynamic damping. In reality, due to the passive nature of the system, once the pendulum motion occurs there is little that can be done to stop the limit cycle oscillation.

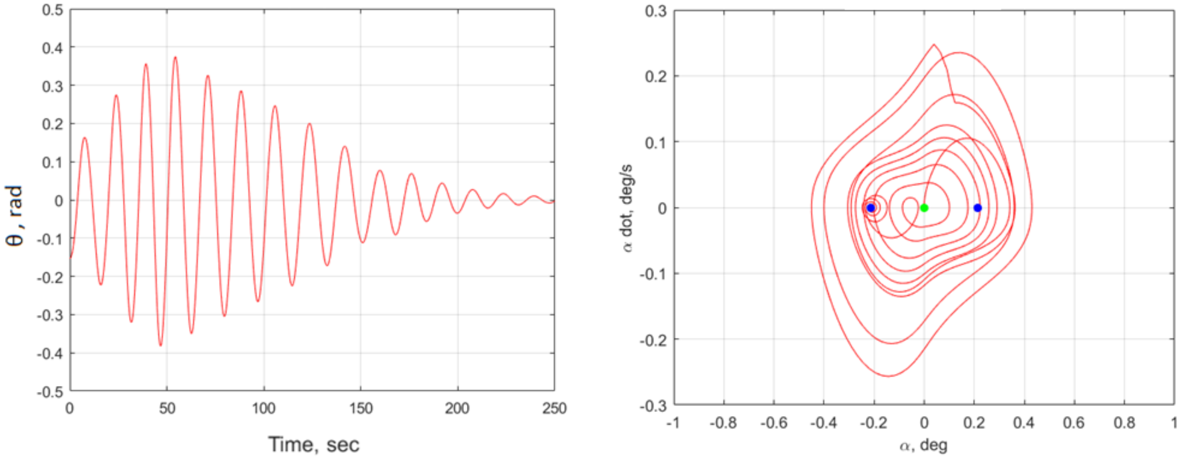

Figure 7.1-9. Simulation of Planar Pendulum Model with Identified Output Error Model (stable damping at T = 50 seconds; swing angle (left), angle of attack phase portrait (right))

Similar analysis was performed for the four possible parachute designs (i.e., statically unstable/dynamically unstable, statically stable/dynamically unstable, statically unstable/dynamically stable, and statically stable/dynamically stable) and the resultant pendulum motion. Figure 6.3.1-2 illustrates the difference in the C_N versus α curve between a statically stable versus a statically unstable parachute. The unstable configuration has three trim points:

unstable equilibrium at $\alpha = 0$ and stable equilibrium at $\alpha = \pm\alpha_o$. $C_{N\dot{\alpha}}$ is positive for a dynamically stable configuration and negative for a dynamically unstable configuration.

Figure 7.1-10 illustrates the case of the statically unstable/dynamically unstable configuration (current Orion parachutes). For the given initial swing angle and rate, the system immediately develops into a large limit cycle oscillation ($\theta \sim \pm 0.4$ rad or 23 degrees), and the parachute α oscillates back and forth between the $\pm\alpha_o$ equilibrium points.

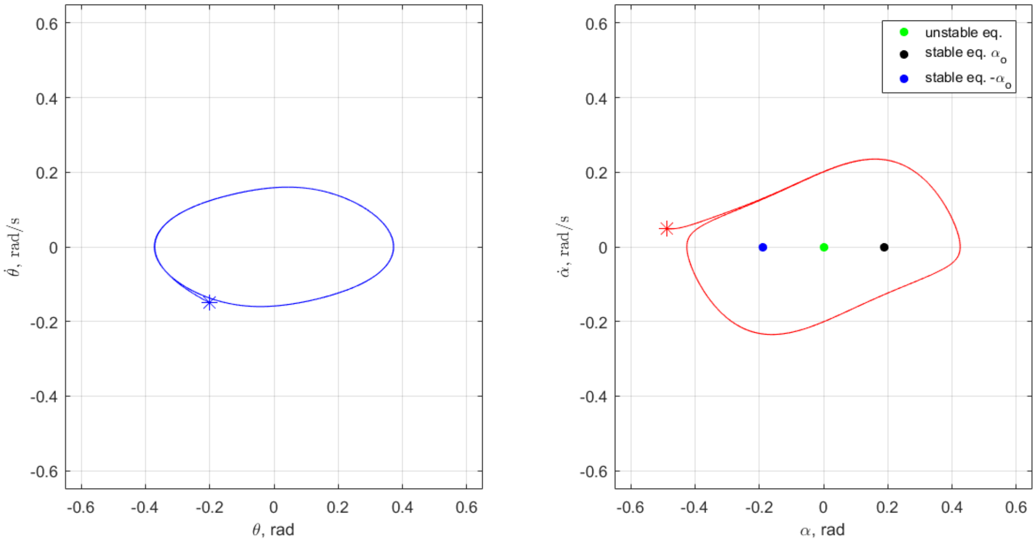

Figure 7.1-10. Statically Unstable and Dynamically Unstable Configuration; Swing Angle Phase Portrait (left), Angle of Attack Phase Portrait (right)

Figure 7.1-11 illustrates the case of the statically stable/dynamically unstable configuration. The system sustains oscillation about the sole equilibrium point at $\alpha = 0$. The amplitude of the swing angle limit cycle is, however, much smaller compared with the statically/dynamically unstable case ($\theta < \pm 0.2$ rad). According to reference 10, in the parachute community, the system illustrated in Figure 7.1-10 is considered unstable, and the system shown in Figure 7.1-11 is considered stable. As discussed in Section 6.3.1, one method for improving the static stability of the parachute is to increase its porosity. This comes at the expense of increasing descent rate.

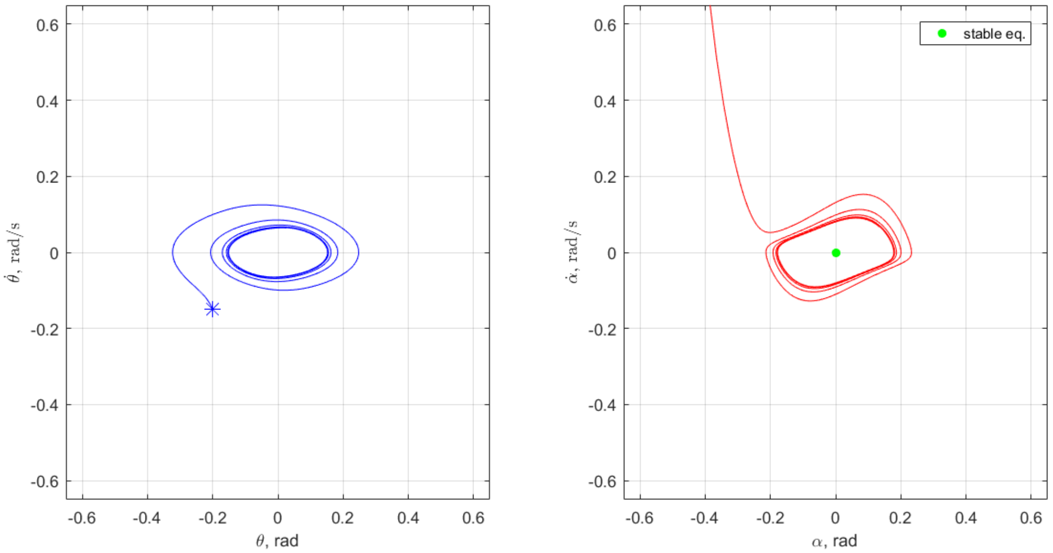

Figure 7.1-11. Statically Stable and Dynamically Unstable Configuration; Swing Angle Phase Portrait (left), Angle of Attack Phase Portrait (right)

Figure 7.1-12 illustrates the case of the statically unstable/dynamically stable configuration. For the given initial swing angle and rate, the system trims at the $-\alpha_0$ equilibrium point. Due to the stable damping coefficient, the swing angle asymptotically goes to zero. In steady state, the motion can be described as a "gliding" descent. To change the dynamic stability of the system, gaps and ring sails must be strategically placed on the parachute.

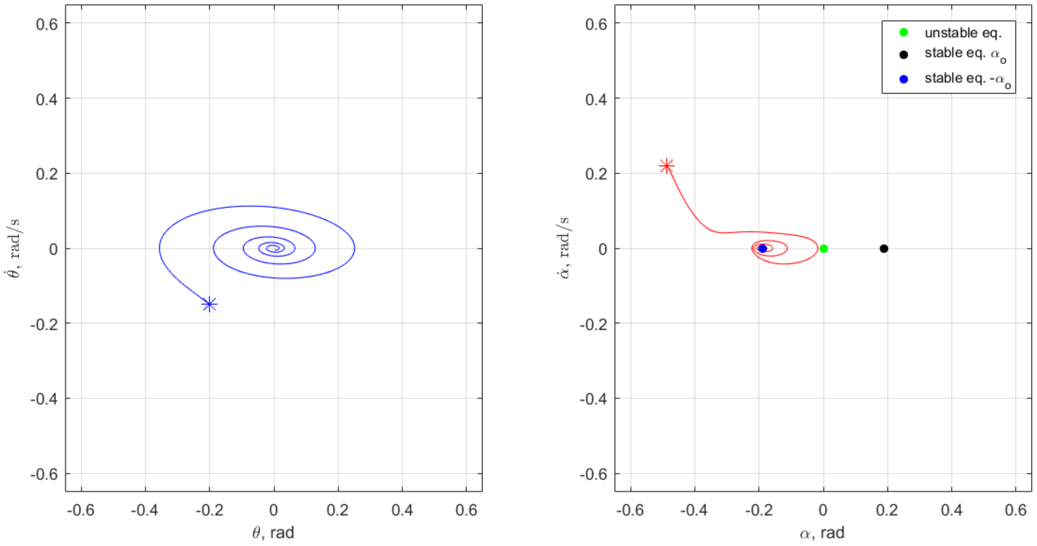

Figure 7.1-12. Statically Unstable and Dynamically Stable Configuration; Swing Angle Phase Portrait (left), Angle of Attack Phase Portrait (right)

Figure 7.1-13 illustrates the case of the statically stable/dynamically stable configuration. The system trims at the stable equilibrium point of $\alpha = 0$ degrees, while the swing angle asymptotically goes to zero. In steady state, the motion can be described as a vertical descent.

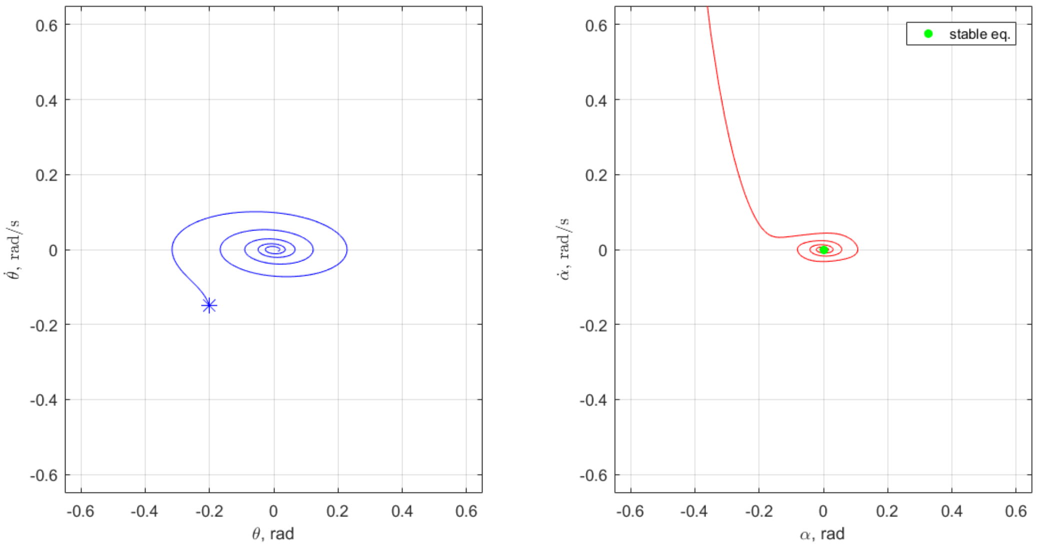

Figure 7.1-13. Statically Stable and Dynamically Stable Configuration; Swing Angle Phase Portrait (left), Angle of Attack Phase Portrait (right)

7.2 Modal Analysis Results

7.2.1 Flyout Mode

The flyout/scissors motion observed during the CDT 3-02 and 3-08 flights is shown in Figure 7.2.1-1. The motion is approximately planar in nature. The red and blue curves indicate the paths traced out by the parachutes relative to the capsule during one cycle of the flyout motion. The observed period of oscillation from both flights is roughly 15 seconds. From Equation (6.2.2.1-9), a value of $(C_{N_\alpha})_{\text{tot}} = 1.2\ \text{rad}^{-1}$ can be determined. A value of 0.2 rad^{-1} was determined for $(C_{N_\alpha})_{\text{fs}}$ from the pendulum motion analysis shown in Table 7.1-2. This suggests that $(C_{N_\alpha})_{\text{prox}}$ should be on the order of 1 rad^{-1}.

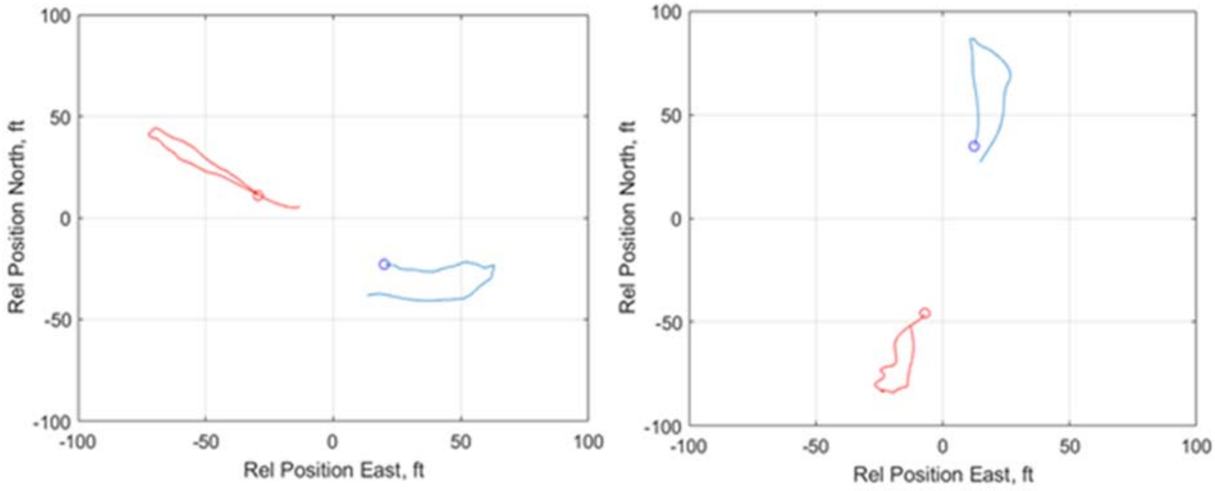

Figure 7.2.1-1. Flyout/Scissors Motion from Flight Data (CDT 3-02 (left), CDT 3-08 (right))

Figure 7.2.1-2 shows derived measurements taken during the CDT 3-02 flight of the total normal force coefficient, $(C_{N_\alpha})_{\text{tot}}$, resolved along the proximity axis with the corresponding proximity distance, D_{prox}, for each parachute. D_{prox} is normalized by the nominal diameter of the parachutes, 116 ft. The data are fairly linear for $0.6 \leq D_{\mathrm{prox}} \leq 1$ and flatten out for $D_{\mathrm{prox}} > 1$. The red line indicates a least squares linear fit. It is apparent that $(C_N)_{\mathrm{tot}}$ has an equilibrium at D_{prox} of 0.6 (or $\theta_o = \theta_1 = \theta_2 = 0.15$ rad). The slope of the least squares fit is approximately $1.25\ \mathrm{rad}^{-1}$, consistent with the analysis of the scissors motion in isolation as described in the previous paragraph. The scatter in the plots is due in part to the multidimensional nature of the data set (e.g., C_N is also a function of $\dot{\alpha}$, V_{prox}, etc.). Similar exercises were performed for the CDT 3-08, CDT 3-11, and CDT 3-12 flights, all of which yielded consistent results (see Figures 7.2.1-3 through 7.2.1-5).

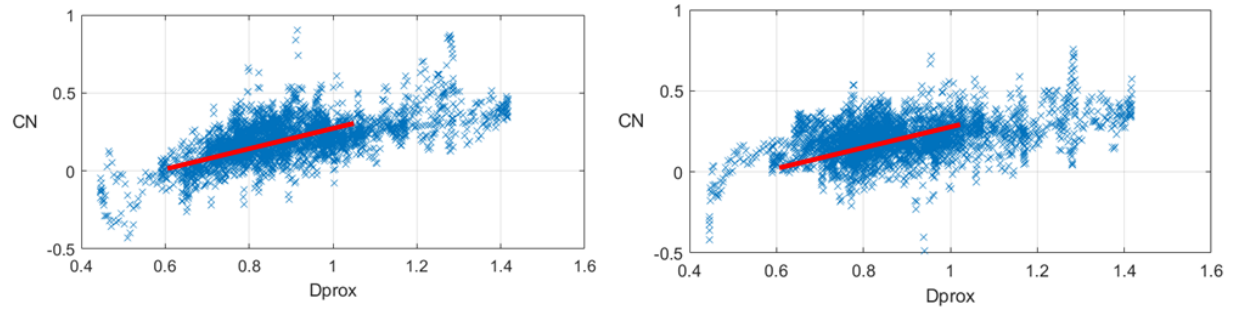

Figure 7.2.1-2. ***$(C_N)_{tot}$ from CDT 3-02 (parachute #1 (left), parachute #2 (right))***

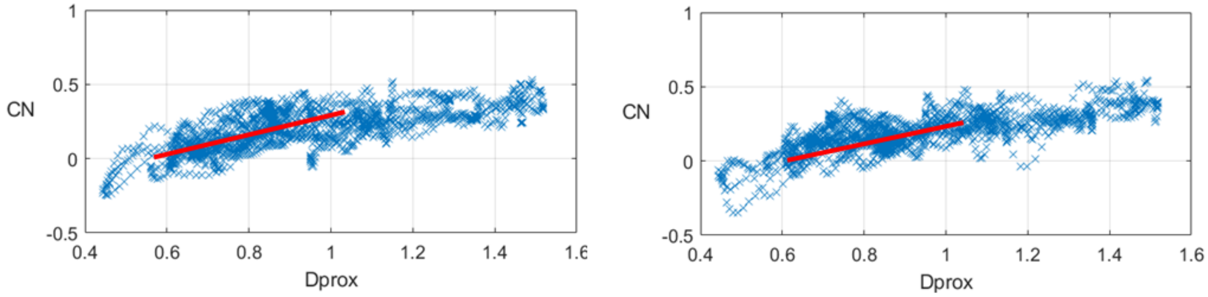

Figure 7.2.1-3. ***$(C_N)_{tot}$ from CDT 3-08 (parachute #1 (left), parachute #2 (right))***

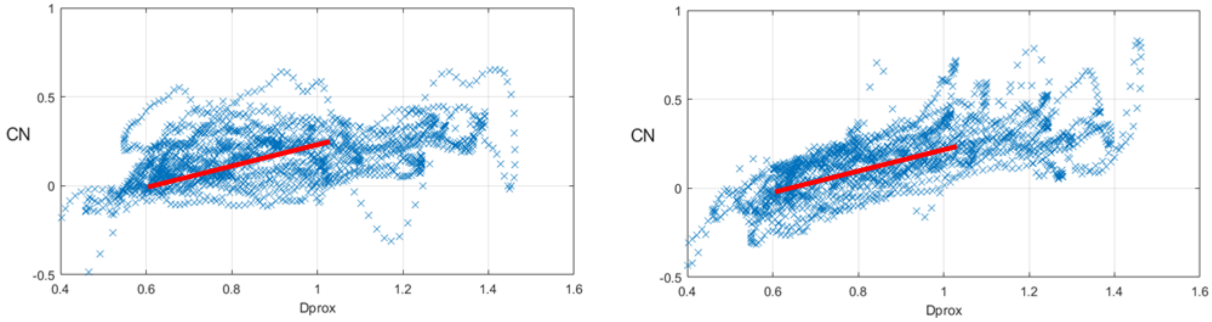

Figure 7.2.1-4. ***$(C_N)_{tot}$ from CDT 3-11 (parachute #1 (left), parachute #2 (right))***

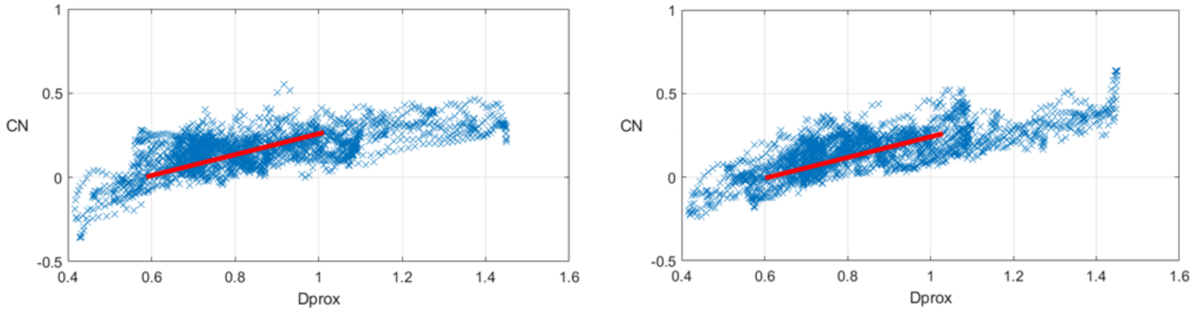

Figure 7.2.1-5. $(C_N)_{tot}$ from CDT 3-12 (parachute #1 (left), parachute #2 (right))

7.2.2 Maypole Mode

According to reference 2, the CDT 3-02 flight exhibited one full period of the maypole motion, as illustrated in Figure 7.2.2-1. The motion is approximately circular in nature and lasted for about 35 seconds. The red and blue curves indicate the paths traced out by the parachutes relative to the capsule during the maypole motion.

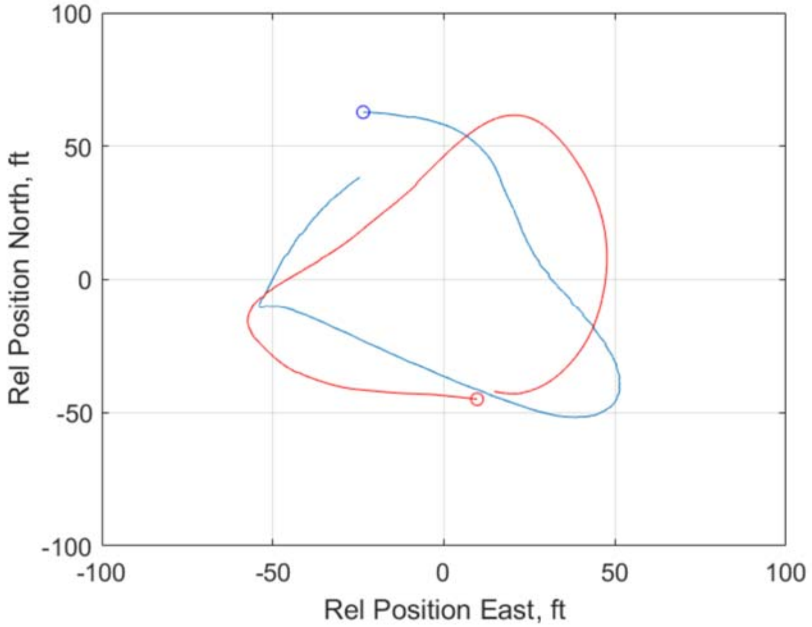

Figure 7.2.2-1. Maypole Motion from Flight Data

The analysis discussed in this section is based on the assumption that during the maypole motion the parachutes orbit around the vertical axis of symmetry in a perfect circle with a constant angular speed. To analyze the flight data, the line integrals of the paths traced out by the parachutes during the maypole motion were computed. This resulted in an equivalent circle with a radius of 50 ft or a constant flyout angle (or α_{trim}) of 0.21 rad. This is consistent with the observation from reference 12 that the interference aerodynamic forces cause the unstable parachutes to seek a trim angle of attack greater than the freestream trim α (0.19 rad shown in Table 7.1-2). Using Equation (6.2.2-22), $(C_N)_{\text{tot}}$ required to maintain the maypole motion is determined to be approximately 0.0485. As a verification, one can compute $(C_N)_{\text{tot}}$ using $(C_{N_\alpha})_{\text{tot}}$ (1.25 rad^{-1} from flyout analysis), α_{trim} (0.21 rad), and α_o (0.15 rad, from flyout analysis). This yields a $(C_N)_{\text{tot}}$ value of 0.072, which is in the ballpark with the 0.0485 value derived from maypole analysis alone. The pendulum analysis (proximity aero ignored) in Section 7.1 yields a C_{N_α} value of 0.19, which suggests that the scissors and maypole modes are dominated by proximity aerodynamics. For sustained Maypole motion, the aero (predominately proximity aero) balance out the centripetal acceleration of the parachutes causing them to circle the vertical axis at a constant flyout angle and angular velocity.

7.2.3 Breathing Mode

As described in Section 6.0, the breathing mode captures the physics in the coupling between oscillations in the parachute reference area (due to flexibility effects) with velocity in the Down direction. Figure 7.2.3-1 shows the best estimate parachute reference area and velocity in the Down direction from $T = 164$ to 234 seconds from the CDT 3-02 flight test. Figure 7.2.3-2 shows the fast Fourier transform (FFT) of the time domain data. It is apparent that the parachute reference area has a dominate peak at 0.23 Hz (period ~4.3 sec). V_{down} has two relatively large peaks below 0.1 Hz and a third peak at 0.23 Hz, which matches the dominate peak of the parachute reference area. Hence, there is an apparent coupling between S_{ref} and V_{down}. The slow oscillations (low frequency peaks below 0.1 Hz) in V_{down} are likely due to wind. The 0.23-Hz mode is present throughout the entire drop test and present in CDT 3-02, 3-11, and 3-12 as well.

Figure 7.2.3-3 shows the simulation results for the breathing mode with the system having a nominal V_{down} of approximately 34 feet per second (ft/s). ω_n is scaled such that the period of oscillation is around 4.5 seconds to match the flight data. $\eta = 0$ represents the nominal S_{proj}, while $\eta = \pm 1$ represents S_{proj} at its maximum and minimum derivations from the nominal. It is apparent that as η approaches 1, V_{down} approaches its minimum value of 32 ft/s, and as η approaches -1, V_{down} approaches its maximum value of 35.2 ft/s. Furthermore, η has a slight phase lead on V_{down}, as would be expected.

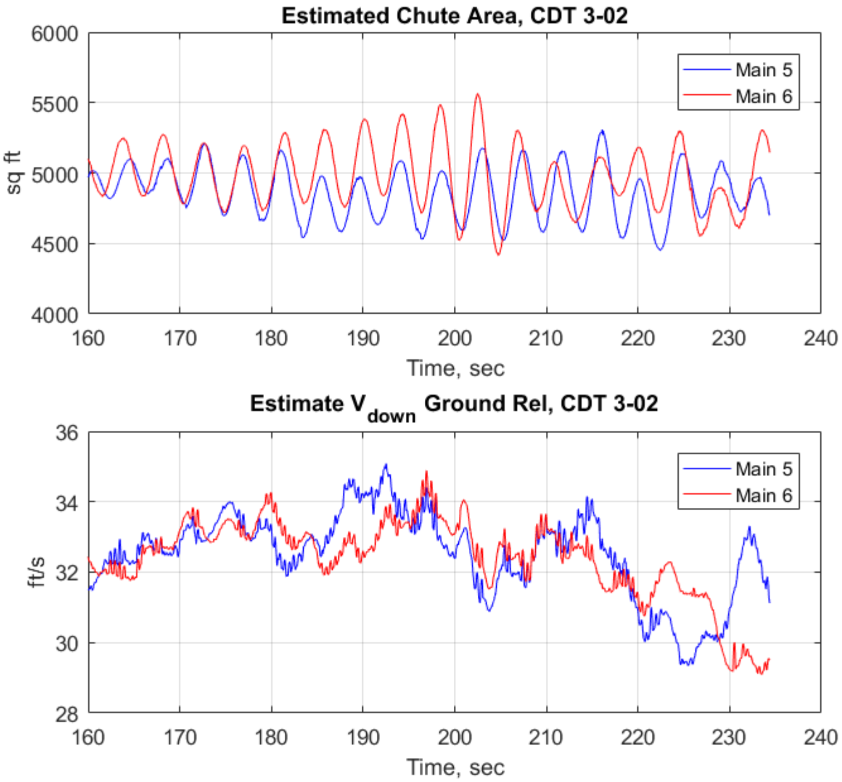

Figure 7.2.3-1. CDT 3-02 Best Estimate S_{ref} and V_{down} (T=160 to 234 sec)

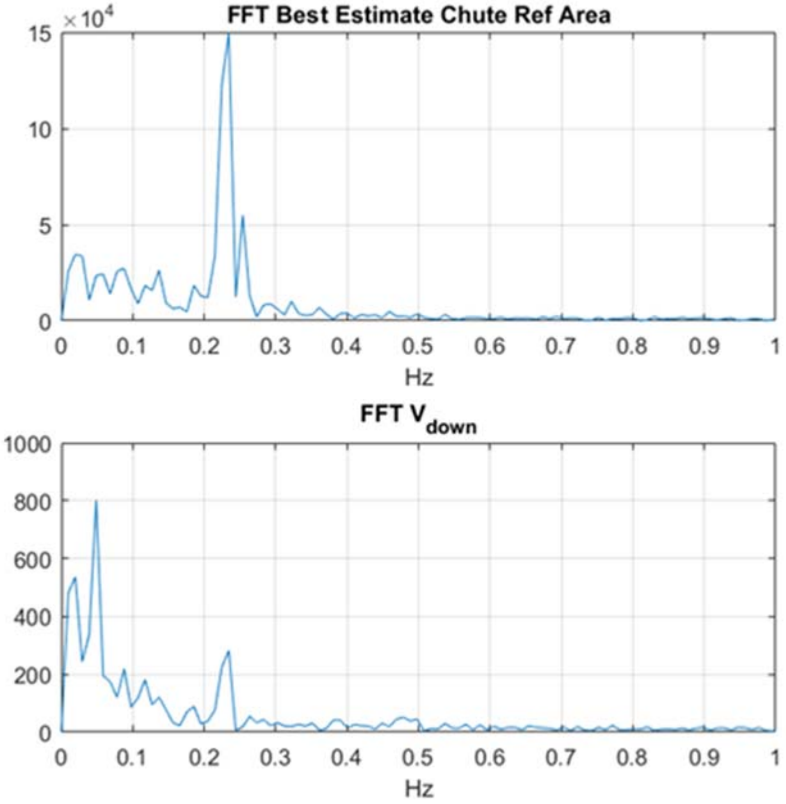

Figure 7.2.3-2. FFT CDT 3-02 Best Estimate S_{ref} and V_{down}

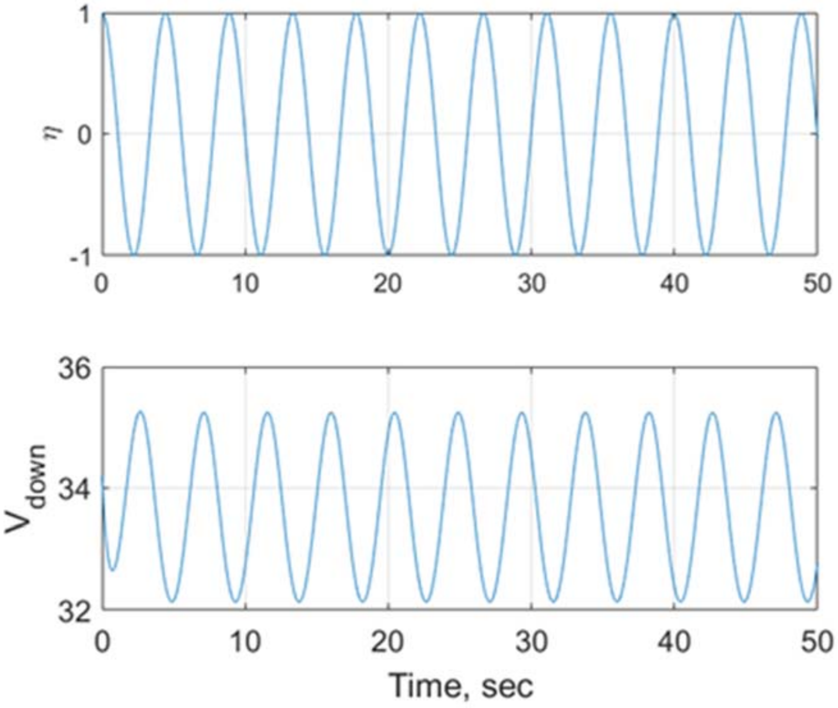

Figure 7.2.3-3. Breathing Mode Simulation Results

7.3 Equation-Error Aerodynamic Modeling Results

The first step in global modeling of the CPAS drop test flight data was the application of the equation-error method. Flight test results obtained using the equation-error approach are presented in this section, along with prediction results using flight data that were not used to identify the models.

Five flight tests applicable to this work were conducted with the CPAS configuration consisting of two main parachutes and a payload. Two other CPAS drop tests were conducted with two main parachutes, but they were not applicable because they utilized a modified main parachute configuration. Only the flight data for both main parachutes fully inflated were used for the analysis. The flight data from parachute 9 on flight test CDT-3-11 was selected for identifying the parachute aerodynamic models because that flight data had the most active dynamics for the longest period of time.

Figure 7.3-1 shows modeling results for C_A, C_Y, and C_N using CDT-3-11 flight data for parachute 9. The plots on the left side show the identified model fits to flight data from parachute 9 during the CDT-3-11 flight test, and the plots on the right show the residuals, which are the difference between the flight data and the identified model shown in the left plots for each nondimensional force coefficient.

The identified models clearly capture the main effects. The residual plots indicate small remaining deterministic components, but these components have amplitudes close to the noise levels for the flight data and, consequently, are difficult to identify. The SNR for the C_A data was much higher (SNR = 51) than for C_Y (SNR = 8) or C_N (SNR = 6). Lower SNR compromises the model identification, because there are smaller deterministic effects standing out above the noise, which makes it more difficult to identify what those deterministic effects are, based on the data.

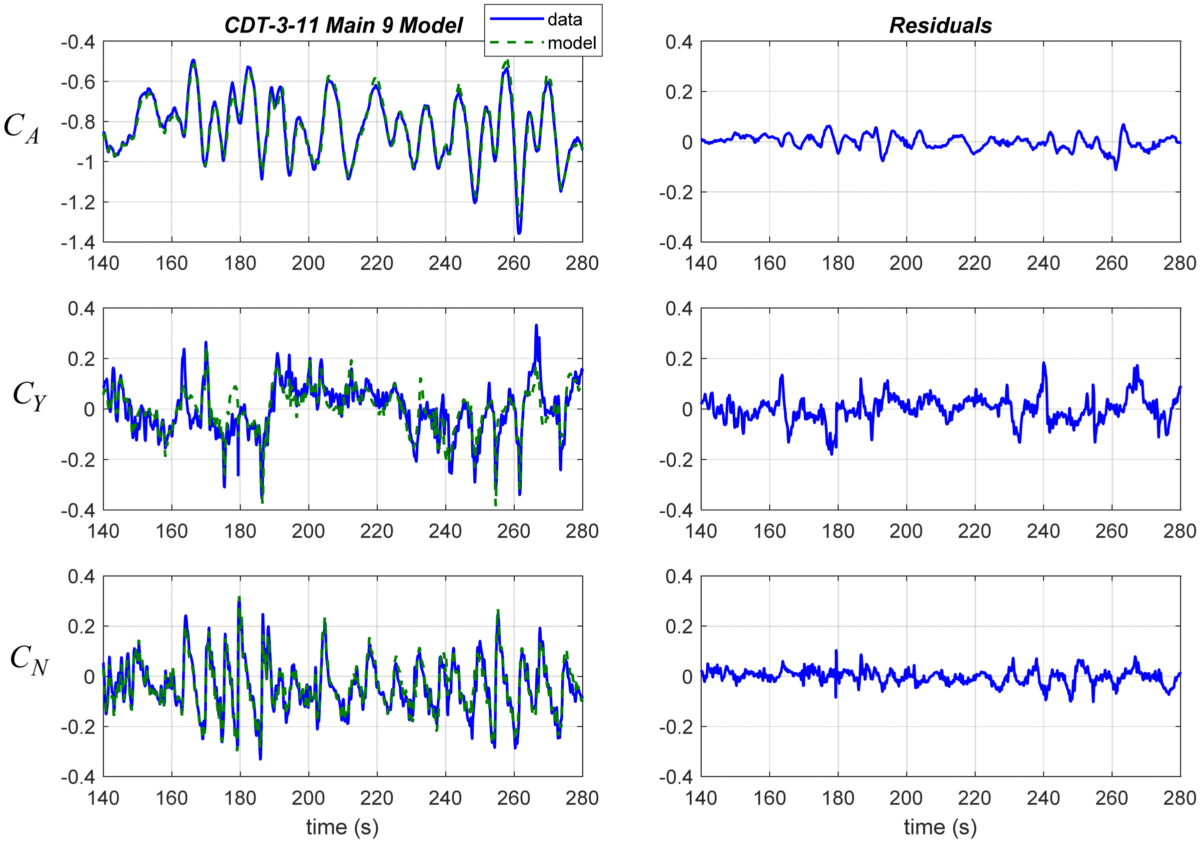

Figure 7.3-1. CPAS Equation-error Modeling, CDT-3-11, Main 9

Table 7.3-1 shows the identified model terms, with associated parameter values and uncertainties, based on CDT-3-11 flight data for the Main 9 parachute only. These model terms were selected from a postulated pool of candidate model terms, using orthogonalization and statistical modeling metrics, as described in Section 6.3.6. Each nondimensional aerodynamic force coefficient had its own pool of candidate model terms, assembled using measured explanatory variable data. All of the candidate modeling terms were polynomial terms of order 2 or less, along with spline terms.

The identified model can be impacted by which modeling terms are included in the pool of candidate modeling terms, along with the information content of the modeling data. Consequently, some investigation was conducted regarding the extent of the candidate modeling pool required. This was done by simply including many different and more complex modeling terms in the candidate pool, and allowing the algorithm to sort through all of them to find the terms with statistical significance for the model, based on the data alone. It was found that polynomial and spline terms with more complexity (higher order than 2) were not selected as statistically significant for inclusion in the model. This is not unusual for modeling problems using real physical data, and therefore the pool of candidate modeling terms included only polynomial terms of order 2 or less, along with spline terms. Note that this determination is based on the flight data available. It is possible that other flight data with more dynamic information content could produce different modeling results.

As an example, the C_A modeling used a pool of candidate modeling terms composed of every possible polynomial combination, up to second order, of the following 14 explanatory variables:

$$\begin{aligned}&\left(\frac{V}{V_o}-1\right),\ \alpha_T,\ \frac{\dot{\alpha}_T l_{ref}}{2V},\ \bar{q},\ D_{prox},\ V_{prox},\\ &\left(1.0-D_{prox}\right)_+^1,\ \left(1.1-D_{prox}\right)_+^1,\ \left(1.2-D_{prox}\right)_+^1,\\ &\left(1.3-D_{prox}\right)_+^1,\ \left(1.4-D_{prox}\right)_+^1,\\ &\left(\alpha_T-16\right)_+^1,\ \left(\alpha_T-20\right)_+^1,\ \left(\alpha_T-24\right)_+^1,\end{aligned} \tag{7.3-1}$$

where the spline notation is defined by

$$\left(\alpha_T-20\right)_+^1=\begin{cases}\left(\alpha_T-20\right) & \text{for } \alpha_T>20\\ 0 & \text{for } \alpha_T\le 20\end{cases} \tag{7.3-2}$$

and similarly for the other spline functions.

The model structure determination algorithm (`mof.m` from SIDPAC) assembled the candidate modeling functions (120 of them in this case), then orthogonalized these candidate modeling functions and ranked them as follows (showing only the top 20 most effective modeling functions output by `mof.m`):

```
o.f. #    index     sqrt(mse)        dmse       perr     R2        pe         n       F
-----     -----     ---------        ----       ----     --        --         -       -

  1           0     1.503e-01     -6.952e-01   17.74     0.00    1.508e-01    1    152.75

  2        1000     4.249e-02     -2.079e-02    5.01    92.01    4.590e-02    2      4.57

  3           2     2.590e-02     -1.134e-03    3.06    97.03    3.352e-02    3      0.25

  4  10010000000000 2.344e-02     -1.213e-04    2.77    97.57    3.396e-02    4      0.03

  5  100000100000   2.180e-02     -7.414e-05    2.57    97.90    3.507e-02    5      0.02

  6       10100     2.078e-02     -4.344e-05    2.45    98.09    3.658e-02    6      0.01

  7         200     2.016e-02     -2.549e-05    2.38    98.20    3.825e-02    7      0.01

  8       10001     1.984e-02     -1.258e-05    2.34    98.26    4.002e-02    8      0.00

  9     2000000     1.902e-02     -3.197e-05    2.25    98.40    4.148e-02    9      0.01

 10  100000000100   1.867e-02     -1.302e-05    2.20    98.46    4.311e-02   10      0.00

 11         101     1.823e-02     -1.624e-05    2.15    98.53    4.465e-02   11      0.00

 12     1100000     1.810e-02     -4.938e-06    2.14    98.55    4.625e-02   12      0.00

 13  10000000100000 1.792e-02     -6.592e-06    2.11    98.58    4.779e-02   13      0.00

 14  1010000000000  1.780e-02     -4.308e-06    2.10    98.60    4.930e-02   14      0.00

 15     1010000     1.768e-02     -3.916e-06    2.09    98.62    5.077e-02   15      0.00

 16  1000000000001  1.759e-02     -3.486e-06    2.08    98.63    5.220e-02   16      0.00

 17  10000000000001 1.737e-02     -7.685e-06    2.05    98.67    5.356e-02   17      0.00

 18  1000000010000  1.728e-02     -2.829e-06    2.04    98.68    5.492e-02   18      0.00

 19          11     1.723e-02     -1.958e-06    2.03    98.69    5.626e-02   19      0.00

 20          20     1.713e-02     -3.321e-06    2.02    98.70    5.756e-02   20      0.00
```

Minimum PSE occurs at the third ranked orthogonal function (see column marked `pe`, which contains the positive square root of the PSE metric), so the first three functions were included in the model, then transformed back to ordinary functions with their associated estimated parameters, as listed in Table 7.3-1. Note that the R2 metric indicates that the model has captured 97 percent of the total variation in the C_A data, using only three orthogonal functions identified from the pool of candidate model terms. The column marked `dmse` shows the reduction in mean squared model fit error with the addition of each orthogonalized candidate modeling function. Note that the ordering of the functions is defined by this quantity, which therefore decreases in magnitude (but is always negative), moving down the rows. The PSE metric selects the first three orthogonal functions as those that reduce the mean squared fit error by an amount significantly greater than the observed noise level for the measured output data, which is the C_A data in this case. The column marked F is the F-ratio, a statistical metric that is large positive for significant functions to include in the model, the column marked `perr` is the percent fit error, and the column marked `index` shows an index that identifies each particular function. A completely analogous process was used to identify the models for C_Y and C_N, with the results given in Table 7.3-1.

The following equations specify the model structure for the parameter values and uncertainties given in Table 7.3-1:

$$C_A = C_{A_o} + C_{A_{\bar{q}}}\bar{q} + C_{A_{V^2}}\left(\frac{V}{V_o} - 1\right)^2 \tag{7.3-2}$$

$$\begin{aligned} C_Y = {} & C_{Y_{\dot{\phi}_a}} \frac{\dot{\phi}_a l}{2V} \sin(\alpha_T) + C_{Y_{\dot{\phi}_a \bar{q}}} \frac{\dot{\phi}_a l}{2V} \sin(\alpha_T)\bar{q} + C_{Y_{D_{prox}}} D_{prox} \sin(\phi_{prox}) \\ & + C_{Y_{D_{prox0.8}}} \left(0.8 - D_{prox}\right)_+^1 \sin(\phi_{prox}) + C_{Y_{\dot{\phi}_a D_{prox}}} \frac{\dot{\phi}_a l}{2V} \sin(\alpha_T) D_{prox} \\ & + C_{Y_{\dot{\alpha}_T}} \frac{\dot{\alpha}_T l}{2V_o} \sin(\phi_{prox}) \end{aligned} \tag{7.3-3}$$

$$C_N = C_{N_{\dot{\alpha}_T}} \frac{\dot{\alpha}_T l}{2V_o} + C_{N_{\alpha_T}} \alpha_T + C_{N_{D_{prox0.8}}} \left(0.8 - D_{prox}\right)_+^1 \cos(\phi_{prox}) \tag{7.3-4}$$

where

$$\left(0.8 - D_{prox}\right)_+^1 = \begin{cases} \left(0.8 - D_{prox}\right) & \text{for } \left(0.8 - D_{prox}\right) > 0 \\ 0 & \text{otherwise} \end{cases} \tag{7.3-5}$$

Table 7.3-1. Equation-error Aerodynamic Modeling Results based on CDT-3-11 Main 9 Flight Data

	Model Term	Parameter Estimate (Standard Error)
C_A	1	-1.9577 (0.0077)
	$\bar{q}$	0.9297 (0.0068)
	$\left(\frac{V}{V_o}-1\right)^2$	-2.2803 (0.0452)
C_Y	$\frac{\dot{\phi}_a l_{ref}}{2V}\sin(\alpha_T)$	0.2007 (0.0280)
	$\frac{\dot{\phi}_a l_{ref}}{2V}\sin(\alpha_T)\bar{q}$	-0.2544 (0.0170)
	$D_{prox}\sin(\phi_{prox})$	-0.0382 (0.0024)
	$(0.8-D_{prox})_+^1\sin(\phi_{prox})$	0.5407 (0.0255)
	$\frac{\dot{\phi}_a l_{ref}}{2V}\sin(\alpha_T)D_{prox}$	0.3701 (0.0198)
	$\frac{\dot{\alpha}_T l_{ref}}{2V}\sin(\phi_{prox})$	-0.0834 (0.0080)
C_N	$\frac{\dot{\alpha}_T l_{ref}}{2V}$	0.3630 (0.0032)
	α_T	-0.0964 (0.0017)
	$(0.8-D_{prox})_+^1\cos(\phi_{prox})$	0.1030 (0.0123)

Figures 7.3-2 through 7.3-4 show prediction tests for the identified aerodynamic model using a presentation similar to that used in Figure 7.3-1. Only the flight data shown in Figure 7.3-1 was used to identify the aerodynamic model. The flight data in Figures 7.3-2 through 7.3-4 was used only for prediction testing. The model identified from flight data for parachute 9 on flight test CDT-3-11 (Figure 7.3-1) was used to predict the aerodynamics for parachute 8 on flight test CDT-3-11 (Figure 7.3-2), parachute 14 on flight test CDT-3-12 (Figure 7.3-3), and parachute 3 on flight test CDT-3-8 (Figure 7.3-4). In each prediction case, explanatory variable data from the prediction test were used with the identified model to predict the nondimensional force coefficient data.

Although the aerodynamic model was identified from flight data for only one parachute during one flight test, the prediction plots in Figures 7.3-2 through 7.3-4 demonstrate that the identified model had good prediction capability for flight data not used in the modeling. The prediction quality and residual magnitudes in Figures 7.3-2 through 7.3-4 are comparable to those shown in the model identification plots of Figure 7.3-1, which is a strong indicator of a good model. Note that this does not mean the identified model is perfect, which it clearly is not, but rather that the model fit quality and the prediction quality are similar. This means the fit to the data is approximately the same for both the data used to identify the model and for data that were not used in any way to identify the model. Furthermore, as discussed earlier, only dynamic characteristics with magnitude at least three times larger than the noise level and clearly correlated with orthogonalized candidate model terms can be reliably modeled. The prediction case shown Figure 7.3-2 is for the other parachute in the CDT-3-11 flight test, whereas the prediction cases shown in Figures 7.3-3 and 7.3-4 are for parachutes in other flight tests, conducted on different days. Prediction cases for all parachutes from all five flight tests exhibited similar good prediction capability, with comparable residual magnitudes.

Note that in the equation-error method, it is possible to combine data from different parachutes and different flight tests by simply stacking the data and conducting the analysis normally, because the equation-error approach uses regression and linear algebra. This approach was investigated with various combinations of flight data from different parachutes and flight tests, but it was found that the flight data from parachute 9 on flight test CDT-3-11 had sufficient data information content to identify aerodynamic models with good prediction capability. Using flight data from other parachutes on flight tests CDT-3-11 and CDT-3-12, or combined flight data for the parachutes on these flights resulted in similar identified model structures and model parameter estimates. This is supported by the fact that the models identified from the flight data for parachute 9 on flight test CDT-3-11 exhibited good prediction capability for all other parachutes and flight tests, as shown in Figures 7.3-2 through 7.3-4. Flight tests CDT-3-2, CDT-3-8, and CDT-3-15 had insufficient dynamic information for good model identification (low SNR), so the flight data from those tests were used only for prediction testing. The prediction capability for models identified from parachute 9 on flight test CDT-3-11 was equally good for all parachutes on all five flight tests, regardless of the dynamic information content in the flight data or the dynamic modal responses exhibited.

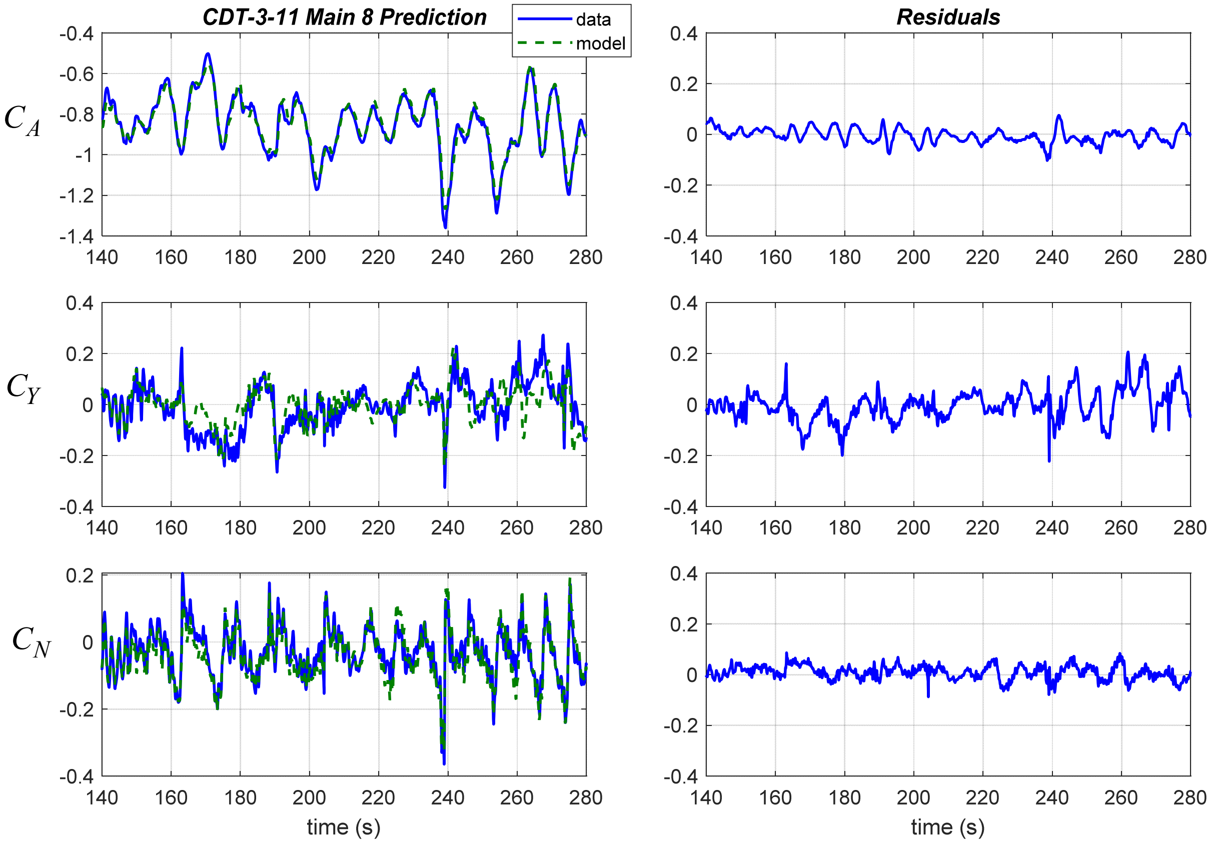

Figure 7.3-2. CPAS Equation-error Model Prediction, CDT-3-11, Main 8

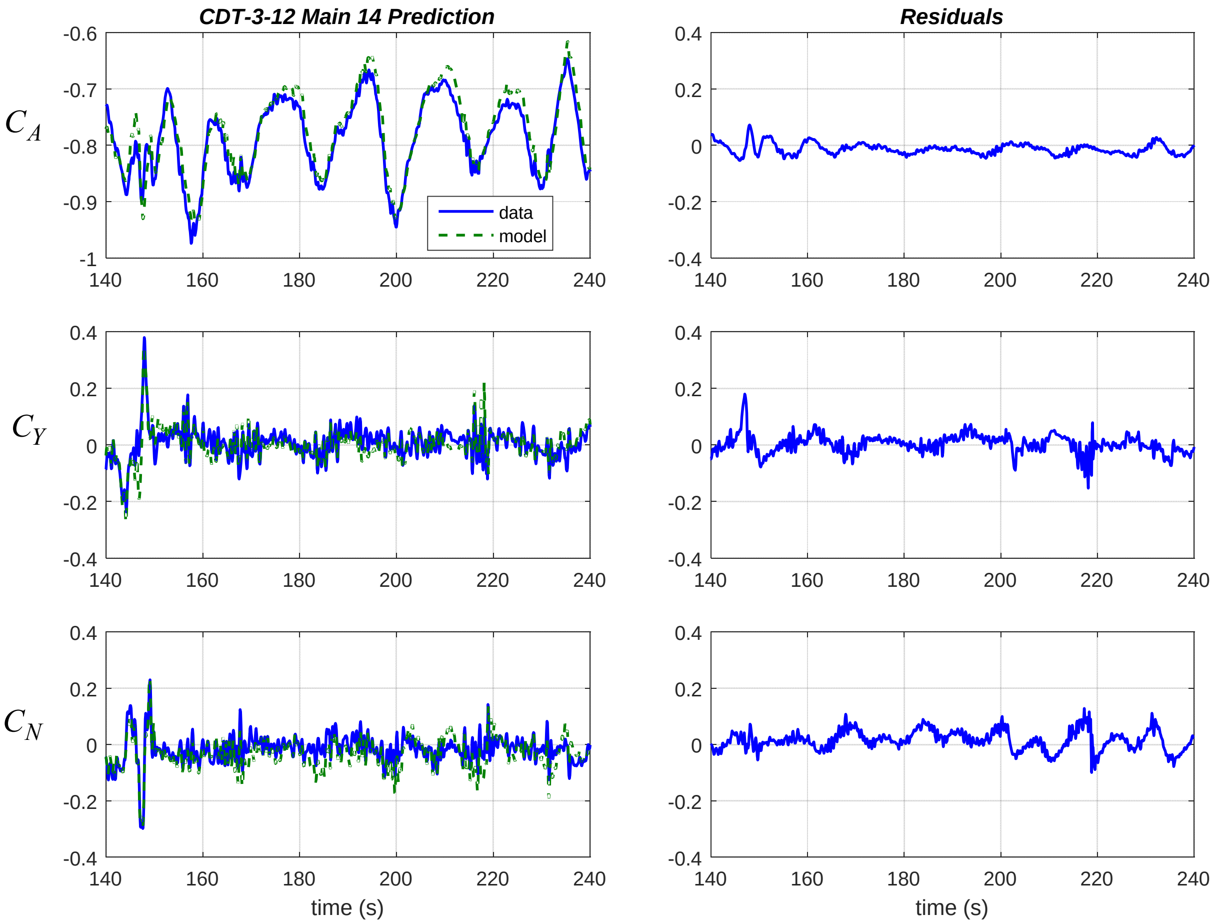

Figure 7.3-3. CPAS Equation-error Model Prediction, CDT-3-12, Main 14

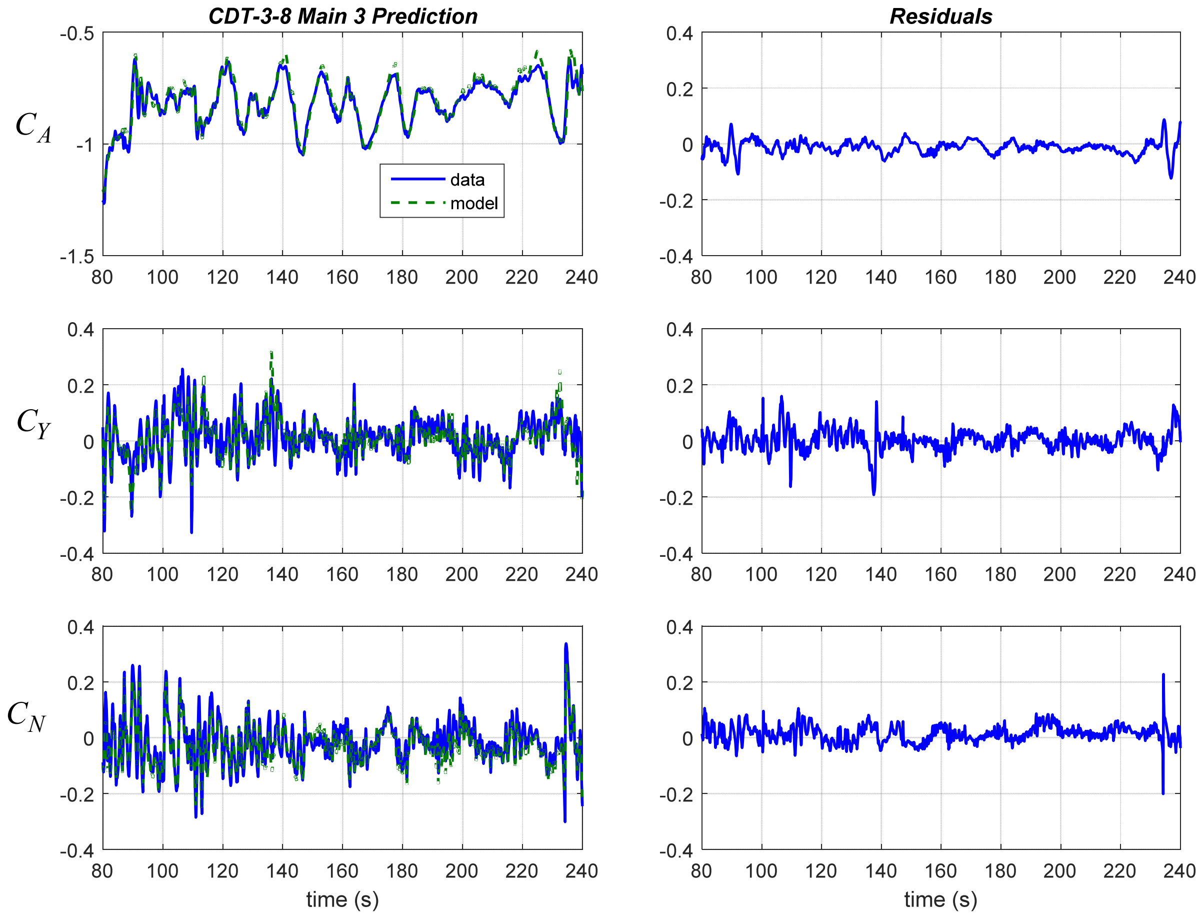

Figure 7.3-4. CPAS Equation-error Model Prediction, CDT-3-8, Main 3

7.4 Output-Error Aerodynamic Modeling Results

The next step in global modeling of the CPAS drop test flight data was the application of the output-error method. Output-error analysis is typically done using the aerodynamic model structure identified from equation-error analysis, as described previously, and using the equation-error model parameter estimates for the identified model structure as starting values for the output-error analysis. This process has been used successfully in the past on many different aircraft and flight test programs [ref. 15].

The parachute aerodynamic modeling problem differs from past applications in important ways, the most significant of which is that the dynamic system is a three-body cluster composed of two parachutes and the capsule payload with elastic connections between the parachutes and the capsule payload, rather than a single aircraft. This made the problem challenging in ways that were not anticipated at the initiation of the study. The main challenges encountered in the output-error analysis for parachute aerodynamic modeling in a three-body parachute cluster were:

- From prior work documented in the literature and wind tunnel testing, parachutes are known to have a strong restoring aerodynamic normal force at high values of total angle of attack. Because the flight tests were passive tests (not actively controlled over a desired range of angle of attack), the flight data included very few data points at high total angle of attack, which meant that the strong restoring force at high total angle of attack was not identifiable from the flight data. This was not a factor for equation-error modeling, which does not involve integrating the equations of motion. However, this issue was important for output-error modeling because without that strong restoring aerodynamic force, the integration of the equations of motion in the nonlinear simulation diverged quickly using models identified using equation error, which did not identify the strong aerodynamic restoring force at high total angle of attack. This required introducing a term for the strong restoring normal force at high total angle of attack in the aerodynamic model used for output-error analysis to prevent divergence during the output-error optimization. The added term was a stabilizing quadratic spline term at high total angle of attack, added to the C_N model,

$$C_{N_{\alpha_{T_{35}}}} \left(\alpha_T - 35\right)_+^2 = \begin{cases} C_{N_{\alpha_{T_{35}}}} \left(\alpha_T - 35\right)^2 & \text{for } \alpha_T > 35 \\ 0 & \text{for } \alpha_T \le 35 \end{cases} \tag{7.4-1}$$

- This model term was suggested by parachute aerodynamic modeling results found in the literature (e.g., reference 10). The value of the $C_{N_{\alpha_{T_{35}}}}$ parameter for this model term was chosen by engineering judgment, to avoid divergence in the simulation runs required for output-error optimization. Subsequent efforts to estimate the value of this parameter value using output-error parameter estimation were unsuccessful. Aerodynamic models identified using multivariate orthogonal functions included angular rate terms, including total angle of attack rate and aerodynamic azimuth angle rate. When these terms are included in a nonlinear simulation, there are difficulties associated with initializing the quantities to match flight data and with computing these values accurately and without time lag inside the nonlinear simulation. Essentially, real-time derivatives had to be computed in the nonlinear simulation based only on the past values of the quantity being differentiated (e.g., total angle of attack). This resulted in reduced accuracy and time lag, which were both detrimental to output-error modeling accuracy. Note that the equation-error approach did not have this problem because the explanatory variables, including total angle of attack and aerodynamic azimuth angle time derivatives, were computed directly from the entire flight data record for the equation-error analysis; therefore, these quantities had neither the reduced accuracy nor the time lag problem.
- In the nonlinear simulation, the parachute z-axis was always directed into the air-relative velocity vector to make the polarity associated with the aerodynamic model consistent. However, when the air-relative velocity vector was nearly parallel to the parachute x-axis directed along the line connecting the center of the parachute and the payload attachment point, there were rapid oscillations of the parachute axes orientation. This is a non-physical characteristic related to how the parachute axes were defined. To prevent these non-physical rapid oscillations, a deadband was implemented (similar to the FAST implementation) to freeze the parachute axes orientation for low values of the air-relative velocity component along the parachute z-axis. This was necessary because the parachute axes orientation affected the computation of the total angle of attack rate and the aerodynamic azimuth angle rate, which were used as explanatory variables in the aerodynamic model. Similarly, when the air-relative velocity vector passed from one side of the parachute axes x-y plane to another, the aerodynamic azimuth angle rate spiked to very high values for just a few time steps. This effect is also non-physical because the air-relative velocity vector does not rotate about the parachute x-axis rapidly, but rather passes nearby or through it on the way to the

other side of the parachute axes x-y plane. This effect was mitigated by freezing the aerodynamic azimuth angle rate inside the deadband for low values of total angle of attack.

- The two parachutes were connected to the capsule payload by elastic riser lines, which were modeled in the nonlinear simulation with a fixed spring constant and damping coefficient. For parachute cluster dynamic modeling, the line tension dynamics and interaction of the capsule payload and line tension forces with the parachute aerodynamics at the start of each simulation run dominated the dynamic motion computed by the nonlinear simulation. Consequently, it was necessary to use flight data from the capsule payload to estimate line tension forces and use that information in the nonlinear simulation so that the modeling problem could be focused on the parachute aerodynamics. When this was not done, the problem became a difficult nonlinear dynamics problem simultaneously involving the parachute aerodynamics and the line tension dynamics.
- When a dynamic system is inherently stable, output-error modeling is a simple and straightforward follow-on analysis, starting from the model structure and model parameter values computed in the equation-error analysis. However, the fact that equation-error modeling works regardless of the stability of the system can lull an analyst into assuming that the output-error solution will be simple and straightforward in the case of an unstable system. This generally is not true, as evidenced by this assessment, and this issue was a major source of unanticipated technical effort. The parachute aerodynamic modeling problem in this assessment could be called a brittle output-error optimization because there were stable and unstable terms in the C_N aerodynamic model identified using the equation-error method, which caused difficulty in the output-error optimization.

Figures 7.4-1 through 7.4-3 show the output-error fit to flight data from the CDT-3-11 flight test, using the CP2 nonlinear simulation and back-driving the equations of motion with measured flight acceleration data. Bias errors in the flight data for Earth-axes velocity were estimated and removed using output-error parameter estimation, in the manner described earlier. The existence of these biases was identified by noting a drift in the Earth axes positions produced by the CP2 nonlinear simulation when back-driving the equations of motion with measured flight acceleration data. The output-error parameter estimation for these bias parameters (i.e., one for each component of Earth axes velocity, for each parachute, for a total of six bias parameters) was straightforward and successful, as evidenced by the excellent match between the flight data and the CP2 nonlinear simulation outputs shown in Figures 7.4-1 through 7.4-3. This demonstrated that the CP2 nonlinear simulation was implemented properly and was a good mathematical representation of the CPAS parachute cluster dynamics.

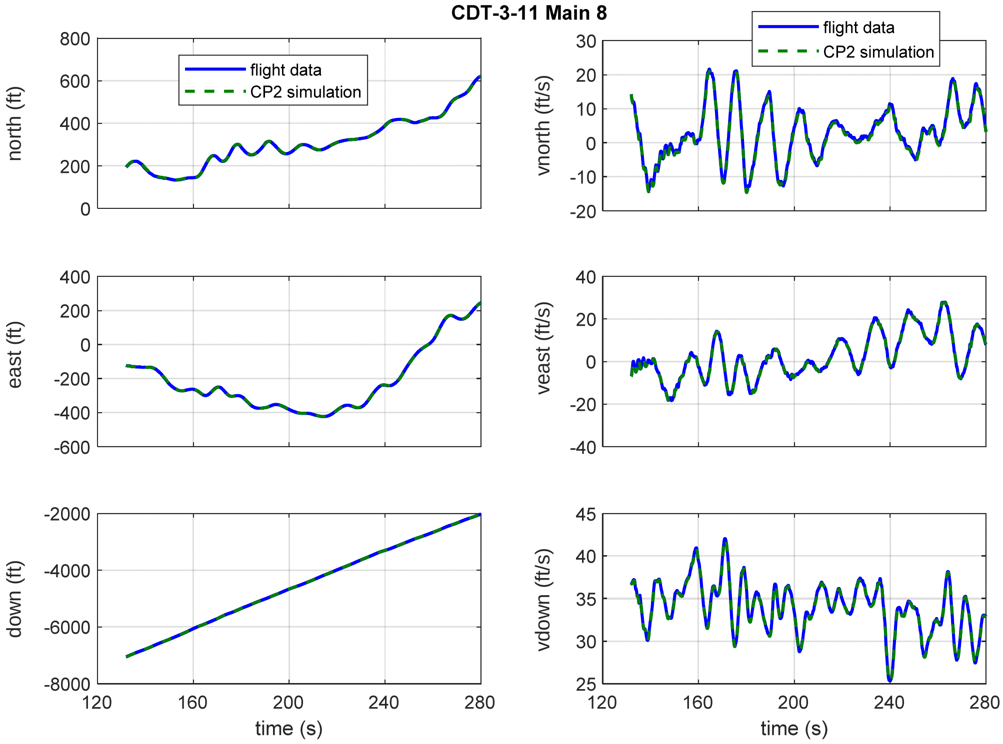

Figure 7.4-1. CP2 Back-driven with Flight Accelerations, CDT-3-11, Main 8

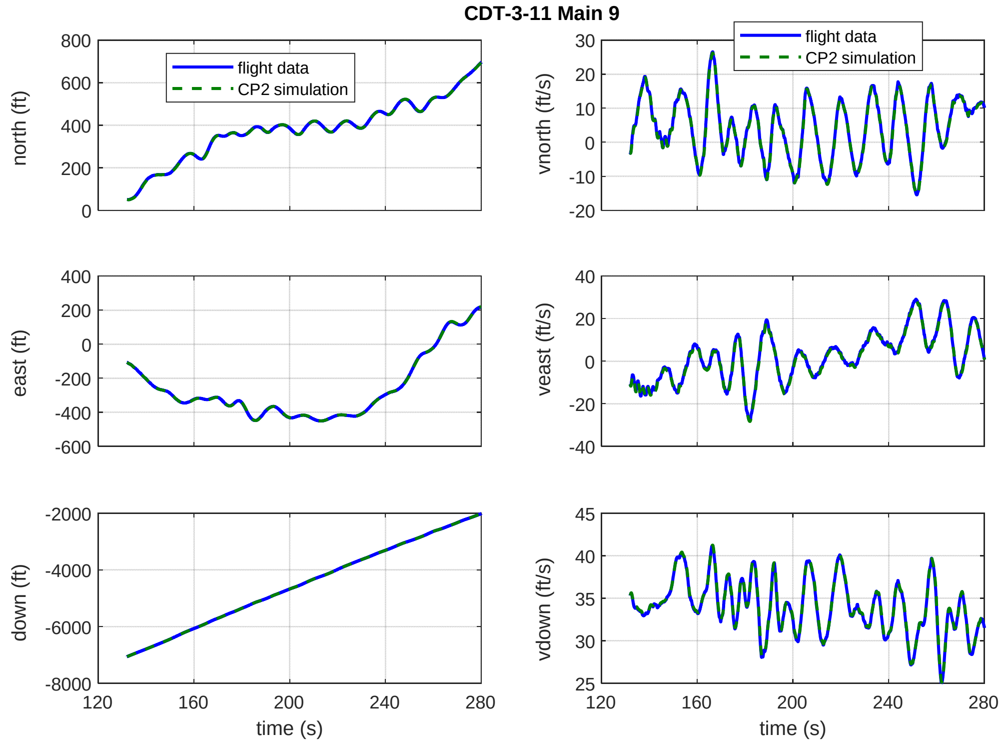

Figure 7.4-2. CP2 Back-driven with Flight Accelerations, CDT-3-11, Main 9

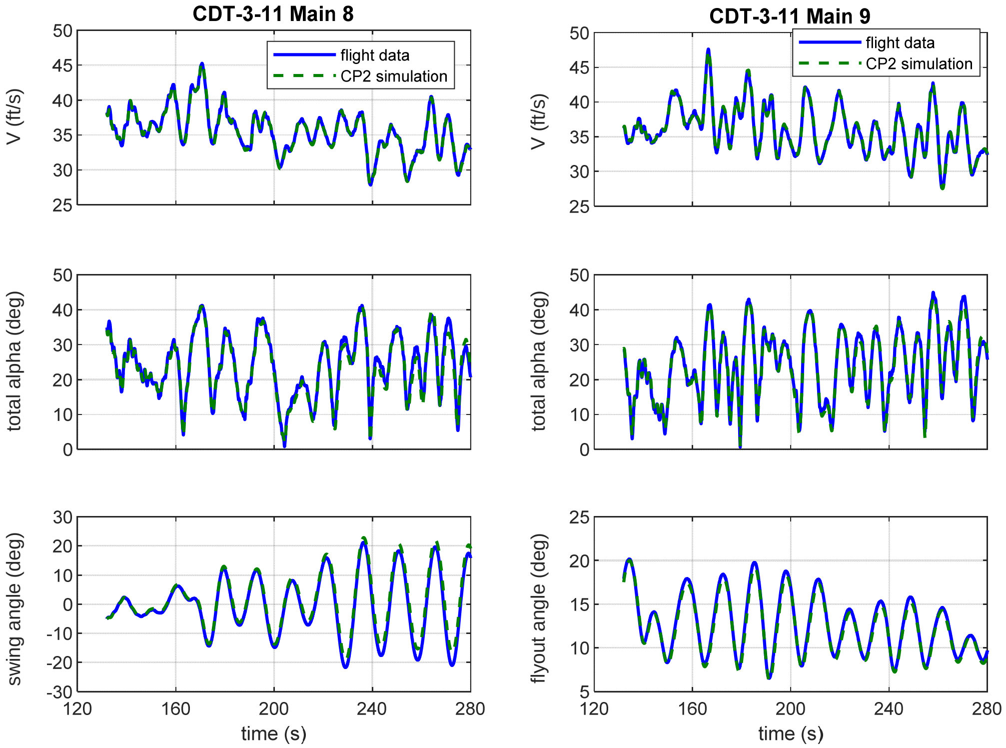

Figure 7.4-3. CP2 Back-driven with Flight Accelerations

For this CP2 simulation run, the nondimensional aerodynamic coefficients were computed from the CPAS flight data and using the identified equation-error model inside the CP2 nonlinear simulation. Figure 7.4-4 shows that the identified equation-error model was reasonably close to the nondimensional aerodynamic force coefficient data that resulted in the excellent output match shown in Figures 7.4-1 through 7.4-3.

The next step was to use the aerodynamic model identified using the equation-error method as the aerodynamic model inside the CP2 simulation, then adjust the parameters in that model structure to best fit the CP2 outputs to the CPAS flight data in a weighted least-squares sense. This is the output-error approach described earlier.

Aerodynamic model structures used for the output-error analysis were those identified from the flight data using the equation-error method, as described in Section 7.3 and listed in Table 7.3-1. The associated model parameter estimates obtained from applying the equation-error method were used as starting values for the output-error analysis.

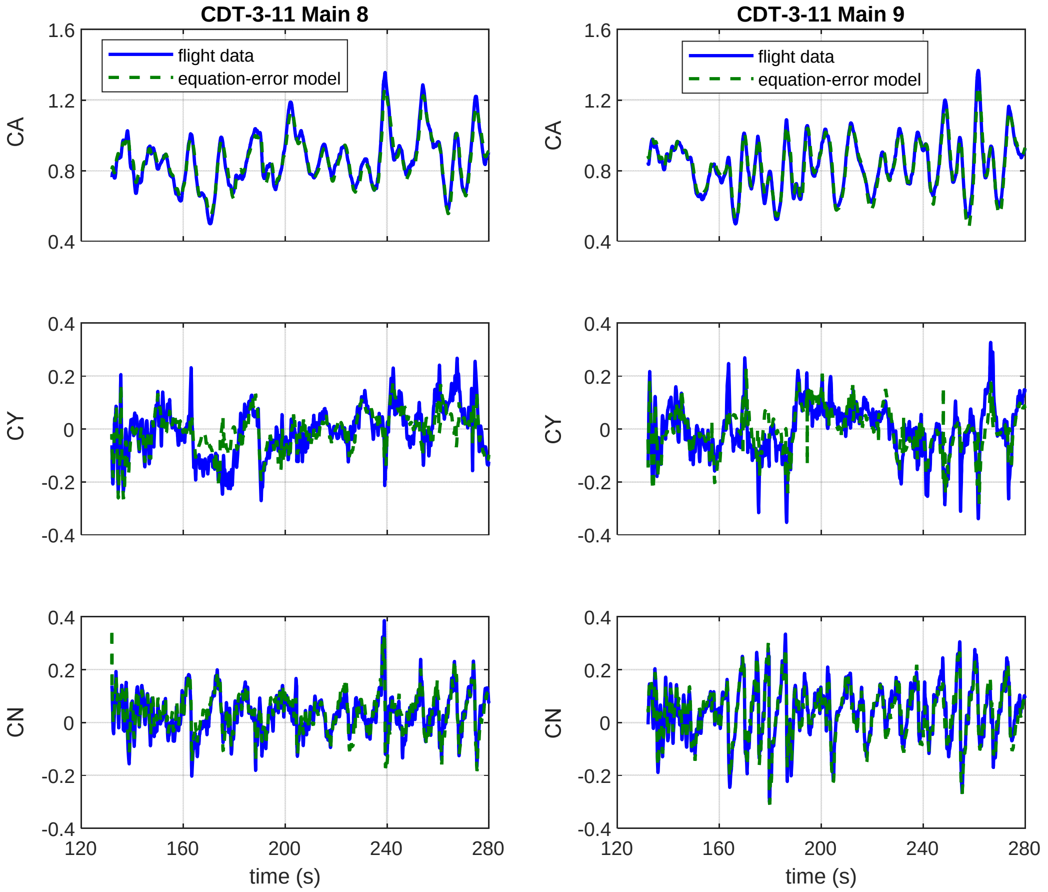

Figure 7.4-4. Nondimensional Aerodynamic Force Coefficient Comparison

Unfortunately, the output-error optimization problem turned out to be very difficult, mainly as a result of attempting to estimate both proximity effects and other aerodynamic effects simultaneously, in a problem that was highly sensitive to small changes in the model parameters and the orientation of the parachutes. This situation might be called a brittle optimization problem. Many variations were attempted to help the optimization converge, such as shortening the data record length, providing the aerodynamic model with measured explanatory variable data (as opposed to time-integrated explanatory data) inside the nonlinear simulation, optimizing model parameters for only one aerodynamic coefficient model at a time, changing the finite differencing method used to compute local output sensitivities to model parameter changes, and using a local exhaustive search rather than the conventional slope-based modified Newton-Raphson optimization technique. Ultimately, none of these approaches produced results that agreed well with the flight-test time histories.

7.5 Simulation Comparisons with Flight Data

7.5.1 Current Orion Model in FAST Simulation versus Flight

The current CPAS main parachute aerodynamic model is part of the MPCV aerodynamic database [ref. 22]. It models the aerodynamics for the full-open, steady-state portion of a one-main-out scenario. The effort to develop this model was spurred by the observation of unfavorable pendulum motion on the CDT-3-11 and CDT-3-12 full-scale drop tests. The model is intended to capture this pendulum motion to enable higher fidelity risk assessments and control algorithm development.

This aerodynamic model was developed through a highly manual process. The equations of the model were split into the three critical components of the aerodynamics: static, dynamic, and proximity effects. The general shape and dependencies of the static components were derived from historical data [refs. 10, 11, and 23]. The dynamic and proximity effects initially were not well understood, and the equations and the coefficient values were developed iteratively.

The model was defined using FAST through manual updates to the aerodynamic coefficients in the equations at each iteration. The key parameters of interest in this reconstruction process were, in order of importance: descent rate, swing angle, flyout angle, and overall orbiting behavior. If the model could match the gross descent rate, peak swing angle, approximate pendulum frequency, and approximate pendulum onset, it was considered a good model. The quality of the drop test data was not high enough to enable exact reconstructions of the trajectories over minutes of flight time. Additional detail about the initial development can be found in reference 24, and updates regarding more recent changes can be found in reference 25.

The current Orion model (v0.94-1) implemented in FAST is compared with the BET for CDT-3-12 in Figures 7.5.1-1 and 7.5.1-2. Note that simulation parameters used in FAST differ slightly from the parameters listed in Table 6.1.1 and used in system identification. The FAST simulations used a slightly larger enclosed mass scale factor, 0.75, in the axial direction and a slightly smaller payload-to-parachute nominal line length of 230 ft. Also, the system identification focused on CDT-3-11, which has a different payload mass than CDT-3-12 (20,340 lbm). The criteria given for an acceptable model have been met with good comparisons in both descent rate and swing angle. Similar trajectory reconstruction quality was also obtained for the four other one-main-out drop tests.

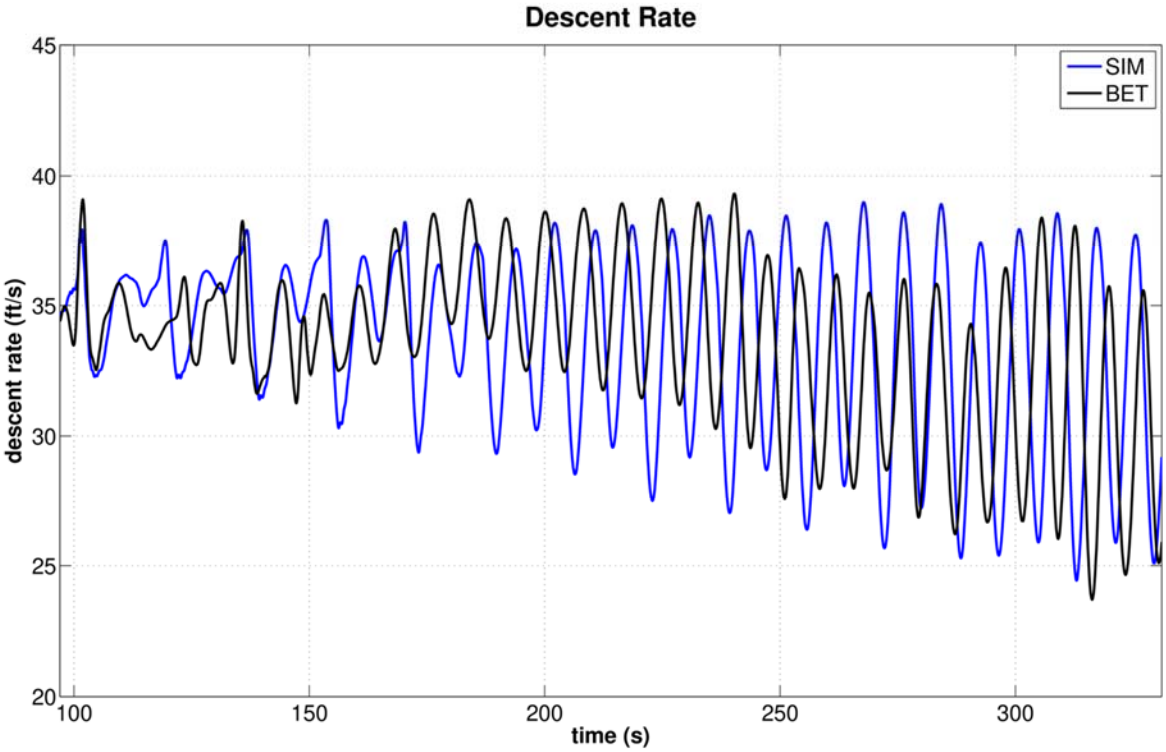

Figure 7.5.1-1. CDT-3-12 BET Sea-level Equivalent Descent Rate Comparison with Orion Model in FAST

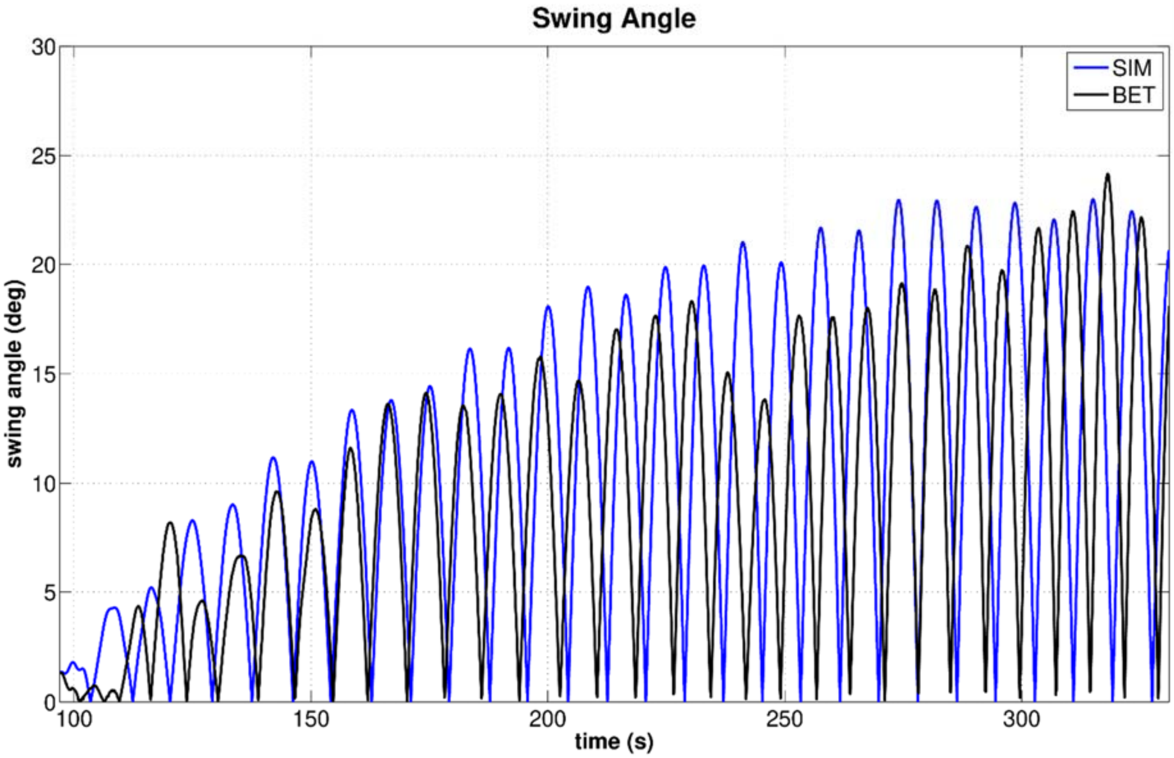

Figure 7.5.1-2. BET Swing-angle Comparison with Orion Model in FAST

7.5.2 System ID Model in CAPDYN Simulation versus Flight 3-11

The identified nonlinear aero model based on the simplified planar dynamics as described in Section 7.1 was implemented into CAPDYN to predict the pendulum motion portion of the 3-11 flight. The parachutes were assumed to be on top of one another due to the lack of proximity aerodynamics. Figure 7.5.2-1 shows the flight winds during the pendulum period of the 3-11 flight. Figure 7.5.2-2 compares the swing-angle time history from CAPDYN and flight. The discontinuities in the CAPDYN swing-angle time history are an artifact of the manner in which it is computed in CADPYN. Generally, the discontinuities appear when the swing angle crosses zero. Figures 7.5.2-3 through 7.5.2-5 compare the North, East, and Down air relative velocities of one of the parachutes. Figure 7.5.2-6 compares the North and East positions of the capsule. The system is translating toward the Northeast due to the winds while undergoing pendulum motion.

It is important to note that while CAPDYN with the simple aero model does a reasonable job of matching certain key outputs from flight during the pendulum motion, it does not match well with the rest of the flight or with flights with no pendulum motion (e.g., 3-02 and 3-08). This is inherently the limitation of the planar dynamics used to generate the simplified aero model. Furthermore, the simplified aero model cannot predict when the pendulum mode will occur. Based on observations of the four sets of flight data, it appears the pendulum motion triggers due to a combination of a sudden change in the wind direction while the magnitude exceeds a certain threshold. It is a highly complex and nonplanar event and is beyond the capability of the planar dynamics model.

As discussed previously, it was hoped that the system identification methods described in Sections 7.3 and 7.4 would have been successful in identifying a global nonlinear parachute model that would predict when the pendulum mode would occur and capture all the modes of motion.

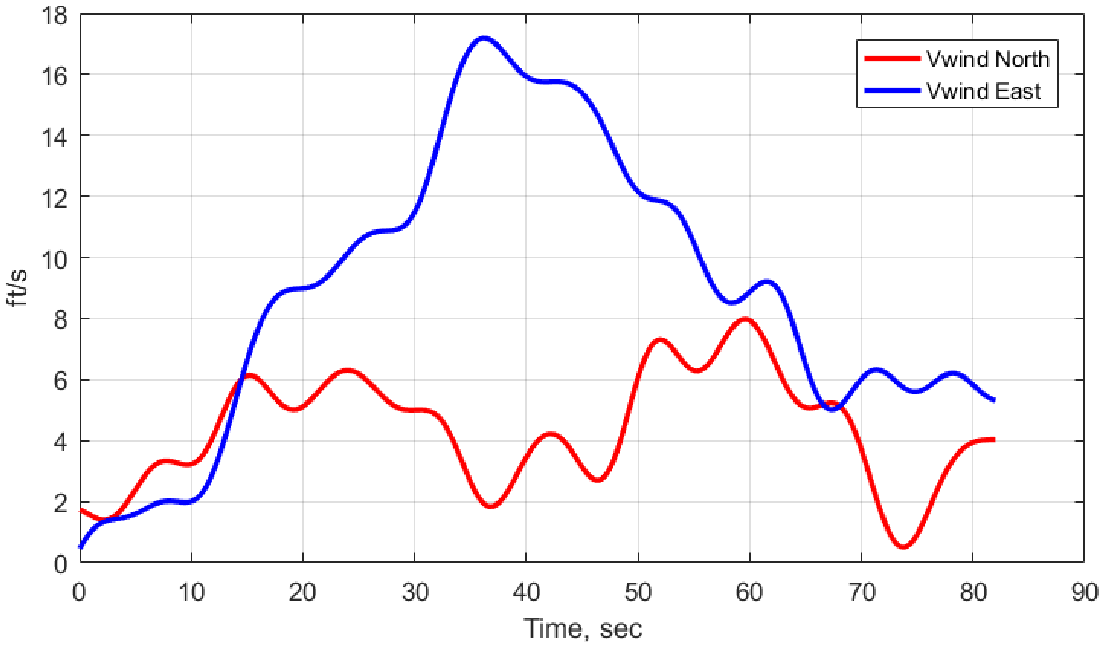

Figure 7.5.2-1. Flight Winds during Pendulum Motion 3-11

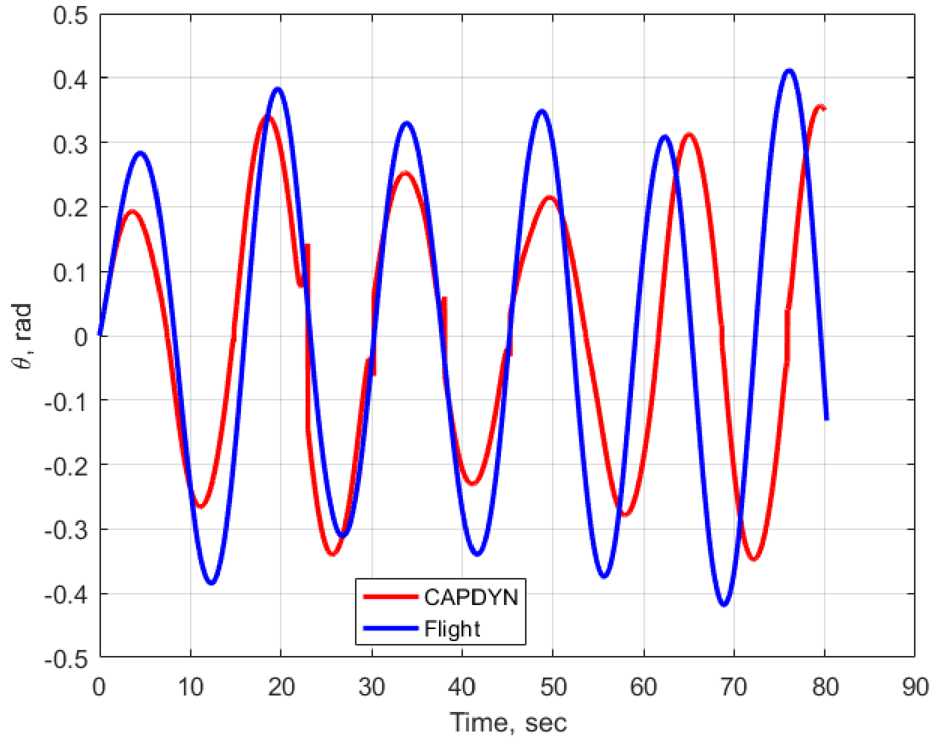

Figure 7.5.2-2. Swing Angle

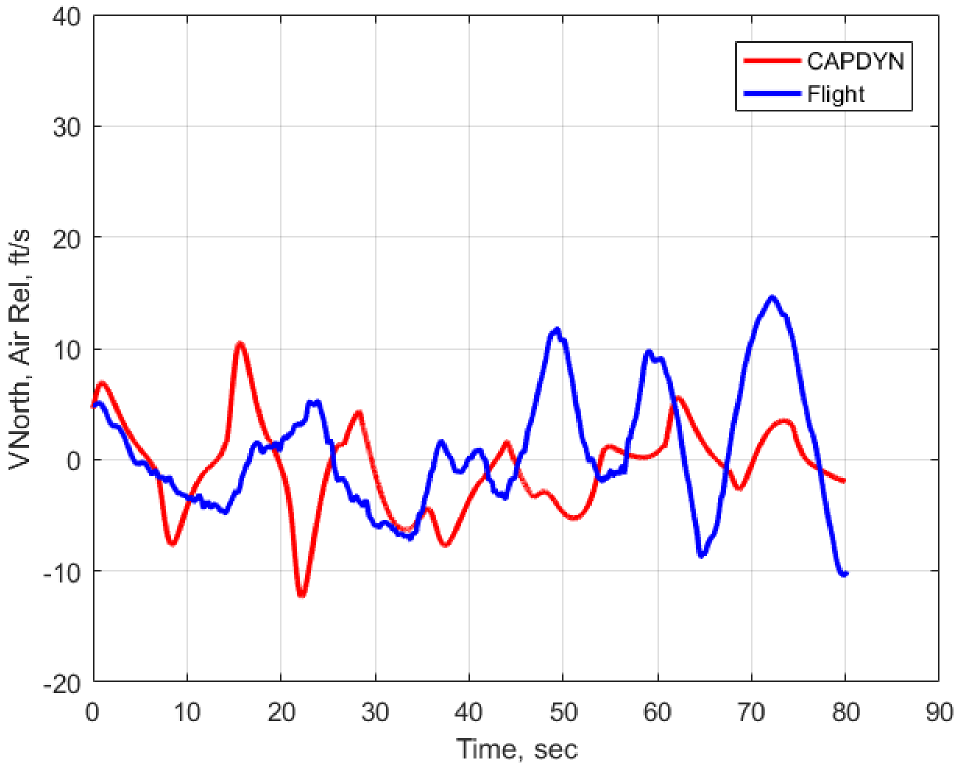

Figure 7.5.2-3. Parachute Air Relative Velocity North

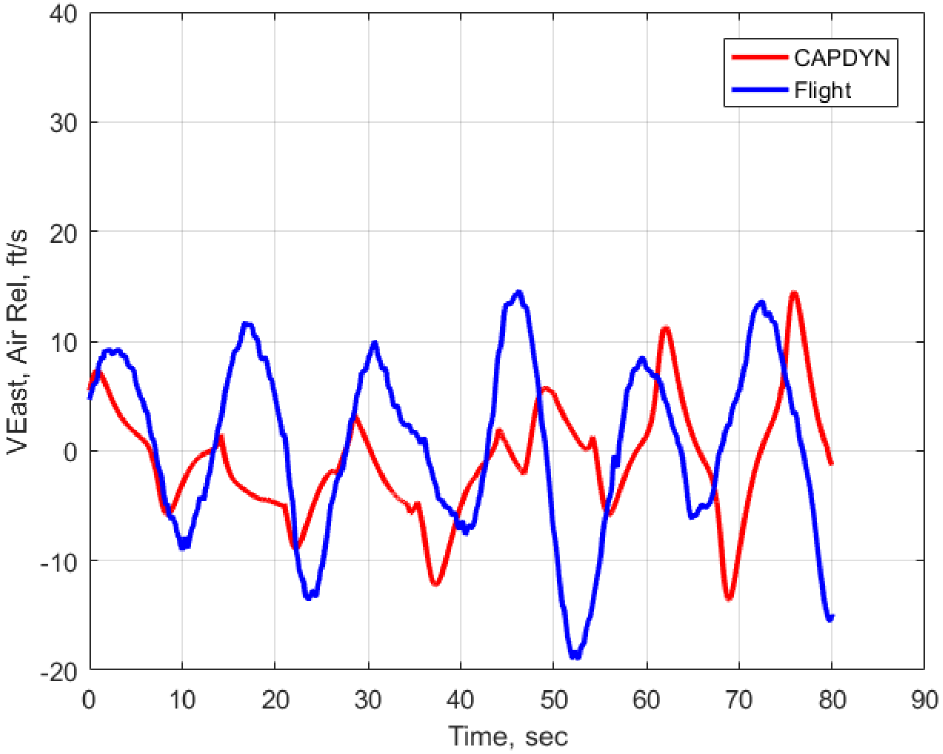

Figure 7.5.2-4. Parachute Air Relative Velocity East

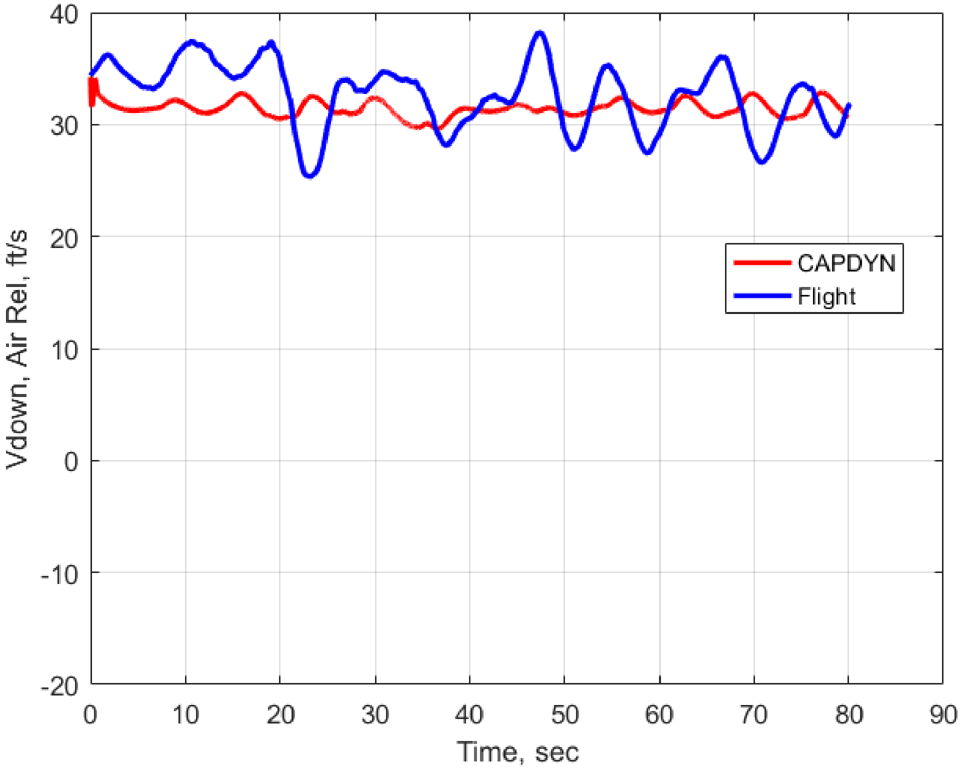

Figure 7.5.2-5. Parachute Air Relative Velocity Down

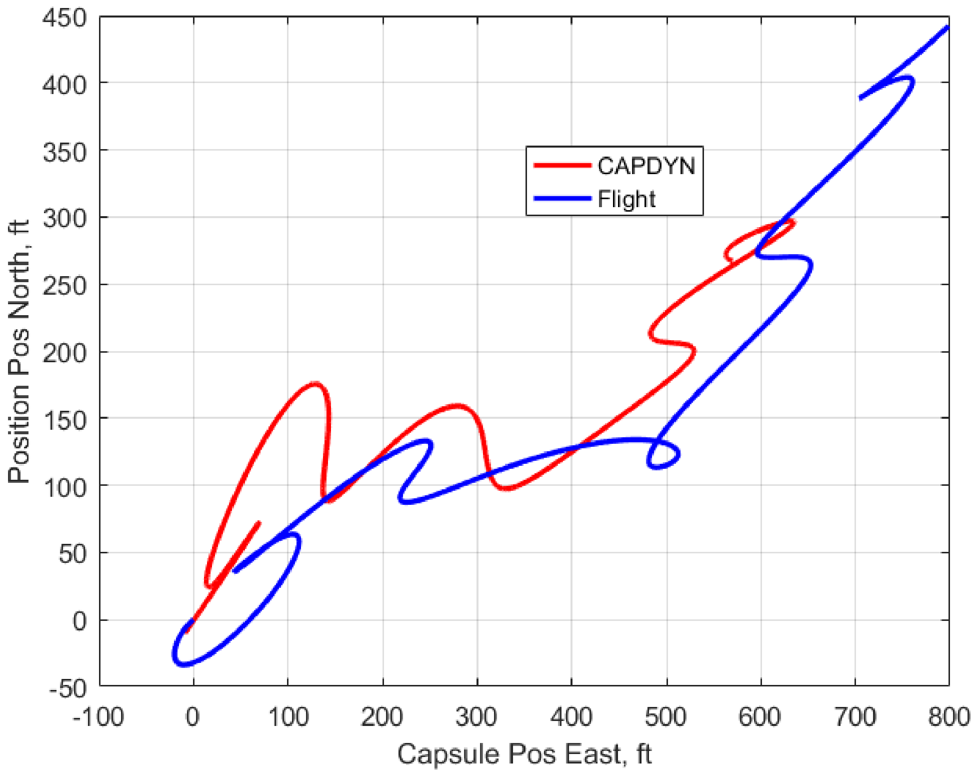

Figure 7.5.2-6. Capsule North East Position

8.0 Findings, Observations, and NESC Recommendations

8.1 Findings

The following findings were identified and are based on the analyses conducted during this assessment and on prior experience with system identification:

F-1. Based on modal analysis, pendulum motion can be mitigated by decreasing the parachute drag coefficient (by increasing its porosity), which improves the static stability characteristics of the parachute. However, this benefit comes at the expense of increasing the steady-state descent rate, which may not be desirable.

F-2. The overall stability of the pendulum motion is dependent on both static and dynamic stability of the parachutes. It was determined that the Orion parachutes are dynamically unstable through system identification of the flight data using the planar pendulum model.

F-3. Increasing the payload mass (the largest contributor to W_{tot}) improves the stability of the system.[3] However, this benefit comes at the expense of increasing the steady-state descent rate, which may not be desirable.

---

[3] While this observation seems consistent with reference 7, experience from the CPAS drop tests suggests the opposite may be true. Half of the nominal two-parachute CPAS development drop tests experienced pendulum motion, but there were no observations of pendulum motion for the CPSS, which used the same parachute configuration numerous times but with a payload that weighed about half as much. There may have been other contributing factors, and the number of tests is insufficient to draw a conclusion with high confidence; however, it is worth noting this discrepancy as it directly applies to the parachute system analyzed in this study.

F-4. Based on modal analysis, pendulum motion is exacerbated with increasing atmospheric density because the mass of the air entrapped inside the canopy increases as the system descends in altitude.

F-5. A parachute aerodynamic model based on planar pendulum dynamics provided nonlinear C_N and C_A models that are consistent with the current MPCV aerodynamic database. $C_{N\dot{\alpha}}$ is consistent in sign (dynamically unstable) but more unstable compared with the current MPCV aerodynamic database.

F-6. Based on observations from flight data, it appears the pendulum motion for the two-parachute/payload system can be triggered by a sudden change in wind direction when the magnitude exceeds a certain threshold. Due to the passive nature of the system and the unstable damping, once the pendulum motion occurs there is little chance of exiting the limit cycle.

F-7. Based on modal analysis, the flyout and maypole modes are dominated by proximity aerodynamics.

F-8. Based on modal analysis, the orbital period of maypole motion is seen to be inversely proportional to $(C_N)_{\text{tot}}$.[4]

F-9. Analytical check cases verified the accuracy of the JSC FAST simulation and the MATLAB-based CAPDYN simulation.

F-10. Successful equation-error modeling was achieved relatively easily and quickly. Identified models predicted data from other flights with accuracy comparable to that observed in the modeling process, which is indicative of a good model.

F-11. Aerodynamic normal force models identified using the equation-error technique did not capture the strong restoring normal force generated by parachutes at large angles of attack. This was because the flight tests were passive tests (i.e., not actively controlled over a desired range of angle of attack), and the flight data included few data points at high total angle of attack, which meant that the strong restoring force at high total angle of attack was not identifiable from the flight data. This limitation in the flight data did not hinder equation-error modeling, which does not involve integrating the equations of motion.

F-12. The limited range of total angle of attack in the flight data was an important limitation for output-error modeling. Without a model term implementing strong restoring normal force at high total angle of attack (a model term not identifiable using equation error, because of few flight data points at high total angle of attack), integration of the equations of motion in the nonlinear simulation diverged quickly. Therefore, output-error modeling required introducing a stabilizing term in the normal force aerodynamic model at high total angle of attack.

F-13. For parachute cluster dynamic modeling, the line tension dynamics and interaction with the parachute aerodynamics at the start dominated the dynamic motion computed by the nonlinear simulation. Consequently, it was necessary to use flight data from the capsule

---

[4] This conclusion appears to contradict the findings in reference 12, which suggests that the orbital period increases with C_N. However, the authors of reference 12 state that those results are applicable only to a narrow range of initial conditions, which may explain the discrepancy.

payload to estimate line tension forces and use that information in the nonlinear simulation as known information, so that the modeling problem could be focused on the parachute aerodynamics. If this was not done, the output-error optimization included complex nonlinear three-body dynamics involving the parachute aerodynamics and the line tension dynamics simultaneously.

F-14. Output-error modeling for a multi-body dynamic system requires a simulation that can be readily modified with different aerodynamic models and back-driven by various flight data (e.g., flight accelerations).

F-15. To use the identified aerodynamic models in a nonlinear simulation for a parachute cluster, there must be a model for the line tension forces, probably dependent on tension line lengths and rate of change of the tension line lengths. Identifying a line tension model from flight data would require accurate measurement of the parachute position relative to the payload attachment point.

F-16. Although there were no faults found with the output-error modeling approach per se, the application of output-error modeling to a parachute cluster gave rise to important practical problems. Because of the manner in which the parachute axis system was defined in the nonlinear simulation, there were often high-amplitude, non-physical values for the aerodynamic azimuth angular rate due to the parachute axis system flipping orientation to keep the parachute z-axis pointing into the air-relative velocity vector, which was necessary for the correct aerodynamic force polarity from the identified aerodynamic model. This caused problems because the aerodynamic azimuth angular rate was used as an explanatory variable in the aerodynamic model.

F-17. Error and time lag were introduced in the computation of time derivatives inside the nonlinear simulation because the time derivatives had to be computed from only present and past values. The total angle of attack and aerodynamic azimuth angle time derivatives were important explanatory variables in the identified aerodynamic model, which made this issue important.

F-18. Relatively long data records had to be used for the output-error modeling to capture data information for various modal responses that occurred throughout a flight. This was problematic for output-error analysis, which involves repeated time integrations for different variations in the aerodynamic model parameters to find an optimized solution, because that led to lengthy and time-consuming computations for the output-error optimization. The long data records were also necessary because of the large time constants for the parachute cluster dynamic motion, making the use of shorter data record lengths within a flight an ineffective strategy. A long time integration effectively adds the aerodynamic modeling errors cumulatively over time, which makes convergence of the output-error solution more difficult. Specifically, a drift or inaccuracy in the attitude of the parachutes will adversely affect nearly every important explanatory variable (e.g., total angle of attack, proximity distance and proximity relative velocity, and both total angle of attack rate and aerodynamic azimuth angle rates).

F-19. When a dynamic system is inherently stable, output-error modeling is usually a simple and straightforward follow-on analysis, starting from equation-error results. However, in the case of an unstable system, the output-error solution becomes more difficult. The parachute aerodynamic modeling problem in this assessment could be called a brittle output-error optimization because there were both stable and unstable terms in the C_N aerodynamic model, which caused difficulty in the output-error optimization.

8.2 Observations

The following observations were identified:

O-1. Flight data for the parachute motion were obtained from videogrammetry implemented on the capsule payload, not from sensors on the parachute. Only position could be measured in this manner, which means that the velocities and accelerations were obtained from smooth numerical differentiation. One important consequence, in terms of modeling, was that the accelerations obtained for the parachutes were actual accelerations and not specific applied forces, as would be measured by accelerometer sensors.

O-2. Aerodynamic models identified using multivariate orthogonal functions included angular rate terms (e.g., total angle of attack rate and aerodynamic azimuth angle rate). When these terms are included in a nonlinear simulation, there are difficulties associated with initializing the quantities to match flight data and with computing these values accurately and without time lag inside the nonlinear simulation.

O-3. In the nonlinear simulation, the two parachutes were connected to the capsule payload by elastic riser lines, which were modeled with a fixed spring constant and damping coefficient. This caused difficulty with initializing the nonlinear simulation to match the flight data because of line tension transients, which need to die out before the nonlinear simulation run can begin properly.

O-4. Practical expertise on parachute aerodynamics was critical to the effort because parachute aerodynamics are complex and made more complex by the interaction effects between multiple parachutes. Investigations such as these will benefit from co-locating parachute and system identification experts.

8.3 NESC Recommendations

The following NESC recommendations are directed toward the analysts of current and future vehicles that want to further develop the application of system identification methods for extracting high-fidelity parachute simulation models from flight data:

R-1. Consider the application of check cases presented in Section 6.3.4 and Volume II to help validate new parachute simulations. ***(F-9)***

R-2. Install miniature IMU instrumentation at the top center of each flight-test parachute canopy, attached as rigidly as possible to the canopy, to provide data for line tension modeling and for improved time synchronization and accuracy of the photogrammetry. ***(F-13, F-15, O-1)***

R-3. Install reliable and accurate instrumentation for direct measurement of the line tension to improve both the line tension model and the parachute aerodynamic model. This could be done with a calibrated load cell near the attachment point on the capsule payload. ***(F-13, F-15, O-3)***

R-4. Install video cameras in the capsule to individually record each parachute's canopy to provide direct evidence of the canopy shape versus time, particularly to support identification of parachute aerodynamic proximity effects. ***(F-7)***

R-5. Obtain accurate measurements or estimates of winds aloft to directly improve the parachute aerodynamic modeling. Any reduction in the time and distance differences between the flight test and winds aloft measurements will improve modeling results. ***(F-6, F-10, F-18, F-19)***

R-6. Conduct flight tests for parachute aerodynamic modeling on days and at times and locations where significant wind shears are expected because primarily wind shears excite the dynamic motion of the parachutes. ***(F-6, F-10 through F-12, F-18, F-19)***

R-7. Investigate a new formulation for the parachute cluster nonlinear simulation, with the objective of avoiding large, non-physical values of aerodynamic azimuth angular rate resulting from changes in the air-relative velocity orientation relative to each parachute. Another solution would be to identify aerodynamic models that use only past values of explanatory variables rather than their time derivatives, which would address the difficulty in computing accurate real-time derivatives inside the nonlinear simulation. ***(F-16 through F-19, O-2)***

R-8. Investigate the use of alternatives to time-domain output-error modeling for the parachute aerodynamic modeling problem (e.g., frequency-domain output-error modeling and filter-error modeling). ***(F-11 through F-13, F-15 through F-19, O-1 through O-3)***

9.0 Alternative Viewpoint(s)

There were no alternative viewpoints identified during the course of this assessment by the NESC team or the NRB quorum.

10.0 Other Deliverables

No unique hardware, software, or data packages, outside those contained in this report, were disseminated to other parties outside this assessment.

11.0 Lessons Learned

No lessons learned were identified for inclusion in the NASA Lessons Learned Information System (LLIS).

12.0 Recommendations for NASA Standards and Specifications

No recommendations for NASA standards and specifications were identified as a result of this assessment.

13.0 Definition of Terms

Finding	A relevant factual conclusion and/or issue that is within the assessment scope and that the team has rigorously based on data from their independent analyses, tests, inspections, and/or reviews of technical documentation.
Lessons Learned	Knowledge, understanding, or conclusive insight gained by experience that may benefit other current or future NASA programs and projects. The

	experience may be positive, as in a successful test or mission, or negative, as in a mishap or failure.
Observation	A noteworthy fact, issue, and/or risk, which may not be directly within the assessment scope, but could generate a separate issue or concern if not addressed. Alternatively, an observation can be a positive acknowledgement of a Center/Program/Project/Organization’s operational structure, tools, and/or support provided.
Problem	The subject of the independent technical assessment.
Recommendation	A proposed measurable stakeholder action directly supported by specific Finding(s) and/or Observation(s) that will correct or mitigate an identified issue or risk.

14.0 Acronyms and Nomenclature List

14.1 Nomenclature

a_x, a_y, a_z	body-axis translational acceleration components, ft/s^2
C_l, C_m, C_n	nondimensional rolling, pitching, and yawing moment coefficients
C_X, C_Y, C_Z	nondimensional x, y, z body-axes aerodynamic force coefficients
C_A	nondimensional axial aerodynamic force coefficient
C_N	nondimensional normal aerodynamic force coefficient
g	Earth gravitational acceleration = 32.174 ft/s^2
h	altitude above mean sea level, ft
I_x, I_y, I_z	body-axis moments of inertia, slug-ft^2
I_{xz}	x-z body-axis product of inertia, slug-ft^2
l	reference length, parachute canopy nominal diameter, ft
m	parachute mass, slug
N	number of data points
$\boldsymbol{N}[\boldsymbol{m},\boldsymbol{R}]$	Gaussian vector random process with mean $\boldsymbol{m}$ and covariance $\boldsymbol{R}$
p, q, r	body-axis roll, pitch, and yaw angular velocity components, deg/s or rad/s
$\bar{q}$	dynamic pressure, lbf/ft^2
rms	root mean square
S	parachute reference area, ft^2
T	line tension, lbf
u, v, w	body-axes air-relative velocity components, ft/s
V	airspeed, ft/s
α	angle of attack, deg or rad
α_T	total angle of attack, deg or rad
β	angle of sideslip, deg or rad
Δt	sampling interval, s
ϕ_a	aerodynamic azimuth angle, deg or rad
ϕ_{prox}	proximity angle, deg or rad
ϕ, θ, ψ	Euler roll, pitch, and yaw angles, deg or rad
θ	parameter vector

Superscripts

$\hat{\ }$	estimate or nondimensional
-1	matrix inverse
$\dot{\ }$	time derivative
T	transpose

Subscripts

a	attachment point on the capsule
b	body axes
E	Earth axes
f	flyout
o	reference value or bias term
$p1$	parachute 1
$p2$	parachute 2
$prox$	proximity effect
s	swing

14.2 Acronyms

ARC	Aerodynamic Reference Center
BET	Best Estimated Trajectory
CAPDYN	Capsule Dynamics
CDT	Cluster Development Test
CM	Center of Mass
CP2	Capsule and Two Parachutes
CPAS	Capsule Parachute Assembly System
CPSS	Capsule Pallet Separation System
DCM	Direction Cosine Matrix
deg	degree
DOF	Degrees of Freedom
FAST	Flight Analysis and Simulation Tool
FFT	Fast Fourier Transform
ft	feet
ft/s	feet per second
IMU	Inertial Measurement Unit
JSC	Johnson Space Center
LaRC	Langley Research Center
lbm	pound mass
lbf	pound force
L/D	Lift to Drag Ratio
MPCV	Multi-Purpose Crew Vehicle
m/s^2	meters per second squared
NED	North-East-Down
NESC	NASA Engineering and Safety Center
psf	pounds per square foot
PCDTV	Parachute Compartment Drop Test Vehicle
PSE	Predicted Squared Error
PTV	Parachute Test Vehicle

s	second
SIDPAC	System IDentification Programs for AirCraft
SNR	Signal-to-Noise Ratio

15.0 References

1. Ray, E. S., and Varela, J. G., "EDU-A-CDT-3-11 Parachute Test Vehicle Analysis Report," CDT-3-11: JETS-JE11-13-SAIP-DOC-0028, May 2014.
2. Ali, Y., Sommer, B., Truong, T., Anderson, B., and Madsen, C., "Orion Multi-Purpose Crew Vehicle Solving and Mitigating the Two Main Cluster Pendulum Problem," AIAA-2017-4056, 2017.
3. Ray, E. S., and Machín, R. A., "Pendulum Motion in Main Parachute Clusters," AIAA-2015-2138, 2015.
4. Etkins, B., *Dynamics of Atmospheric Flight*, Dover Publications, Mineola, NY. 2000.
5. Roithmayr, C. M., Beaty, J., Pei, J., Barton, R. L., and Matz, D. A., "Linear Analysis of a Two-Parachute System Undergoing Pendulum Motion," 25th Aerodynamic Decelerator Conference, AIAA, 2019.
6. Pei, J., "Nonlinear Analysis of a Two-Parachute System Undergoing Pendulum Motion," 25th Aerodynamic Decelerator Conference, AIAA, 2019.
7. White, F. M., and Wolf, D. F., "A Theory of Three-Dimensional Parachute Dynamic Stability," *Journal of Aircraft*, Vol. 5, No. 1, 1968, pp. 86–92.
8. Ginn, J. M., Clark, I. G., and Braun, R. D., "Parachute Dynamic Stability and the Effects of Apparent Inertia," AIAA-2014-2390, 2014.
9. Pamadi, B. N., *Performance, Stability, Dynamics, and Control of Airplanes*, 3rd Edition, AIAA, 2015, pp. 427–428.
10. Knacke, T. W., "Parachute Recovery Systems Design Manual," NWC TP-6575, 1991.
11. Greathouse, J. S., and Schwing, A. M., "Study of Geometric Porosity on Static Stability and Drag using Computational Fluid Dynamics for Rigid Parahcute Shapes," 23rd Aerodynamic Decelerator Systems Conference, AIAA AVIATION Forum, AIAA 2015-2131, June 2015.
12. Wolf, D., and Heindel, K., "A Steady Rotation Motion for a Cluster of Parachutes" AIAA-2005-1629, 2005.
13. Pei, J., Roithmayr, C. M., Barton, R. L., and Matz, D. A., "Modal Analysis of a Two-Parachute System," 25th Aerodynamic Decelerator Conference, AIAA, 2019.
14. Roithmayr, C. M., and Hodges, D. H., *Dynamics: Theory and Application of Kane's Method*, Cambridge University Press, New York, 2016.
15. Morelli, E. A. and Klein, V., *Aircraft System Identification – Theory and Practice*, 2nd Edition, Sunflyte Enterprises, Williamsburg, VA, 2016, Chapters 3, 5, 6, 11, 12.
16. Morelli, E. A. and Klein, V., "Accuracy of Aerodynamic Model Parameters Estimated from Flight Test Data," *Journal of Guidance, Control, and Dynamics*, Vol. 20, No. 1, January-February 1997, pp. 74-80.

17. Morelli, E. A., “Nonlinear Aerodynamic Modeling using Multivariate Orthogonal Functions,” AIAA Paper 93-3636, *AIAA Atmospheric Flight Mechanics Conference*, Monterey, CA, August 1993.
18. Morelli, E. A., “Global Nonlinear Aerodynamic Modeling using Multivariate Orthogonal Functions,” *Journal of Aircraft*, Vol. 32, No. 2, March-April 1995, pp. 270-77.
19. Morelli, E. A., “Efficient Global Aerodynamic Modeling from Flight Data,” AIAA-2012-1050, *50th AIAA Aerospace Sciences Meeting*, Nashville, TN, January 2012.
20. Barron, A. R., “Predicted Squared Error: A Criterion for Automatic Model Selection,” *Self-Organizing Methods in Modeling*, Farlow, S. J., Ed., Marcel Dekker, Inc., New York, NY, 1984, pp. 87-104.
21. “NASA Software: System IDentification Programs for AirCraft (SIDPAC),” URL: https://software.nasa.gov/software/LAR-16100-1, last accessed August 26, 2019.
22. MPCV Aerosciences Team, “Orion Aerodynamic Databook Ver 0.94-1,” NASA MPCV-72167, 2018.
23. Anderson, B. P., *et al*., “Sub-scale Orion Parachute Test Results From the National Full-Scale Aerodynamics Complex 80- by 120-ft Wind Tunnel,” 24th AIAA Aerodynamic Decelerator Systems Technology Conference, AIAA AVIATION Forum, AIAA 2017-4203, June 2017.
24. Owens, D. B., *et al*., “Orion Crew Module and Parachute System Aerodynamic Modeling,” ITAR Paper, AIAA AVIATION Forum, AIAA 2016-3988, June 2016.
25. Robinson, P. E. and Powell, J. M., “Two Main Chute Proximity Update,” CAP-CR-Aero-077 Rev 2, July 2017.

Appendices (separate Volume II)

Appendix A.	Verification Case 1 – Constant Density Descent
Appendix B.	Verification Case 2 – Exponential Density Descent
Appendix C.	Verification Case 3 – Vertical Wind Shear, Constant Density
Appendix D.	Verification Case 4 – Steady-state Glide
Appendix E.	Verification Case 5 – Horizontal Wind Shear, Constant Density
Appendix F.	Verification Case 6 – Pendulum Motion
Appendix G.	Verification Case 7 – Flyout Motion
Appendix H.	Verification Case 8 – Maypole
Appendix I.	Verification Case 9 – Nonplanar Pendulum Motion
Appendix J.	Verification Case 10 – Nonplanar Flyout Motion
Appendix K.	Prescribed Aerodynamics Required for Nonplanar Pendulum Motion in CAPDYN

REPORT DOCUMENTATION PAGE

Form Approved
OMB No. 0704-0188

1. REPORT DATE *(DD-MM-YYYY)*
10/03/2019

2. REPORT TYPE
Technical Memorandum

3. DATES COVERED *(From - To)*

4. TITLE AND SUBTITLE
Application of System Identification to Parachute Modeling

5a. CONTRACT NUMBER

5b. GRANT NUMBER

5c. PROGRAM ELEMENT NUMBER

6. AUTHOR(S)
Murri, Daniel G.; Morelli, Eugene A.; Pei, Jing; Roithmayer, Carlos M.;
Matz, Daniel A.; Barton, Richard L.; Mendenhall, Michael R.

5d. PROJECT NUMBER

5e. TASK NUMBER

5f. WORK UNIT NUMBER
869021.05.07.12.01

7. PERFORMING ORGANIZATION NAME(S) AND ADDRESS(ES)
NASA Langley Research Center
Hampton, VA 23681-2199

8. PERFORMING ORGANIZATION REPORT NUMBER
L-21061 NESC-RP-15-01037

9. SPONSORING/MONITORING AGENCY NAME(S) AND ADDRESS(ES)
National Aeronautics and Space Administration
Washington, DC 20546-0001

10. SPONSOR/MONITOR'S ACRONYM(S)
NASA

11. SPONSOR/MONITOR'S REPORT NUMBER(S)
NASA/TM-2019-220410/Volume I

12. DISTRIBUTION/AVAILABILITY STATEMENT
Unclassified - Unlimited
Subject Category 16 Space Transportation and Safety
Availability: NASA STI Program (757) 864-9658

13. SUPPLEMENTARY NOTES

14. ABSTRACT

The NASA Engineering and Safety Center (NESC) was requested to determine the feasibility of using modern system identification techniques for developing high-fidelity parachute models from parachute drop-test flight data, using full-scale Orion Capsule Parachute Assembly System (CPAS) drop-test pendulum-mode flight data as a test case. This document contains the outcome of the NESC assessment.

15. SUBJECT TERMS
NASA Engineering and Safety Center; Parachute Modeling; Capsule Dynamics; Capsule Parachute Assembly System

16. SECURITY CLASSIFICATION OF:

a. REPORT	b. ABSTRACT	c. THIS PAGE	17. LIMITATION OF ABSTRACT	18. NUMBER OF PAGES
U	U	U	UU	106

19a. NAME OF RESPONSIBLE PERSON
STI Help Desk (email: help@sti.nasa.gov)

19b. TELEPHONE NUMBER *(Include area code)*
(443) 757-5802

Standard Form 298 (Rev. 8/98)
Prescribed by ANSI Std. Z39.18